1-1-2015

Engineering Novel Nanostructures via Chemical and Morphological Transformations

Rahul Agarwal
University of Pennsylvania, rahulagg88@gmail.com

Engineering Novel Nanostructures via Chemical and Morphological Transformations

Abstract
Materials at the nanoscale have revolutionized the world around us by enabling the discovery of novel size dependent properties and experimental verification of untested theoretical concepts. However, most nanomaterials today are phases of matter that are well known and have been studied extensively at the bulk scale. For example, II-VI semiconductors, which are widely studied today at the nanoscale, were employed in photovoltaic applications at the microscale for nearly half a century. The question that arises is whether material processing at the nanoscale can allow us to go beyond the limitations of conventional synthesis techniques? We believe that the next pathbreaking step in nanotechnology is to synthesize novel phases of materials which are metastable by thermodynamic considerations and hence challenging to achieve through established one-step synthesis processes. At the core of such an approach is the desire to gain in-depth scientific understanding of the chemical and morphological transformation mechanisms that enable the engineering of novel nanomaterials with exotic physical properties.

Our research revolved around synthesizing novel nanomaterials from preexisting nanostructures via chemical and morphological transformation in a chemical vapor deposition system while preserving the morphology and atomic arrangement of the parent material through, what we like to call, "atomic templating". We explored chemical transformation in II-VI semiconducting nanostructures via anion exchange to synthesize metastable phases of materials such as zincblende CdS and CdSe while retaining the crystal structure and twin boundaries of the parent zincblende CdTe. We later extended the concept of atomic templating to explore chemical substitution in II-VI semiconductors with elements from dissimilar groups of the periodic table such as IV A and V A that possess different bonding characteristics with chalcogenides as compared to elements of group II B. We also studied chemical substitution in a covalently bonded compound, GeTe. Finally, morphological transformation of CdS nanobelts into periodically branched nanostructures was studied through environmental TEM. The resulting nanostructures were thoroughly characterized via electron microscopy, photoluminescence and Raman spectroscopy. Through first principles calculations via density functional theory, experimental observations were explained and novel physical properties targeted at specific applications were predicted.

Degree Type
Dissertation

Degree Name
Doctor of Philosophy (PhD)

Graduate Group
Materials Science & Engineering

First Advisor
Ritesh Agarwal

Keywords
Atomic Templating, Chemical transformation, In-situ TEM, Ion exchange, Morphological transformation, Nanotechnology

Subject Categories
Mechanics of Materials | Nanoscience and Nanotechnology

ENGINEERING NOVEL NANOSTRUCTURES VIA CHEMICAL AND MORPHOLOGICAL TRANSFORMATIONS

Rahul Agarwal

A DISSERTATION

in

Materials Science and Engineering

Presented to the Faculties of the University of Pennsylvania

in

Partial Fulfillment of the Requirements for the

Degree of Doctor of Philosophy

2015

Supervisor of Dissertation

Signature _____

Ritesh Agarwal, Professor, Materials Science & Engineering

Graduate Group Chairperson

Signature _____

Shu Yang, Professor, Materials Science & Engineering

Dissertation Committee

David P. Pope, Professor, Materials Science & Engineering

Christopher B. Murray, Richard Perry University Professor, Chemistry and Materials Science & Engineering

Daniel S. Gianola, Professor, Materials Science & Engineering

ENGINEERING NOVEL NANOSTRUCTURES VIA CHEMICAL AND

MORPHOLOGICAL TRANSFORMATIONS

To the three pillars of my life: my parents and my wife.

ACKNOWLEDGMENTS

An individual's PhD degree is always so much more than an individual effort and I'm sincerely grateful to my professors, collaborators, colleagues, friends and family for their continued guidance, support and love throughout this journey.

Professor Ritesh Agarwal, my thesis supervisor, mentor and friend. You have been the most influential person in my academic life since the first time I was a naïve undergraduate summer researcher in your lab and I have learnt so much from you about research and life in general over these past seven years. Thank you for showing so much confidence in me throughout this journey and providing the independence and guidance to pursue my research goals. The freedom of research that I enjoyed in our group, which allowed me to collaborate with colleagues both inside and outside our lab, has been instrumental in my understanding of materials science. Though the bar is set extremely high, I aspire to have the same unbiased and uninhibited perspective towards science and research as you do.

I am very grateful to my dissertation committee members, Professor David P. Pope, Professor Christopher B. Murray and Professor Daniel S. Gianola from the Department of Materials Science and Engineering who have been my teachers (MSE 505, Mechanical Properties and MSE 545, Energy Storage and Technology), mentors and collaborators. Thank you for always being so approachable and open to scientific discussions and invaluable feedback which has greatly influenced my thinking process and research. I have also learnt a lot from you during our informal discussions and I will always cherish those conversations.

I feel honored to have collaborated with some amazing scientists who helped enrich my work and understanding of materials science. Dr. Eric A. Stach and Dr. Dmitri N. Zakharov from Brookhaven National Lab for experiments on the environmental transmission electron microscope, Dr. Youngkuk Kim, Dr. Liang Z. Tan and Shi Liu from Professor Andrew M. Rappe's group for first principles density functional theory calculations. I'm very grateful to past and present members of Agarwal research group who have been instrumental in this journey, especially Dr. Yeonwoong Jung, Dr. Hee-Suk Chung, Dr. Christopher M. Rodd, Dr. Brian Piccione, Dr. Carlos O. Aspetti, Dr. Mingliang Ren, Dr. Moon H. Jung, Dr. Sajal Dhara and Jacob Berger. A special thank you to my friend and colleague, Dr. Pavan Nukala, who has deeply influenced my research through numerous collaborations and endless scientific discussions over the past five years. Undergraduate researchers, Karthik Kumar, Nadia M. Krook and Sonya Kripke, thanks for bringing fresh energy and ideas to my research. Thank you to my other collaborators, Professor Matteo Cargnello at Stanford Chemical Engineering, Frank Streller from Professor Robert Carpick's group at Penn and Dr. Vicky Doan-Nguyen from Professor Christopher B. Murray's group at Penn for helping me widen my horizons.

I appreciate the hard work, training and support of brilliant staff members Dr. Douglas M. Yates, Dr. Jamie T. Ford, Dr. Matthew Brukman and Steve Szewczyk at Penn research facilities that enable smooth and efficient experiments round the clock. I am also grateful to Ms. Patricia Overend, Ms. Vicky Lee and Ms. Irene Clements for their tremendous support and for providing a home like atmosphere thousands of miles away from home.

I am grateful to Dr. Mahadevan Khantha and Professor Ertugrul Cubukcu who showed a lot of confidence by employing me as their teaching assistant for seven semesters at Penn (MSE 540, Phase Transformation and MSE 570, Physics of Materials).

I am fortunate to have come across so many interesting and kindhearted people at Penn who are my friends today. My MSE PhD year has been a solid rock of support throughout this journey and special thanks to Ashley Gaulding, Dr. Elaine Lee, Dr. Joohee Park, Jason Reed, Dr. Sharon Sharick and Dr. Ryan Wade. I'm grateful to Dr. Carlos Aspetti, Dr. Lisa Chen, Dr. Robert Ferrier, Dr. David Kim, Dr. Kathryn Murphy, Dr. Vicky Doan-Nguyen, Dr. Pavan Nukala and Dr. Michael O'Reilly for always sharing their insightful wisdom and friendly advice. I'm also thankful to Jenica Abram, Daksh Agarwal, Jacob Berger, Nicholas Greybush, Tyr Holmström, Nadia Krook, Daniel Magagnosc, Anne E. Mehaffey, L. Robert Middleton, Yash Pant, Jason Pope, Luke Shi, Frank Streller, Spencer Thomas, Edward Trigg and Han Chang Yang for sharing some amazing moments of our lives together. A special mention to those who made it all the way to India for my wedding. Please know that my wife and I will forever be grateful.

Most importantly, my mother Smt. Neelam Agarwal and my father Shri Prashant Kumar who sacrificed at every juncture of their life to ensure that I had the best there was to offer. They always supported my ambitions and I would have never had the courage to pursue my dreams if it was not for their love and motivation. My wife, Dr. Sanghmitra P. Arvindekar, who will always be the one true love and guiding light of my life and has been my partner through nine years of a challenging long distance relationship. My uncle, Late Prof. Sanjeev K. Aggarwal (IIT-Kanpur) who was a strong inspiration and helped ignite the fire of scientific curiosity at an early stage of my life. Thank you!

ABSTRACT

ENGINEERING NOVEL NANOSTRUCTURES VIA CHEMICAL AND MORPHOLOGICAL TRANSFORMATIONS

Rahul Agarwal

Ritesh Agarwal

Materials at the nanoscale have revolutionized the world around us by enabling the discovery of novel size dependent properties and experimental verification of untested theoretical concepts. However, most nanomaterials today are phases of matter that are well known and have been studied extensively at the bulk scale. For example, II-VI semiconductors, which are widely studied today at the nanoscale, were employed in photovoltaic applications at the microscale for nearly half a century. The question that arises is whether material processing at the nanoscale can allow us to go beyond the limitations of conventional synthesis techniques? We believe that the next pathbreaking step in nanotechnology is to synthesize novel phases of materials which are metastable by thermodynamic considerations and hence challenging to achieve through established one-step synthesis processes. At the core of such an approach is the desire to gain in-depth scientific understanding of the chemical and morphological transformation mechanisms that enable the engineering of novel nanomaterials with exotic physical properties.

Our research revolved around synthesizing novel nanomaterials from preexisting nanostructures via chemical and morphological transformation in a chemical vapor deposition system while preserving the morphology and atomic arrangement of the parent material through, what we like to call, “atomic templating”. We explored chemical

transformation in II-VI semiconducting nanostructures via anion exchange to synthesize metastable phases of materials such as zincblende CdS and CdSe while retaining the crystal structure and twin boundaries of the parent zincblende CdTe. We later extended the concept of atomic templating to explore chemical substitution in II-VI semiconductors with elements from dissimilar groups of the periodic table such as IV A and V A that possess different bonding characteristics with chalcogenides as compared to elements of group II B. We also studied chemical substitution in a covalently bonded compound, GeTe. Finally, morphological transformation of CdS nanobelts into periodically branched nanostructures was studied through environmental TEM. The resulting nanostructures were thoroughly characterized via electron microscopy, photoluminescence and Raman spectroscopy. Through first principles calculations via density functional theory, experimental observations were explained and novel physical properties targeted at specific applications were predicted.

TABLE OF CONTENTS

LIST OF TABLES

LIST OF ILLUSTRATIONS

CHAPTER 1: Introduction

Adapted and reprinted in parts from:

B.Piccione, R. Agarwal, Y. Jung and R. Agarwal, "Size-dependent chemical transformation, structural phase change, and optical properties of nanowires", Philosophical Magazine 93, (2013), p.2089. Reproduced with permission.

B. Zhang, Y. Jung, H.-S. Chung, L. K. Van Vugt and R. Agarwal, "Nanowire Transformation by Size-Dependent Cation Exchange Reactions", Nano Letters, 10, (2010), p.149. Reproduced with permission.

1.1 One Dimensional Nanostructures

Nanowires and nanobelts, quasi-one-dimensional structures that exhibit high anisotropy between their nanometer-scale diameters and micrometer-scale lengths, have received significant attention in the last decade for their unique physical and chemical properties as well as for their promise for applications in a variety of devices and systems[1]. Synthesized as early as the 1960s by Wagner and Ellis[2], these novel nanostructures have since been actively researched for their potential use as active device components such as field effect transistors[3], logic devices[4], microprocessors and complete programmable circuits[5], sensors[6–10], nanogenerators[11,12], light-emitting diodes[13,14], electrically driven lasers[15], solar cells[16], and lithium-ion battery anodes[17] among many notable examples. Benefits gained from high surface-to-volume ratios, as well as electrical or optical confinement in the radial direction, are accessible due to the long lengths of the nanowires, which allow electrical connections and interconnection to

be made via conventional lithographic techniques. In the cases where benefits gained from radial confinement are unaffected by nanowire length, nascent techniques have potential for scaling single-nanowire devices to multi-nanowire systems: microfluidic assembly[18,19], electric field[20,21], dielectrophoresis[22–24], mechanical transfer[25–27], and optical tweezers[28–31], for instance, have potential for aiding in precise placement within smaller-scale systems, while techniques such as Langmuir–Blodgett[32–34], branched nanowire growth[35–37], or 3-D assembly[38,39] could eventually mature sufficiently for large-scale deterministic system assembly.

1.2 Ion-Exchange Reaction at the Nanoscale

The unique properties of nanostructured materials enable their transformation into complex and occasionally kinetically controlled morphologies, which cannot be obtained during their growth. Solution-phase cation-exchange reactions can transform sub-10 nm nanocrystals and nanorods into varying compositions and superlattice structures; however, due to their small size, ion-exchange reaction rates are extremely fast, which limits control over the transformed products and possibilities for obtaining new morphologies. On the other hand, ion-exchange phenomena in bulk materials are quite slow, occur at very high temperatures, and also damage the material due to the large stress that builds up during the course of the reaction. Recent efforts in transforming nanowires with length scales that bridge the gap between nanocrystals and bulk materials into kinetically controlled products using ion-exchange reactions in the gas phase are discussed. These studies also shed new insights into how diffusion, domain growth, and percolation occur at the nanoscale, leading to novel transformations.

Ion exchange is a useful technique for chemically transforming one material to another, partially or completely, in order to modify its structural, chemical and physical properties. In bulk materials, ion exchange is mainly circumscribed to the surface due to the high activation energy required for diffusion of atoms, thus making the transformation extremely sluggish[40]. However, nanostructures, owing to their high surface-to-volume ratios, effectively reduce the kinetic barrier for diffusion[40]. This enables their fast and complete chemical transformation while undergoing ion exchange. Researchers have displayed controllability of ion exchange both in terms of the extent of composition and volume transformation. Moreover, nanostructures have shown not just compositional but morphological transformation as well, which makes ion exchange at the nanoscale an exciting method of making novel multi-component materials with highly complex structures, morphologies, and composition modulation. In this section, we will look at some of the notable work in the field of ion exchange in nanostructures that promise to deliver the next generation of engineered nanomaterials and focus on our group's work in the area of controlled gas-phase transformation of semiconductor nanowires. For ionic compounds, it is well known that anions form the rigid framework of the crystal lattice, whereas the cations are relatively mobile[42]. Therefore, it is kinetically more challenging to perform anion exchange, which often involves complete transformation of the crystal framework as opposed to cation exchange, which is a much simpler diffusion process. In fact, anion exchange often leads to more drastic morphological changes than its cationic counterpart. Hence, the latter has been studied more widely due to the ease with which it can be accomplished.

1.3 Cation-Exchange Reaction

Some of the early work in the field of cation exchange in nanostructures was reported by Alivisatos and coworkers on the rapid ($t << 1$ s) and reversible transformation of CdS nanocrystals into Ag_2Se in solution phase under ambient conditions in a very short period[40]. The extremely fast transformation was attributed to the lowering of the kinetic barrier for diffusion in nanostructures. They also studied the size-dependent morphological transformation in anisotropic non-equilibrium nanostructures such as rods. It was found that if the initial diameter of the nanostructure is smaller than the reaction zone width, then the entire structure becomes unstable during transformation and can equilibrate in the form of a lower surface energy morphology such as a sphere, but if not, the initial morphology remains stable and the reaction zone continues progressing from the surface toward the core. The same group demonstrated superlattice formation in nanorods as a result of partial cation exchange[43]. The starting material was chosen as CdS nanorods, which on reaction with a limited source of Ag^+ ions resulted in the formation of alternating segments of CdS and Ag_2S. Formation of such a superlattice was explained by limited cation exchange in the CdS nanorods that led to small islands of Ag_2S on the surface. These islands found it energetically favorable to merge into segments through Ostwald ripening since it would reduce the surface area between CdS and Ag_2S domains. This process continued until the point that these segments spanned the entire diameter of the rod and joining of these segments would be kinetically unfavorable. Regular spacing of the stripe pattern was explained by elastic repulsion between Ag_2S segments due to the strain in CdS region in between. This elastic

strain was generated so that Ag_2S lattice can match the basal lattice constant of CdS. This phenomenon has been further studied with some theoretical explanation for the formation of these superlattices and their elastic properties are predicted based on experimental and structural data[44]. Diffusion-limited growth and ordering due to epitaxial strain is believed to drive the spontaneous pattern formation. Another important work by the same group showed how the anionic framework is conserved in ionic nanocrystals when they undergo cation exchange[45]. This was proven by performing cation exchange on CdS nanorods embedded with a CdSe nanocrystal (CdSe/CdS) to obtain a PbSe/PbS product via a Cu_2Se/Cu_2S structure. During this two-step exchange process, the size and the position of the selenide nanocrystal within the nanorod was preserved. Alivisatos and co-workers also looked at synthesis of nanocrystal heterostructures as a result of selective cation exchange on different facets of the parent nanocrystal[46]. Experimental and theoretical models of cation exchange by Cu on different crystallographic facets of CdS nanorods were studied. They observed and justified, based on interfacial energy arguments, how Cu_2S segments were formed on the ends of the CdS nanorods.

Jeong and coworkers transformed Ag_2Te nanowires into CdTe (also ZnTe and PbTe) nanowires and then into $PtTe_2$ nanotubes through cation exchange in solution phase[47]. In this work, they showed how solubility products (K_{sp}) of ionic solids can be used to predict whether transformation is thermodynamically favorable or not. Ideally, an ionic solid with a relatively high K_{sp} value will undergo cation exchange to form another ionic solid with relatively low K_{sp}. The solubility product itself can be adjusted as a function of temperature, presence of common ions, and also the size of the ionic solid.

The change in morphology was explained by the volume transformation that takes place during cation exchange: if the volume change in the material is large, then it can lead to stress accumulation, which relieves itself leading to morphological changes. For example, severe axial stress in a nanowire can cause it to fracture into smaller nanorods, and radial stress can cause migration of material from or toward the surface. Formation of $PtTe_2$ nanotubes was also explained by a large volume change on cation exchange in CdTe nanowires, which causes stress accumulation that forces Te to be driven out from the core, leading to a hollow one-dimensional nanostructure. Jeong and coworkers also synthesized uniform CdSe nanowires from Ag_2Se nanowires in the solution phase such[48,49] that both the morphology and the single crystallinity of the parent phase were preserved[48,49]. Ma and colleagues synthesized trigonal Se nanowires from amorphous Se nanoparticles and transformed them into Ag_2Se and CdSe nanowires through cation exchange[50].

1.4 Anion-Exchange Reaction

Even though energetically and structurally challenging, several successful attempts have been reported to obtain anion exchange in nanostructures. Könenkamp and coworkers converted columnar ZnO films into ZnS-coated ZnO nanocolumns (aspect ratio ~ 10) in the vapor phase by reaction with H_2S at 400 °C[51]. The core of the column was etched away by H_2SO_4, leaving behind ZnS nanotubes. Könenkamp and coworkers further extended their work by substituting zinc with copper in the solution phase to yield Cu_2S nanotubular structures[52]. Similar work was done to create PbS/PbSe[53] and CdS/CdSe[54] core–shell nanostructures in the solution phase. Metal hydroxides have been

used by numerous researchers to obtain metal chalcogenides by employing an anion exchange reaction. Shim and coworkers[55] used $Cd(OH)_2$ nanowire bundles as a starting template to synthesize CdSe nanotubes in the solution phase, and the resulting tubular morphology was a result of the Kirkendall effect due to faster outward diffusion of Cd in comparison with inward diffusion of Se[56]. Another novel work is the spatial confinement of anion exchange reaction in a single-walled carbon nanotube (SWCNT)[57]; metal halide/SWCNT core–shell system was synthesized via impregnation of SWCNTs with low-melting cadmium iodide. Subsequently, anion exchange was carried out by sulfidation in molten sulfur to obtain CdS/SWCNT core–shell structure. This experiment was extended to other systems to yield similar MX/SWCNT core–shell morphologies (M = Cd, Zn, Pb; X= S, Se, Te).

1.5 Vapor Phase Ion-Exchange Reaction

Most of the ion-exchange work has focused on transformations in the solution phase of nanocrystals in the sub-10 nm size scale, where the transformations occur very rapidly. It would be interesting to extend ion-exchange work for larger systems (10–100 nm) and in the gas phase to make it more compatible with a wide range of nanomaterials grown using gas-phase techniques. Park and coworkers have attempted cation exchange on nanowires by chemical vapor transport; in their earlier work, they converted CdS nanobelts into ZnS nanobelts by Zn vapor (evaporated Zn metal) transport at 800 °C[58]. They also showed that the reverse reaction cannot be achieved completely even at higher temperatures pointing out the thermodynamic stability of one phase over the other. In another similar work, they transformed ZnTe nanowires into CdTe nanowires through an

intermediate ZnCdTe-CdTe core–shell nanowire structure[59]. The extent of transformation was controlled by the reaction time, which dictated how deeply the CdTe growth front would penetrate inside the wire.

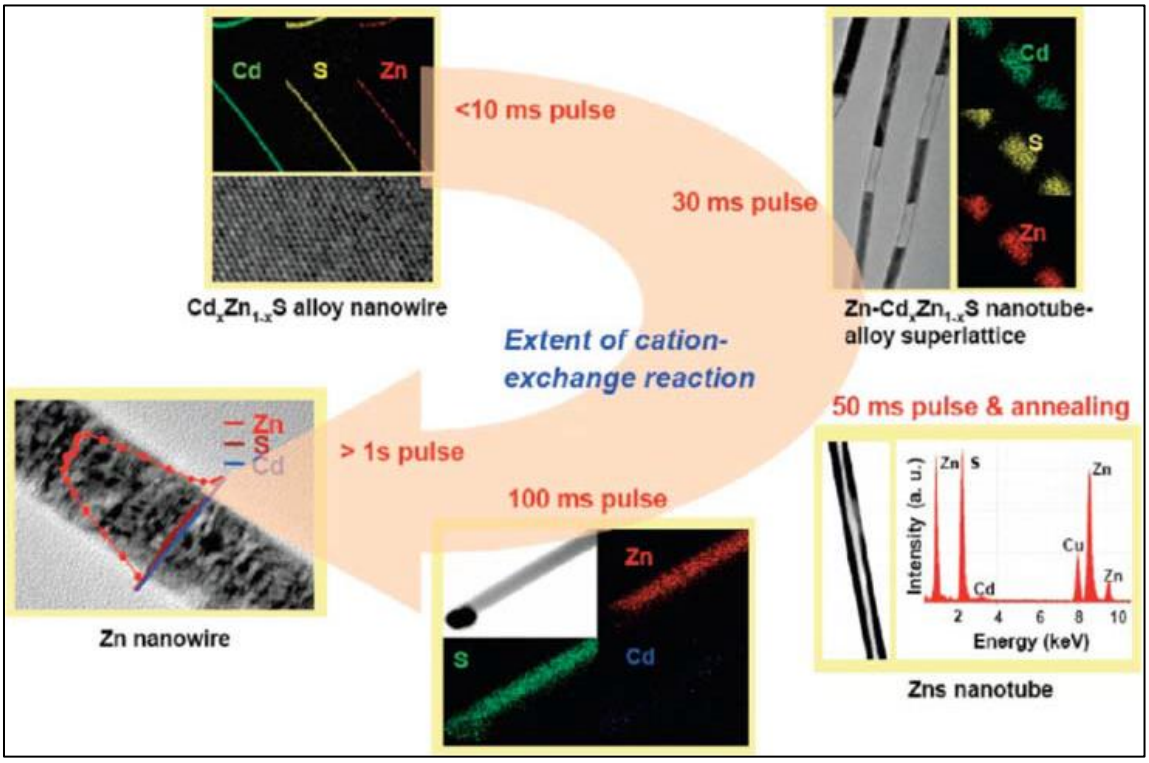

Figure 1.1 Schematic showing the overview of nanowire transformations precisely controlled by cation-exchange reactions. Initial CdS nanowires are transformed into various morphologies as the extent of cation exchange reactions are controlled by the amount (ms pulse) of DMZn delivery in the gas phase. Reprinted with permission from reference 60.

The first successful attempt at a precisely controlled composition and morphology in nanostructures via cation exchange in the gas phase was reported by Zhang and coworkers in our group[60]. Starting from CdS nanowires, they were able to obtain compositionally tunable $Cd_xZn_{(1-x)}S$ nanowires, Zn_{tube}–$Cd_xZn_{(1-x)}S$ superlattices, ZnS nanotubes, ZnS nanowires, and pure Zn nanowires as a function of increasing Zn precursor dimethyl Zn, (DMZn) inside an atomic layer deposition furnace (Figure 1.1).

They also observed size-dependent variation in transformation in nanowires performed under different reaction temperatures. It was observed that at elevated temperatures (220 °C), thin nanowires (<25 nm) completely transformed into ZnS nanowires, slightly thicker ones (30–90 nm) formed $Cd_xZn_{(1-x)}S$ nanowires ('x' decreases as a function of decreasing nanowire diameter) and the thickest ones only displayed cation exchange 25–30 nm from the surface, whereas the core remained intact. Nanowires that were less than 10 nm in size could undergo complete transformation even at temperatures as low as 50 °C. They measured the decrease in the activation energies of the exchange reactions with decreasing nanowire diameters, which is a sum of diffusion and exchange reaction energies. This provided a concrete proof of how cation exchange is a much faster phenomenon in nanostructures as compared to bulk mainly due to the dramatic decrease in diffusion activation energies.

To study the morphological transformations obtained upon increasing amount of Zn precursor, nanowires of a tight distribution range (~50 nm) were chosen and reactions were carried out at 350 °C. The results and proposed mechanisms were as follows. As shown in Figure 1.2, on introducing a small amount of DMZn, $Cd_xZn_{(1-x)}S$ nanowires were formed as a result of partial cation exchange with the morphology intact due to very little strain in the system. On increasing the DMZn, Zn_{tube}–$Cd_xZn_{(1-x)}S$ superlattices were formed as a result of segregation between Zn-rich and $Cd_xZn_{(1-x)}S$ segments. On further increasing DMZn concentration and subsequent annealing, ZnS nanotubes were formed. This result was explained by a complete radial stress from ZnS shell formation, which pushes unbound Cd and S toward the core–shell interface where they are trapped. Upon

annealing, these materials eventually escaped, leaving behind a ZnS nanotube. Upon a further increase in DMZn concentration, complete cation exchange occurred and ZnS

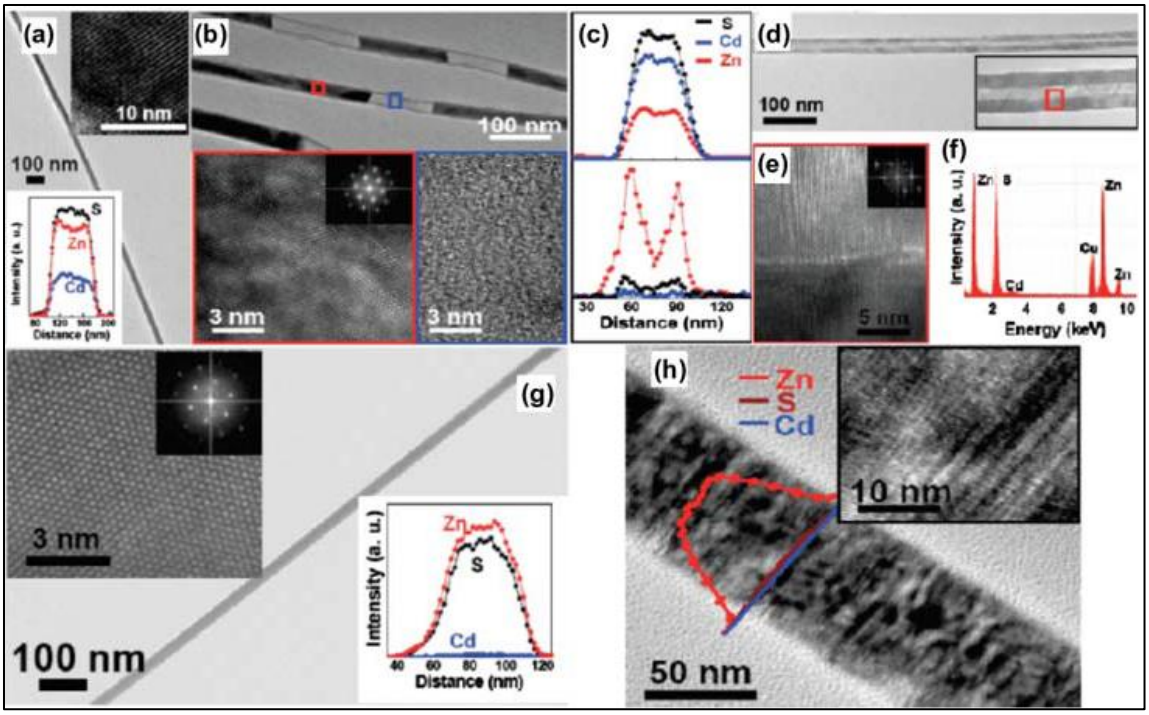

Figure 1.2 (a) High-resolution TEM (HRTEM) of an intermediate sized CdS nanowire (70 nm) transformed to a single-crystalline $Zn_xCd_{(1-x)}S$ with x0.7 structure (top inset) and the corresponding EDS line scans along the radial direction (bottom inset). (b) TEM image of nanowire super-lattices showing alternating segments of solid and tubular regions. HRTEM images obtained from the solid region (red) shows single-crystalline structure (inset: corresponding fast Fourier transform (FFT)) while the nanotube region (blue) is a mixture of polycrystalline and amorphous regions. (c) EDS line spectrum shows that the solid region (top, and red box in panel (b) are alloyed $Zn_xCd_{(1-x)}S$ with x~0.35 and the tubular regions (bottom, and blue box in panel (b) are highly Zn-rich with negligible Cd and S. (d) TEM image of a ZnS nanotube formed by annealing the core/shell-like nanowires. Inset shows a zoomed-in image of the body of the nanotube. (e) HRTEM image and the corresponding FFT of the region enclosed by the red box in panel (d). (f) Point-scan EDS spectrum obtained from the body of the nanotube clearly showing that it is ZnS. (g) TEM image of a ZnS nanowire completely transformed from a 50 nm CdS nanowire obtained with a 100 ms DMZn pulse. Top inset: HRTEM image and the corresponding FFT showing the single-crystalline structure of the transformed nanowire. Bottom inset: EDS line-scan spectrum from the same nanowire showing that it is stoichiometric ZnS with no Cd. (h) TEM of Zn nanowires obtained with a1s DMZn pulse with the corresponding EDS line scans superimposed showing almost no Cd or S. Inset: HRTEM of the Zn nanowire showing the roughened surface with polycrystalline and amorphous grains. Reprinted with permission from reference 60.

nanowires were formed. Higher concentrations caused severe diffusion and system instability, resulting in the formation of pure polycrystalline zinc nanowires by rapid outward diffusion of cadmium and sulfur.

Accomplishments in the field of nanostructure ion exchange have provided us with novel materials exhibiting very promising electrical, thermal, and optical properties. The study of the underlying science of ion exchange promises to open new frontiers in the field of nanomaterial synthesis. Cation exchange is now a well-studied field, and even though anion exchange has not been probed into as much as it deserves, it will be interesting to see how the chemical and structural evolution occurs at the nanoscale when the structural pillars (anions) in an ionic solid are replaced. The underlying science is still being probed carefully and promises to open new frontiers in the field of nanomaterial synthesis.

1.6 Crystal Structure and Lattice Parameter of Relevant Materials

1.6.1 Wurtzite Crystal Structure

Several compounds, including those of II-VI and III-V semiconductors, crystallize in wurtzite crystal structure where each atom of one type is in tetrahedral coordination with atoms of the other type (Figure 1.3). A wurtzite crystal can be obtained by stacking close packed two dimensional alternating layers of atoms in the sequence A a B b A a B b… where ‘A’ and ‘B’ denote different stacking sequence of one type of an atom and ‘a’ and ‘b’ denote different stacking sequence of the other type of an atom. Wurtzite has a hexagonal unit cell with the long axis perpendicular to the close packed

plane referred to as the *c*-axis and the other two axis in plane of the close packed plane as *a* and *b* respectively. The most common planar defects in wurtzite materials are stacking faults, a local anomaly in the stacking sequence of close packed planes which leads to formation of a small region of zincblende crystal structure. Some common examples are CdS, CdSe, ZnO and GaAs.

Table 1.1 Lattice constants of relevant II-VI semiconductors in wurtzite phase.

Compound	**Lattice constant *a* (Å)**	**Lattice constant *c* (Å)**
CdS	4.135	6.75
CdSe	4.3	7.02
CdTe	4.55	7.45

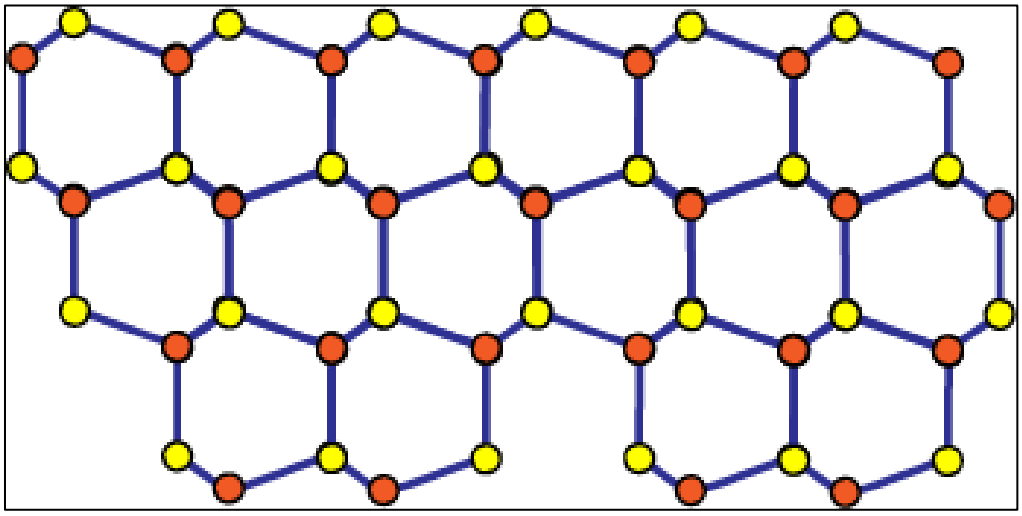

Figure 1.3 Wurtzite crystal structure (Space group: $P6_3mc$) of a binary compound viewed along a-axis. Each atom is in tetrahedral coordination with atoms of the other species. The stacking sequence of any one atomic species is of the type A B A B A B.

1.6.2 Zincblende Crystal Structure

Several compounds, including those of II-VI and III-V semiconductors, also crystallize in zincblende phase where each atom of one type is in tetrahedral coordination with atoms of the other type (Figure 1.4). A zincblende crystal can be obtained by stacking close packed two dimensional alternating layers of atoms in the sequence A a B b C c… where 'A', 'B' and 'C' denote different stacking sequence of one type of an atom and 'a', 'b' and 'c' denote different stacking sequence of the other type of an atom. Zincblende has a cubic unit cell. The most common planar defects in zincblende materials are stacking faults, a local anomaly in the stacking sequence of close packed planes leading to formation of wurtzite crystal structure and twin boundaries which act as a mirror plane. Some common examples are CdTe, ZnS, ZnTe and GaSb.

Table 1.2 Lattice constants of relevant II-VI semiconductors in zincblende phase.

Compound	Lattice constant *a* (Å)
CdS	5.81
CdSe	6.08
CdTe	6.48

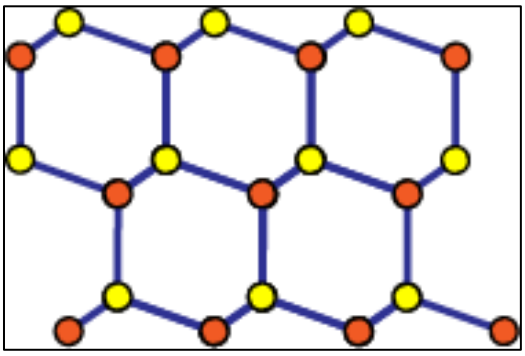

Figure 1.4 Zincblende crystal structure (Space group: $F\bar{4}3m$) of a binary compound viewed along <110>. Each atom is in tetrahedral coordination with atoms of the other species. The stacking sequence of any one atomic species is of the type A B C A B C A B C.

1.6.3 Rocksalt Crystal Structure

Several compounds, especially I-VII and IV-VI materials, crystallize in rocksalt phase where each atom of one type is in octahedral coordination with atoms of the other type (Figure 1.5). A rocksalt crystal can be obtained by stacking close packed two dimensional alternating layers of atoms in the sequence A c B a C b… where 'A', 'B' and 'C' denote different stacking sequence of one type of an atom and 'a', 'b' and 'c' denote different stacking sequence of the other type of an atom. Rocksalt has a cubic unit cell. The most common planar defects in rocksalt materials are stacking faults, a local anomaly in the stacking sequence of close packed planes leading to formation of trigonal prismatic structure and twin boundaries which act as a mirror plane. Some common examples are NaCl, CdO, PbTe and PbSe.

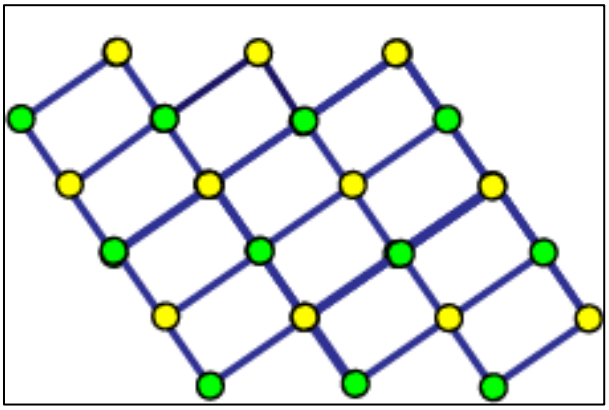

Figure 1.5 Rocksalt crystal structure (Space group: $Fm\bar{3}m$) of a binary compound viewed along <110>. Each atom is in octahedral coordination with atoms of the other species. The stacking sequence of any one atomic species is of the type A B C A B C.

Table 1.3 Lattice constants of relevant compounds in rocksalt phase.

Compound	Lattice constant *a* (Å)
PbSe	6.13
PbTe	6.48
BiTe	6.48

1.7 Thesis Outline

This document mainly consists of our efforts in the direction of engineering next-generation nanomaterials through chemical and morphological transformations. Chapter 2 explains high temperature vapor phase anion exchange reaction in II-VI semiconducting nanostructures exploring the chemical and structural transformation at the nanoscale as the structural pillars (anions) of a material are systematically and completely replaced. The products of chemical transformation are characterized by TEM based microscopy and Raman and photoluminescence spectroscopy techniques. Mechanism of the observed chemical transformation is described in detail and the idea of 'atomic templating' is discussed as a novel route of synthesizing metastable phases of well-known compounds while retaining the morphology and crystal structure of the parent compound even upon complete chemical transformation. This understanding is utilized to engineer metastable phases such as zincblende CdS and CdSe with controlled defect distribution.

Chapter 3 explores high temperature vapor phase reactivity of II-VI semiconducting nanostructures with elements of dissimilar periodic groups (IV A and V A) resulting in cation exchange leading to formation of a variety of products ranging from chemical and structural heterostructures to completely transformed products. The concept of 'atomic templating' is once again observed to be central to the chemical and structural transformation in spite of change in bonding nature (ionic to covalent) and coordination (tetrahedral to octahedral) and the results are explained in this framework. Zincblende CdTe is reacted with Pb and Bi leading to formation of rocksalt PbTe and

metastable rocksalt BiTe with twin boundaries retained from parent CdTe, a strong signature of atomic templating. More interestingly, wurtzite CdSe, upon reaction with Pb, is transformed into rocksalt PbSe via hexagonal PbSe phase. The transformation mechanism is explained and the role of atomic templating is clearly underlined. With the help of first principles calculations using density functional theory, relative stability of obtained phases is calculated along with predicted physical properties aimed at specific applications.

Chapter 4 looks at chemical transformation in a covalent compound, GeTe, by replacing the chalcogenide species (Te) with Se in high temperature vapor phase reaction leading to formation of a metastable layered IV-VI semiconductor, $GeSe_2$ while preserving the morphology and close packed plane orientation of the parent compound. Chapter 5 discusses morphological transformation in wurtzite CdS nanobelts into periodically branched nanostructures upon heating in reactive atmospheres. The underlying mechanism is uncovered by performing similar experiments in environmental TEM at Brookhaven national lab and observing the morphological transformation in real time. A series of control experiments are devised to understand the role of crystal structured based anisotropy in the transformation mechanism and the results are discussed in detail.

Chapter 6 explores possibilities of future work in the area of chemical transformation in nanostructures with specific applications in mind. Replacement of group II B elements in II-VI semiconductors with group III A elements such as Indium may lead to many interesting possibilities since these elements can exist in both

octahedral and tetrahedral coordination. Also, chemical reactivity of highly popular and useful transition metal dichalcogenides such as MoS_2 and WSe_2 can open newer avenues in the field of materials engineering. Besides the work on chemical and morphological transformation in nanostructures, a large fraction of my effort at Penn was concentrated on developing a new characterization technique, optical second harmonic generation polarimetry, in studying crystallography and defect distribution in non-centrosymmetric nanostructures in collaboration with Dr. Ming-Liang Ren, a postdoc in our group. It is used to distinguish between wurtzite and zinc blende crystal structures in II-VI semiconducting compounds, to ascertain their growth orientation with respect to the close packed plane normal and to detect presence of twin boundaries while differentiating between upright and inverted twin boundaries in single-crystalline nanostructures. The results are verified by TEM. The technique and results are discussed in detail in Appendices A and B of this thesis.

Finally, Appendix C discusses our work in the field of resistive memory devices which was another area of research during my tenure at Penn. In collaboration with Dr. Moon Hyung Jang, a postdoc in our group, we developed an indirect method of tracking oxygen vacancy dynamics in $Pt/TiO_2/Pt$ resistive memory during the electroforming process eventually leading to formation of a conductive oxygen-vacancy filament. The oxygen vacancies were tracked via Pt migration owing to strong metal-support interaction between Pt metal and reduced TiO_2 in region with high oxygen vacancy concentration thereby providing a concrete proof of a widely believed electroforming mechanism. The experiments consist of in-situ TEM and atmosphere dependent

switching coupled with ex-situ TEM observations. The mechanism of electroforming is explained in detail.

1.8 References

1. W. Lu and C.M. Lieber, J. Phys. D. 39 (2006) p.R387.

2. R.S. Wagner and W.C. Ellis, Appl. Phys. Lett. 4 (1964) p.89.

3. Y. Cui, Z. Zhong, D. Wang, W.U. Wang and C.M. Lieber, Nano Lett. 3 (2003) p.149.

4. Y. Huang, X. Duan, Y. Cui, L.J. Lauhon, K.-H. Kim and C.M. Lieber, Science 294 (2001) p.1313.

5. H. Yan, H.S. Choe, S. Nam, Y. Hu, S. Das, J.F. Klemic, J.C. Ellenbogen and C.M. Lieber, Nature 470 (2011) p.240.

6. P.-H. Yeh, Z. Li and Z.L. Wang, Adv. Mater. 21 (2009) p.4975.

7. G.-J. Zhang, J.H. Chua, R.-E. Chee, A. Agarwal, S.M. Wong, K.D. Buddharaju and N. Balasubramanian, Biosens. Bioelectron. 23 (2008) p.1701.

8. Q. Wan, Q.H. Li, Y.J. Chen, T.H. Wang, X.L. He, J.P. Li and C.L. Lin, Appl. Phys. Lett. 84 (2004) p.3654.

9. U. Cvelbar, K. Ostrikov, A. Drenik and M. Mozetic, Appl. Phys. Lett. 92 (2008) p.133505.

10. B. Wang, L.F. Zhu, Y.H. Yang, N.S. Xu and G.W. Yang, J. Phys. Chem. C 112 (2008) p.6643.

11. X. Wang, J. Song, J. Liu and Z.L. Wang, Science 316 (2007) p.102.

12.Z.L. Wang and J. Song, Science 312 (2006) p.242.

13. J. Bao, M.A. Zimmler, F. Capasso, X. Wang and Z.F. Ren, Nano Lett. 6 (2006) p.1719.

14. R. Konenkamp, R.C. Word and C. Schlegel, Appl. Phys. Lett. 85 (2004) p.6004.

15. X. Duan, Y. Huang, R. Agarwal and C.M. Lieber, Nature 421 (2003) p.241.

16. M. Law, L.E. Greene, J.C. Johnson, R. Saykally and P. Yang, Nat. Mater. 4 (2005) p.455.

17. C.K. Chan, H. Peng, G. Liu, K. McIlwrath, X.F. Zhang, R.A. Huggins and Y. Cui, Nat. Nanotechnol. 3 (2008) p.31.

18. M. Koto, P.W. Leu and P.C. McIntyre, J. Electrochem. Soc. 156 (2009) p.K11.

19 S.H. Lee, H.J. Lee, D. Oh, S.W. Lee, H. Goto, R. Buckmaster, T. Yasukawa, T. Matsue, S.-K. Hong, H. Ko, M.-W. Cho and T. Yao, J. Phys. Chem. B 11 (2006) p.3856.

20. O. Englander, D. Christensen, J. Kim, L. Lin and S.J.S. Morris, Nano Lett. 5 (2005) p.705.

21. P.A. Smith, C.D. Nordquist, T.N. Jackson, T.S. Mayer, B.R. Martin, J. Mbindyo and T.E. Mallouk, Appl. Phys. Lett. 77 (2000) p.1399.

22. C.S. Lao, J. Liu, P. Gao, L. Zhang, D. Davidovic, R. Tummala and Z.L. Wang, Nano Lett. 6 (2006) p.263.

23. E.M. Freer, O. Grachev, X. Duan, S. Martin and D.P. Stumbo, Nat. Nanotechnol. 5 (2010) p.525.

24. S. Raychaudhuri, S.A. Dayeh, D. Wang and E.T. Yu, Nano Lett. 9 (2009) p.2260.

25. Z. Fan, J.C. Ho, Z.A. Jacobson, R. Yerushalmi, R.L. Alley, H. Razavi and A. Javey, Nano Lett. 8 (2008) p.20.

26. Y. Sun and J.A. Rogers, Nano Lett. 4 (2004) p.1953.

27. K.J. Lee, J. Lee, H. Hwang, Z.J. Reitmeier, R.F. Davis, J.A. Rogers and R.G. Nuzzo, Small 1 (2005) p.1164.

28. R. Agarwal, K. Ladavac, Y. Roichman, G. Yu, C. Lieber and D. Grier, Opt. Express 13 (2005) p.8906.

29. P.J. Pauzauskie, A. Radenovic, E. Trepagnier, H. Shroff, P. Yang and J. Liphardt, Nat. Mater. 5 (2006) p.97.

30. A. van der Horst, A.I. Campbell, L.K. van Vugt, D.A. Vanmaekelbergh, M. Dogterom and A. van Blaaderen, Opt. Express 15 (2007) p.11629.

31. A.T. Ohta, A. Jamshid, P.J. Pauzauskie, H.Y. Hsu, P. Yang and M.C. Wu, Trapping and transport of silicon nanowires using lateral-field optoelectronic tweezers, in Conference on Lasers and Electro-Optics, Opt. Soc. Am., 2007.

32. F. Kim, S. Kwan, J. Akana and P. Yang, J. Am. Chem. Soc. 123 (2001) p.4360.

33. S. Acharya, A.B. Panda, N. Belman, S. Efrima and Y. Golan, Adv. Mater. 18 (2006) p.210.

34. D. Whang, S. Jin, Y. Wu and C.M. Lieber, Nano Lett. 3 (2003) p.1255.

35. Y. Jung, D.-K. Ko and R. Agarwal, Nano Lett. 7 (2006) p.264.

36. D. Wang, F. Qian, C. Yang, Z. Zhong and C.M. Lieber, Nano Lett. 4 (2004) p.871.

37. K.A. Dick, K. Deppert, M.W. Larsson, T. Mårtensson, W. Seifert, L.R. Wallenberg and L. Samuelson, Nat. Mater. 3 (2004) p.380.

38. A. Javey, S.W. Nam, R.S. Friedman, H. Yan and C.M. Lieber, Nano Lett. 7 (2007) p.773.

39. S.W. Nam, X. Jiang, Q. Xiong, D. Ham and C.M. Lieber, PNAS 106 (2009) p.21035.

40. D.H. Son, S.M. Hughes, Y. Yin and A.P. Alivisatos, Science 306 (2004) p.1009.

41. G.D. Moon, S. Ko, Y. Min, J. Zeng, Y. Xia and U. Jeong, Nano Today 6 (2011) p.186.

42. S. Feng and R. Xu, Acc. Chem. Res. 34 (2001) p.239.

43. R.D. Robinson, B. Sadtler, D.O. Demchenko, C.K. Erdonmez, L.W. Wang and A.P. Alivisatos, Science 317 (2007) p.355.

44. D.O. Demchenko, R.D. Robinson, B. Sadtler, C.K. Erdonmez, A.P. Alivisatos and L.-W. Wang, ACS Nano 2 (2008) p.627.

45. P.K. Jain, L. Amirav, S. Aloni and A.P. Alivisatos, J. Am. Chem. Soc. 132 (2010) p.9997.

46. B. Sadtler, D.O. Demchenko, H. Zheng, S.M. Hughes, M.G. Merkle, U. Dahmen, L.-W. Wang and A.P. Alivisatos, J. Am. Chem. Soc. 131 (2009) p.5285.

47. G.D. Moon, S. Ko, Y. Xia and U. Jeong, ACS Nano 4 (2010) p.2307.

48. U. Jeong, Y. Xia and Y. Yin, Chem. Phys. Lett. 416 (2005) p.246.

49. U. Jeong, P.H.C. Camargo, Y.H. Lee and Y. Xia, J. Mater. Chem. 16 (2006) p.3893.

50. R. Ma, Y. Wang and T.E. Mallouk, Small 5 (2009) p.356.

51. L. Dloczik, R. Engelhardt, K. Ernst, S. Fiechter, I. Sieber and R. Könenkamp, Appl. Phys. Lett. 78 (2001) p.3687.

52. L. Dloczik and R. Könenkamp, Nano Lett. 3 (2003) p.651.

53. D.S. Koktysh, J.R. McBride, S.K. Dixit, L.C. Feldman and S.J. Rosenthal, Nanotechnology 18 (2007) p.495607.

54. Y. Xie, P. Yan, J. Lu, Y. Qian and S. Zhang, Chem. Commun. (1999) p.1969.

55. H.-S. Shim, V.R. Shinde, J.W. Kim, T.P. Gujar, O.-S. Joo, H.J. Kim and W.B. Kim, Chem. Mater. 21 (2009) p.1875.

56. V.R. Shinde, T.P. Gujar, T. Noda, D. Fujita, C.D. Lokhande and O.-S. Joo, J. Phys. Chem. C 113 (2009) p.14179.

57. A.A. Eliseev, M.V. Chernysheva, N.I. Verbitskii, E.A. Kiseleva, A.V. Lukashin, Y.D. Tretyakov, N.A. Kiselev, O.M. Zhigalina, R.M. Zakalyukin, A.L. Vasiliev, A.V. Krestinin, J.L. Hutchison and B. Freitag, Chem. Mater. 21 (2009) p.5001.

58. J.Y. Lee, D.S. Kim and J. Park, Chem. Mater. 19 (2007) p.4663.

59. W.I. Park, H.S. Kim, S.Y. Jang, J. Park, S.Y. Bae, M. Jung, H. Lee and J. Kim, J. Mater. Chem. 18 (2008) p.875.

60. B. Zhang, Y. Jung, H.-S. Chung, L.K. van Vugt and R. Agarwal, Nano Lett. 1 (2010) p.149.

CHAPTER 2: Atomic Templating via Anion Exchange in II-VI Semiconducting Nanostructures

Adapted and reprinted in parts from:

R. Agarwal, N. M. Krook, M.-L. Ren, L.Z. Tan, W. Liu, A. M. Rappe and R. Agarwal, "Atomic Templating via Anion Exchange in II-VI Semiconducting Nanostructures" Under preparation for submission.

2.1 Synthesis and Characterization of II-VI Semiconducting Nanostructures

All nanostructures involved in various experiments throughout this thesis were synthesized via the Vapor-Liquid-Solid (VLS) mechanism in a chemical vapor deposition (CVD) system at elevated temperatures under an inert gas flow. The specific details of the growth and characterization of concerned nanostructures are mentioned below.

2.1.1 Synthesis of CdS Nanostructures

CdS nanowires and nanobelts were synthesized in a quartz tube furnace using evaporation of 99.995% pure CdS powder (Sigma-Aldrich). 5 mg of CdS powder was placed in a quartz boat in the middle of the tube, and Si substrates covered by a 8 nm thick Au layer using e-beam evaporation were placed 15 cm downstream (referenced to the middle of the tube). The tube was evacuated to 20 mTorr and argon carrier gas was introduced at a flow of 15 SCCM to reach a stable pressure of 5 Torr. The tube was rapidly heated to 760 °C and maintained there for 120 minutes after which the furnace was cooled by a forced airflow.

2.1.2 Synthesis of CdSe Nanostructures

CdSe nanowires and nanobelts were synthesized in a quartz tube furnace using evaporation of 99.995% pure CdSe powder (Sigma-Aldrich). 5 mg of CdSe powder was placed in a quartz boat in the middle of the tube, and Si substrates covered by a 8 nm thick Au layer using e-beam evaporation were placed 15 cm downstream (referenced to the middle of the tube). The tube was evacuated to 20 mTorr and argon carrier gas was introduced at a flow of 15 SCCM to reach a stable pressure of 5 Torr. The tube was rapidly heated to 850 °C and maintained there for 120 minutes after which the furnace was cooled by a forced airflow.

2.1.3 Synthesis of CdTe Nanostructures

CdTe nanowires and nanobelts were synthesized in a quartz tube furnace using evaporation of 99.995% pure CdTe powder (Sigma-Aldrich). 5 mg of CdTe powder was placed in a quartz boat in the middle of the tube, and Si substrates covered by a 8 nm thick Au layer using e-beam evaporation were placed 15 cm downstream (referenced to the middle of the tube). The tube was evacuated to 20 mTorr and argon carrier gas was introduced at a flow of 15 SCCM to reach a stable pressure of 5 Torr. The tube was rapidly heated to 750 °C and maintained there for 120 minutes after which the furnace was cooled by a forced airflow.

2.1.4 Characterization of Nanostructures

As-grown nanostructures were dry-transferred to a TEM compatible platform (lacey carbon on copper support or SiN_x membrane on Si support) and analyzed for structure via selected area electron diffraction (SAED) and high-resolution TEM imaging and for chemical composition via energy dispersive X-ray spectroscopy (EDS) on the JEOL 2010F TEM. CdS and CdSe nanostructures always grow in the form of wires and belts in the wurtzite crystal structure (Figure 2.1) whereas CdTe nanowires and nanobelts mostly grow in the zincblende crystal structure, often with twin boundaries along the closed packed plane of the crystal structure ({111} twin boundaries) as shown in Figure 2.2 and Figure 2.3. However, CdTe nanostructures may also grow in the wurtzite crystal structure and sometimes as heterostructure of zincblende/wurtzite.

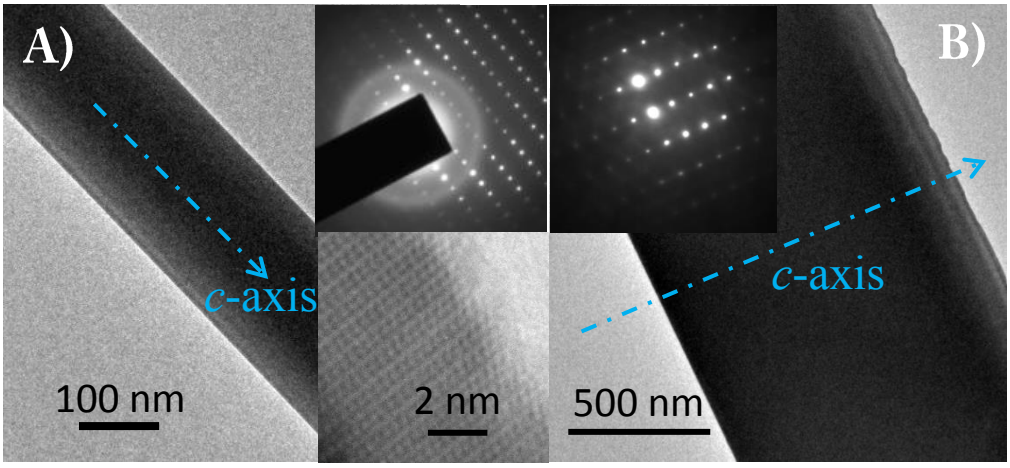

Figure 2.1 A) TEM micrograph of a CdS NW grown along the *c*-axis confirmed by the selected area electron diffraction (SAED) pattern (top inset) and high resolution TEM image (bottom inset). B) TEM micrograph of CdS NW. Inset: SAED pattern of the NW indicating WZ crystal structure and $c \perp$NW growth orientation.

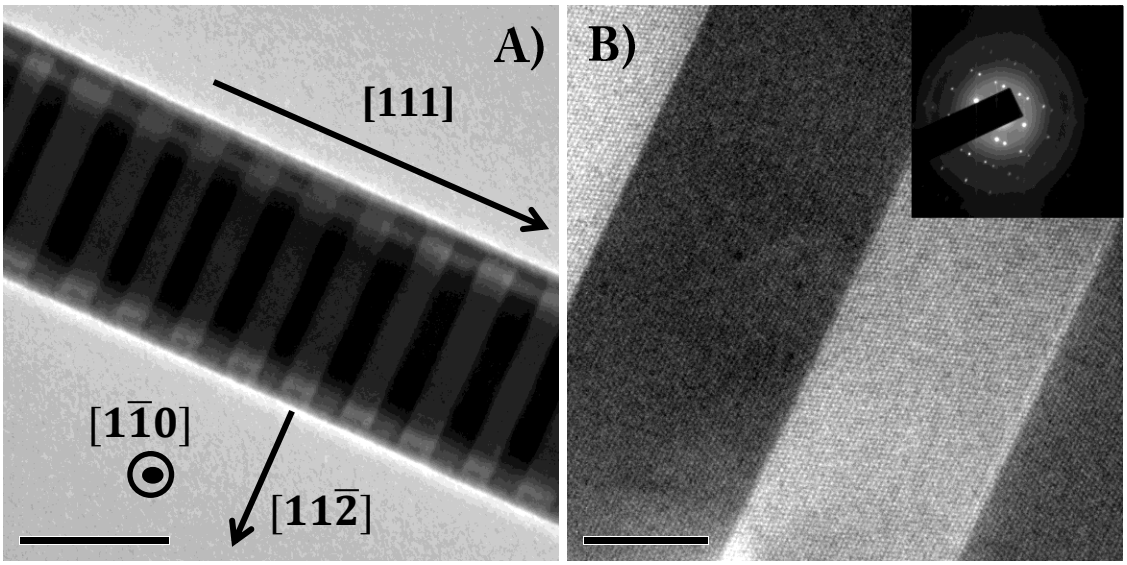

Figure 2.2 A) TEM micrograph of an as-grown CdTe nanowire growing along [111] with periodic twin boundaries running across the diameter throughout the length. B) HRTEM micrograph of the same nanowire showing phase contrast across twin boundaries in separate domains. Inset: SAED pattern of the same nanowire.

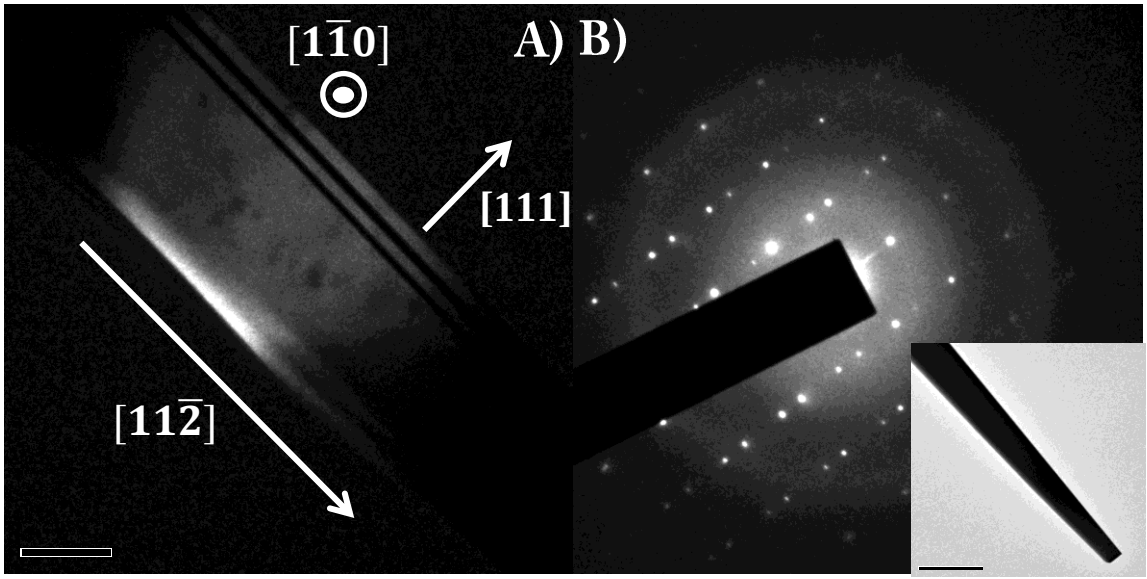

Figure 2.3 A) DF-TEM micrograph of an as-grown CdTe nanobelt growing along [112] with twin boundaries running along the length of the belt. B) SAED pattern of the same nanobelt confirming ZB crystal structure with twin boundaries present. Inset: BF-TEM micrograph of the nanobelt.

2.2 Introduction

Ion-exchange, defined as chemical substitution of one ionic species in a material with another, has been utilized as an effective route for chemical transformation of nanostructures to design novel materials with unique physical, chemical and structural properties and to understand the distinctive transformation mechanism at the nanoscale[1-13]. However, most of the work has focused on cation exchange in sub-10 nm crystals in solution phase thereby limiting its scope in understanding chemical transformations in intermediate length scale nanostructures (>100 nm) such as nanowires (NWs) and nanobelts (NBs), which find extensive applications owing to the ease of growth, manipulation and device fabrication. We previously reported cation exchange in CdS NWs with Zn via high temperature vapor phase reaction thus enabling kinetically controlled and size dependent chemical transformation products ranging from alloyed NWs to metal-semiconductor heterostructures which highlights the importance of chemical transformation in nanostructures for the synthesis of novel materials[14]. Moreover, there is limited emphasis on anion exchange[15-21] owing to anionic species forming the rigid crystal framework and possessing sluggish diffusivity thus rendering the reaction structurally and energetically challenging to achieve[22]. In this chapter, we present anion exchange in II-VI semiconducting nanostructures via high temperature vapor phase reaction while retaining the atomic template of the parent compound in the form of its crystal structure, defect distribution and morphology thus permitting us to engineer well-known semiconductor compounds in kinetically controlled phases which are difficult to obtain otherwise. II-VI semiconductor nanostructures were selected as the model system since the nature of bonding is predominantly ionic in these materials[23] and

they have been extensively studied in the last two decades for interesting physical properties thereby finding applications in a variety of fields[24-28].

2.3 Anion Exchange in CdS with Se

To explore the potential of anion exchange in chemical transformation of nanostructures and to study the accompanying evolution in crystal structure and physical properties, single-crystalline wurtzite (WZ) CdS nanostructures were synthesized via the vapor-liquid-solid (VLS) method in a tube furnace set-up[27] and anion exchange was performed on as-grown CdS nanostructures with Se. As-grown CdS nanostructures were dry transferred to a Si TEM grid with an electron beam transparent 50 nm thick SiN_x window at the center and the grid was placed on the downstream side of the furnace such that the reaction temperature was uniform throughout. 5 mg of the precursor (Se) in powdered form (Sigma-Aldrich) was loaded at the center of the furnace in a quartz tube and the furnace was pumped down to 20 mTorr (Figure 2.4). After flushing several times with Ar, the system was stabilized under a continuous flow of 15 SCCM and 5 Torr of Ar. The reaction temperature varied for different experiments but the reaction time was fixed at 1 hour after which the furnace was opened and left to cool until it reached room temperature.

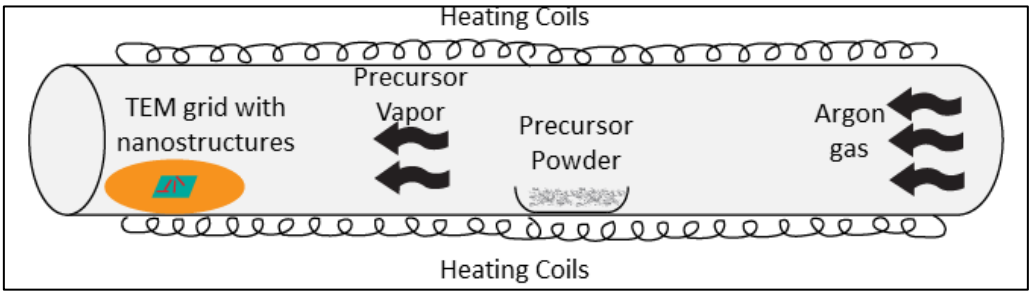

Figure 2.4 Schematic of the experimental set-up for anion exchange in a tube furnace.

The experimental conditions were optimized after extensive trials involving variation of precursor type, quantity, reaction temperature and time and it was established that reaction time and temperature were the two most important factors which determined the final product. Overheating for delayed periods caused excessive sublimation and underheating for short durations lead to negligible chemical transformation. Anion exchange reaction at 600 ^{0}C for one hour leads to complete chemical transformation of CdS into CdSe while retaining the single-crystalline WZ structure, morphology and growth orientation of the parent nanostructure (Figure 2.5 A-D). The results were reproduced for a wide range of sizes and morphologies of WZ CdS ranging from sub-100 nm NWs to 500 nm wide NBs. Raman spectroscopy, performed on a confocal micro-Raman system equipped with a 532 nm continuous-wave laser at room temperature and pressure, of a completely transformed CdSe nanostructure shows that longitudinal optical (LO) phonon peaks corresponding to pure CdSe[29] were present while those corresponding to pure CdS[30] or CdS_xSe_{1-x} alloy[31] were absent confirming presence of only Cd-Se bonds in the product (Figure 2.5 E). Photoluminescence (PL) spectroscopy, carried out on individual nanostructures using a home-built optical set-up with a continuous-wave argon ion laser at 458 nm, of a completely transformed CdSe NW indicates band edge emission corresponding to pure CdSe[32] (~716 nm) (Figure 2.5 F) confirming that the physical properties, such as the band gap of the anion exchanged material, matched WZ CdSe. Achieving complete chemical transformation in such large nanostructures via anion exchange while retaining the structural integrity of the parent material has been challenging thus far and this is one important result in the field. It is

interesting to note that while the anions, structural pillars of the lattice, were being replaced; the cations remained frozen in their position thereby retaining the single-crystalline structure of the parent compound.

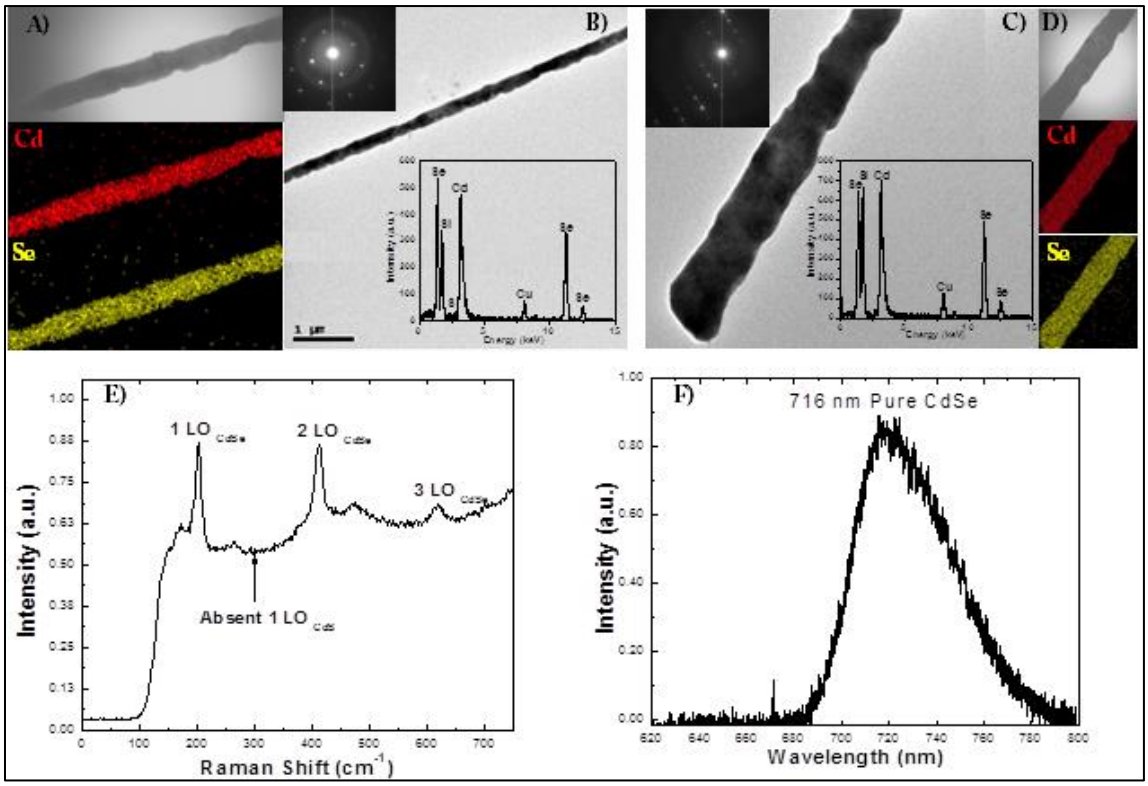

Figure 2.5 Characterization of nanostructures after undergoing complete anion exchange from WZ CdS into WZ CdSe. A) BF-STEM micrograph and EDS map scan of a chemically transformed CdSe NW showing uniform anion exchange in starting CdS. B) BF-TEM micrograph of the same NW confirming morphological integrity along the entire length after anion exchange. Upper Left Inset: SAED pattern corresponding to single-crystalline pure WZ CdSe NW grown along c-axis. Bottom Right Inset: EDS point scan of the NW confirming complete chemical transformation from CdS to CdSe with no residual S. C) BF-TEM micrograph of a NB after undergoing complete chemical transformation. Upper Right Inset: SAED pattern corresponding to single-crystalline WZ CdSe NB grown at an angle to c-axis. Bottom Right Inset: EDS point scan of the NB confirming complete chemical transformation from CdS to CdSe. D) BF-STEM micrograph and EDS map of the same CdSe NB showing uniform chemical transformation. E) Raman spectrum of a completely transformed CdSe nanostructure showing LO phonon peaks corresponding to only Cd-Se bond. F) PL spectrum of a completely transformed CdSe nanostructure showing band edge emission corresponding to pure CdSe.

2.4 Anion Exchange in CdTe with Se

Motivated by lattice framework preserving anion exchange mechanism in WZ CdS, the concept was extended to other phases of II-VI semiconductors in order to obtain metastable crystal structures which are not possible to obtain during conventional growth processes such as VLS mechanism. CdTe and CdSe are thermodynamically stable in zincblende (ZB) crystal structure whereas CdS is stable in WZ crystal structure under room temperature and pressure[33, 34]. In spite of thermodynamic stability of ZB CdSe at room temperature and pressure, it typically grows in WZ phase through most bottom-up synthesis techniques[35, 36]. Numerous efforts have focused on synthesizing CdSe and CdS in zincblende (ZB) crystal structure to study novel semiconducting properties[36-44]. However, it has met with limited success, mostly in small nanocrystals (<10 nm), and is yet to be reproduced in larger nanostructures such as NWs and NBs. Considering the lattice framework preserving nature of the anion exchange mechanism discussed before, it was expected that complete chemical transformation in ZB CdTe nanostructures by introducing Se/S will produce ZB CdSe/CdS. As-grown CdTe nanostructures, synthesized via VLS mechanism[45], often possess planar growth defects such as twin boundaries (TBs) owing to low stacking fault energy of the material[46] (Figure 2.2 and 2.3). CdTe NW with periodic TBs was chosen (Figure 2.6 A) for anion exchange reaction with Se (450 ºC) and the same nanostructure was characterized both before and after the anion exchange reaction through a TEM comparative study to understand the evolution of crystal structure and defect distribution as a function of chemical transformation. The resulting NW, retained the single-crystalline ZB crystal structure, the <111> growth direction and periodic TBs of the parent material (Figure 2.6 B) upon undergoing

complete chemical transformation into CdSe, confirmed by energy dispersive X-ray spectroscopy (EDS) point scan (Figure 2.6 C). Raman and PL spectroscopy also confirm the complete chemical transformation by displaying LO phonon and band-edge emission PL peaks corresponding to pure CdSe[47, 48] (Figure 2.6 D-E). This result is universal for all ZB CdTe nanostructures, NW and NBs, with and without TBs.

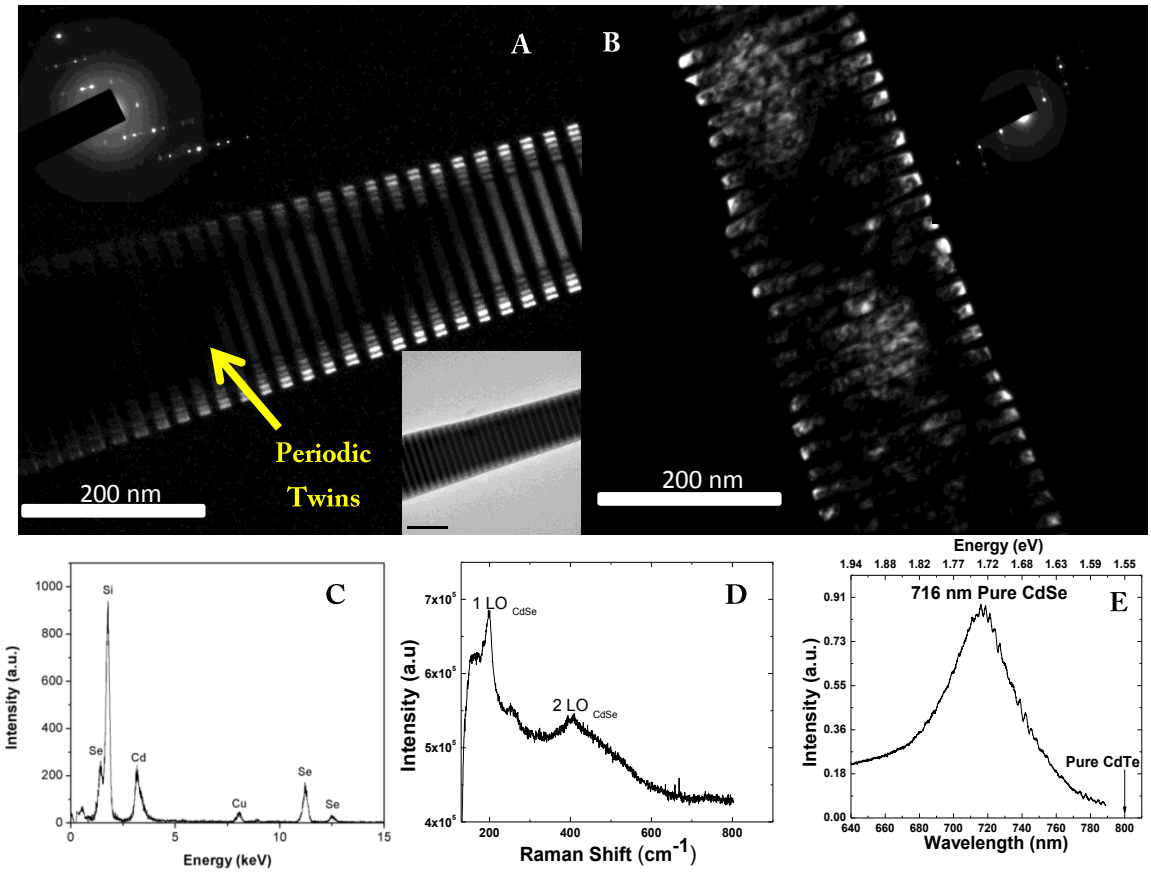

Figure 2.6 Characterization of NW after complete anion exchange from ZB CdTe into ZB CdSe. A) Dark-field TEM image of a periodically twinned CdTe NW before anion exchange. Upper Left Inset: SAED pattern confirming the ZB crystal structure, twinning and <111> growth axis. Bottom Right Inset: Bright-field TEM micrograph of the same NW. B) Dark-field TEM micrograph of the same NW after complete anion exchange into CdSe. Inset: SAED pattern confirming retention of the ZB crystal structure, twinning and <111> growth axis with lattice parameters matching pure ZB CdSe. C) EDS point scan of the above NW confirming complete chemical transformation into CdSe. D) Raman spectrum confirming complete chemical transformation. E) PL spectrum displaying band edge emission corresponding to pure CdSe.

2.5 Anion Exchange in CdTe with S

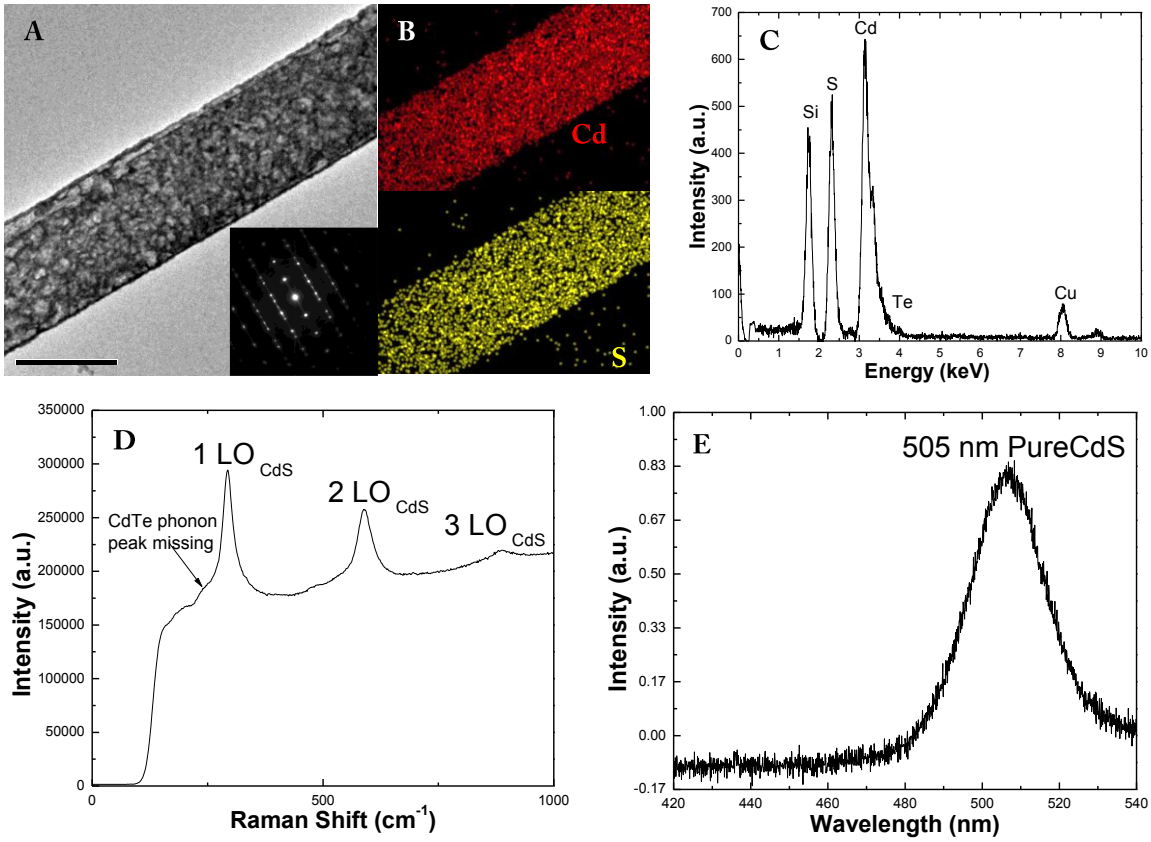

Figure 2.7 Characterization of NB after undergoing complete anion exchange from ZB CdTe into ZB CdS. A) Bright-field TEM micrograph of a NB after undergoing complete chemical transformation. Inset: SAED pattern of the NB confirming retention of ZB crystal structure, twinning and <112> growth axis. B) EDS map scan of the NB showing uniform chemical transformation into CdS. C) EDS point scan of the NB confirming complete chemical transformation. D) Raman spectrum displaying LO phonon peaks corresponding only to Cd-S bond thereby confirming complete chemical transformation. E) PL spectrum displaying band edge emission corresponding to pure CdS.

On performing anion exchange under similar experimental conditions on CdTe nanostructures with S, complete chemical transformation into single-crystalline ZB CdS was observed while retaining the TBs and <112> growth direction of the parent NB (Figure 2.7). As discussed before, retention of the parent crystal structure upon chemical transformation was expected, but the retention of planar defects such as twin boundaries

reaffirms the lattice preserving nature of the anion exchange reaction. This is an important result since it highlights the role of anion exchange based chemical transformation in phase engineering of metastable structures which are challenging to obtain otherwise with the additional ability to retain defect distribution of the parent material which promises very interesting physical properties in applications ranging from nanoscale photocatalysis to thermoelectricity[49, 50].

2.6 Kinetically Controlled Anion Exchange Reaction

To further understand the mechanism behind this lattice framework preserving chemical transformation, a series of control experiments were designed to study anion exchange in WZ CdS model system by introducing Se. This model system was chosen since the forward reaction (CdS converting into CdSe) is thermodynamically unfavorable and therefore can be kinetically controlled[52]. Anion exchange was performed by lowering the reaction temperature thereby decelerating the transformation kinetics while maintaining all other experimental conditions constant to observe step by step structural and chemical evolution. Upon performing anion exchange at 300 ^{0}C in a ~200 nm diameter WZ CdS NW, we observed that the NW possesses a rough morphology with periodic protrusions on the surface (Figure 2.8 A). Selected area electron diffraction (SAED) pattern reveals single-crystalline WZ structure with split diffraction spots corresponding to pure CdS and CdSe (Figure 2.8 A inset). EDS line scan along the radial direction indicates that the NW possesses a compositional gradient, with Se rich phase on the surface and S rich phase towards the core indicating incomplete anion exchange reaction (Figure 2.8 B). However, upon performing anion exchange at 450 ºC on another

~200 nm diameter WZ CdS NW, we observe comparatively smoother surface morphology and uniform lattice parameter (indiscernible diffraction spot splitting) throughout the material (Figure 2.8 C). EDS line scan along the radial direction indicates a compositional gradient however the penetration depth of Se towards the core is higher than the NW obtained via anion exchange reaction performed at 300 ^{0}C (Figure 2.8 D).

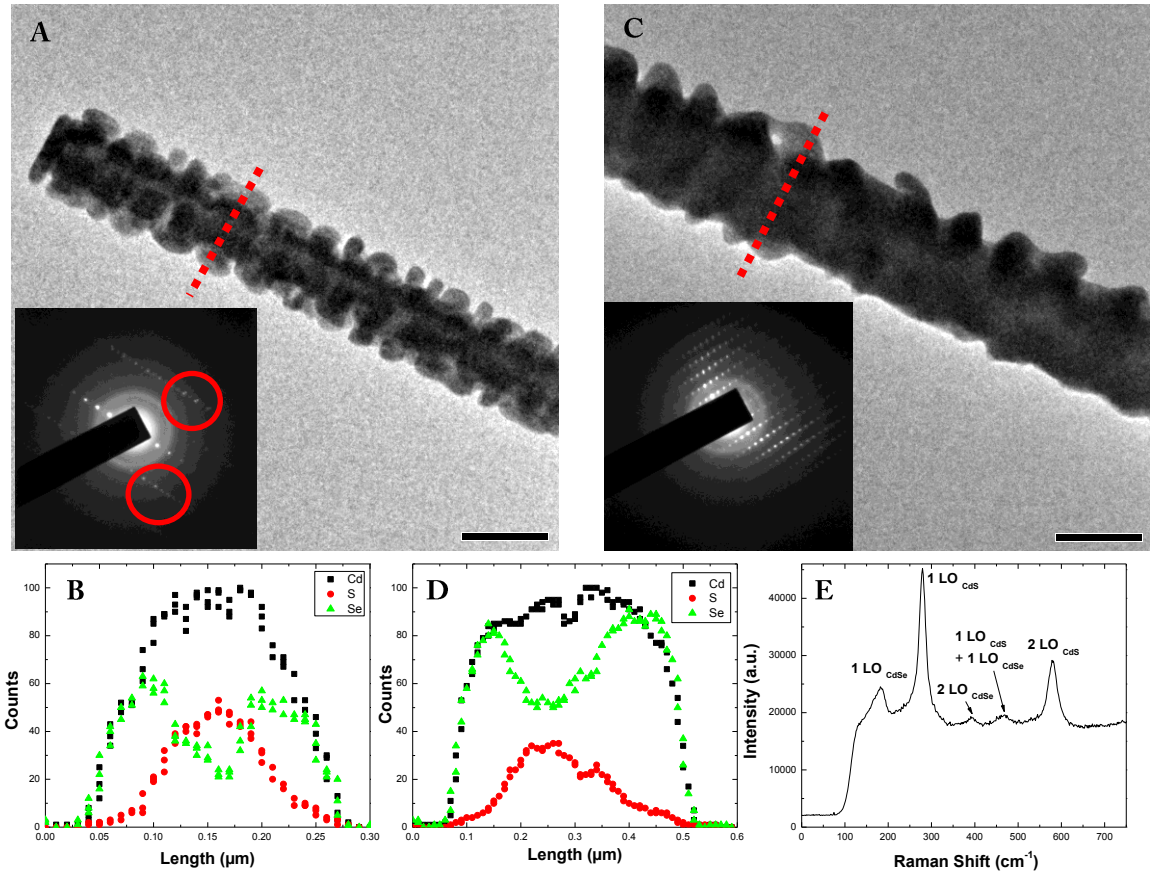

Figure 2.8 Characterization of nanostructures after undergoing partial anion exchange from CdS to CdS_xSe_{1-x}. A) Bright-field TEM micrograph of CdS_xSe_{1-x} NW after anion exchange at 300 ^{0}C. Inset: SAED pattern of the NW confirming single-crystalline WZ structure with split and elongated spots (red circles). B) EDS line scan of the same NW confirming the core-shell morphology of the alloyed NW (along the dotted line in A). C) Bright-field TEM micrograph of CdS_xSe_{1-x} NW after anion exchange at 450 ^{0}C. Inset: SAED pattern of the NW confirming single-crystalline WZ structure of CdS_xSe_{1-x}. D) EDS line scan of the same NW confirming the core-shell morphology of the alloyed NW (taken along the dotted line in C). E) Raman spectrum of an alloyed CdS_xSe_{1-x} NW showing LO phonon peaks corresponding to both Cd-S and Cd-Se bonds.

Raman spectroscopy of the NW indicates LO phonon peaks corresponding to Cd-S and Cd-Se bond in a CdS_xSe_{1-x} type alloy besides a sum frequency peak (~480 cm^{-1}) (Figure 2.8 E) that corresponds to a two mode behavior alloy of the type CdS_xSe_{1-x}[31]. Such control experiments underline the importance of temperature dependent diffusion and reaction kinetics in driving the anion exchange reaction forward. Also, controlled chemical transformation via anion exchange in large nanostructures to produce compositionally gradient materials is a promising technique to engineer novel materials which may offer very interesting physical properties (Figure 2.9).

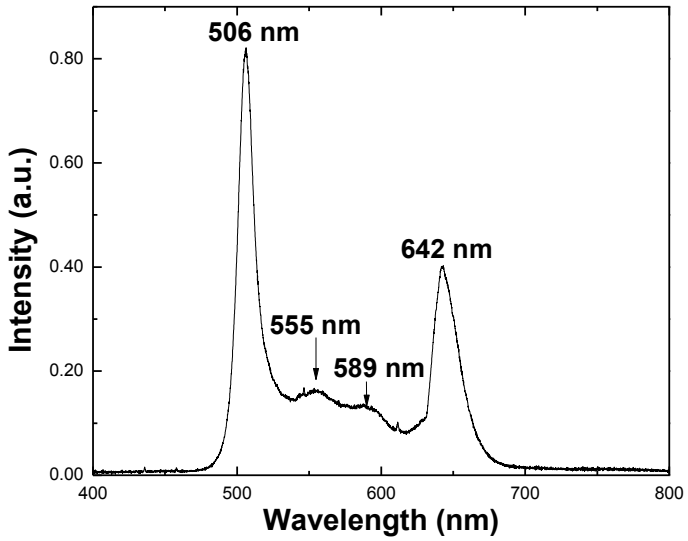

Figure 2.9 PL spectrum of a partially anion exchanged CdS_xSe_{1-x} NW displaying band edge emission corresponding to regions with different stoichiometry (x) ranging from pure CdS (505 nm) to highly red shifted peak at 642 nm corresponding to CdS_xSe_{1-x}.

2.7 Anion Exchange Reaction Mechanism

Based on the results obtained from partial and complete chemical transformation in WZ CdS with Se, we propose the following hypothesis for the observed anion exchange reaction. The reaction temperature influences the flux of the reactant species (Se vapor) that the sample experiences, the driving force for the anion exchange to

proceed forward and the diffusivity of atoms in the nanostructure, all of which determine the chemical composition of the final product. At a particular reaction temperature, CdS nanostructures (Figure 2.10 A) will be exposed to a constant flux of Se vapor which will react and replace S^{2-} through anion exchange in CdS on the surface, thereby creating domains of Se rich CdS_xSe_{1-x} alloy and the excess vapor will condense as amorphous selenium (a-Se) on top creating protrusions (Figure 2.10 B). Se can also occupy S vacancies in CdS. Even though transformation of CdS into CdSe is thermodynamically unfavorable, excess Se source and high temperature provide sufficient kinetic drive for the forward reaction. Also, since the carrier gas is capable of instantaneously transporting away rejected S vapor, which is a byproduct of the forward anion exchange reaction, the system acts as an efficient sink for S. This helps in pushing the reaction forward and not letting the reverse anion exchange reaction (CdSe transforming into CdS) take place at all. The initial CdS_xSe_{1-x} domain spacing and size will be directly proportional to the incoming Se vapor flux which is dictated by the reaction temperature. Domain growth of CdS_xSe_{1-x} will involve outward diffusion of Se^{2-} to the S^{2-} rich regions while fresh Se^{2-} is introduced into the system through constant anion exchange (Figure 2.10 C). Also, surface diffusion, which is faster than bulk diffusion[51], will lead to preferential chemical transformation at the surface before the core of the nanostructure thereby creating core-shell type morphology instead of an axial heterostructure (Figure 2.10 D). Since the source of Se vapor can be assumed to be infinite with respect to the limited nanostructure volume available, the anion exchange reaction and CdS_xSe_{1-x} domain growth will continue until heating is stopped (Figure 2.10 E). Therefore, at the lowest reaction

temperature (300 ^{0}C), pure CdS at the core is preserved and is surrounded by a shell of CdS_xSe_{1-x} alloy which explains the diffraction spot splitting in SAED pattern (Figure 2.8 A inset). The rough surface morphology is owing to Cd^{2+} diffusing from nearby regions into the accumulated amorphous Se protrusions, thus creating Se rich CdS_xSe_{1-x} in the outermost shell. At an intermediate reaction temperature (450 ^{0}C), the entire nanostructure transforms into CdS_xSe_{1-x} alloy with a radial composition gradient which allows the system to relax close to an intermediate lattice parameter between pure CdS and CdSe. The surface roughness is relatively lower since Se condensation rate will be smaller at higher temperatures and the deposited amorphous Se will be consumed at a faster rate through anion exchange. At the highest reaction temperature (600 ^{0}C), the reaction front proceeds inwards all the way to the core, completely transforming CdS into CdSe and the observed surface roughness, which is the least out of all the three reactions, can be explained by negligible a-Se deposition on the surface. Another important factor responsible for surface roughness is lattice expansion by ~ 4.5% as CdS converts into CdSe. Since the fully transformed nanostructures show no signature of any residual sulfur, it is believed to diffuse outwards to the surface and sublimate. At reaction temperatures below 300 ^{0}C, no anion exchange is observed for similar reaction duration since there is not enough kinetic drive to push forward both the chemical substitution reaction and atomic diffusion. At reaction temperatures higher than 600 ^{0}C, the nanostructures sublimate possibly owing to very fast chemical substitution reaction thereby causing large scale bond breaking and thereby destabilizing the anion lattice framework. The above hypothesis establishes the utility of vapor phase anion exchange

reactions in chemically transforming large nanostructures to fully transformed or compositionally graded nanomaterials while preserving the lattice framework of the parent material which allows synthesis of metastable phases of materials at the nanoscale

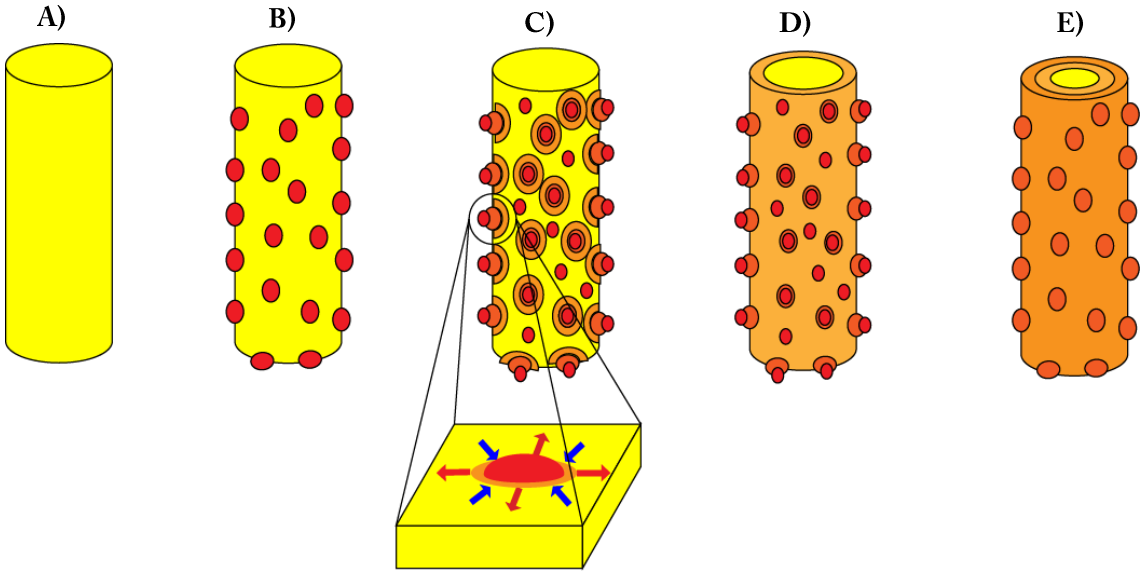

while preserving defect density of the parent material.

Figure 2.10 A) Starting CdS nanostructure with smooth surfaces and well defined morphology. B) Condensation of the anion precursor vapor (Se) on the surface of the nanostructure and beginning of anion exchange with surface ions (S^{2-}). C) Domain formation of CdS_xSe_{1-x} alloy spreading through surface and bulk anion exchange. Inset: Zoomed up schematic of surface diffusion process of various chemical species. D) Complete transformation of the surface into CdSe and the anion exchange reaction progressing towards the core. E) The reaction stops after either the precursor is exhausted or the system is cooled down.

2.8 Conclusion

We have developed anion exchange as a novel chemical transformation route to synthesize well-known compounds in thermodynamically less stable crystal phases with precise defect distribution which is retained from the parent nanostructure (Figure 2.11). Besides, this work answers fundamental questions in the field of controlled chemical

reactions at the nanoscale while preserving the structural integrity of the material in spite of substituting anions which are considered structural pillar in a crystal framework. This method, which we like to call "atomic templating", is a promising tool that can hopefully be extended beyond II-VI semiconductors to engineer exotic materials at the nanoscale for a variety of applications.

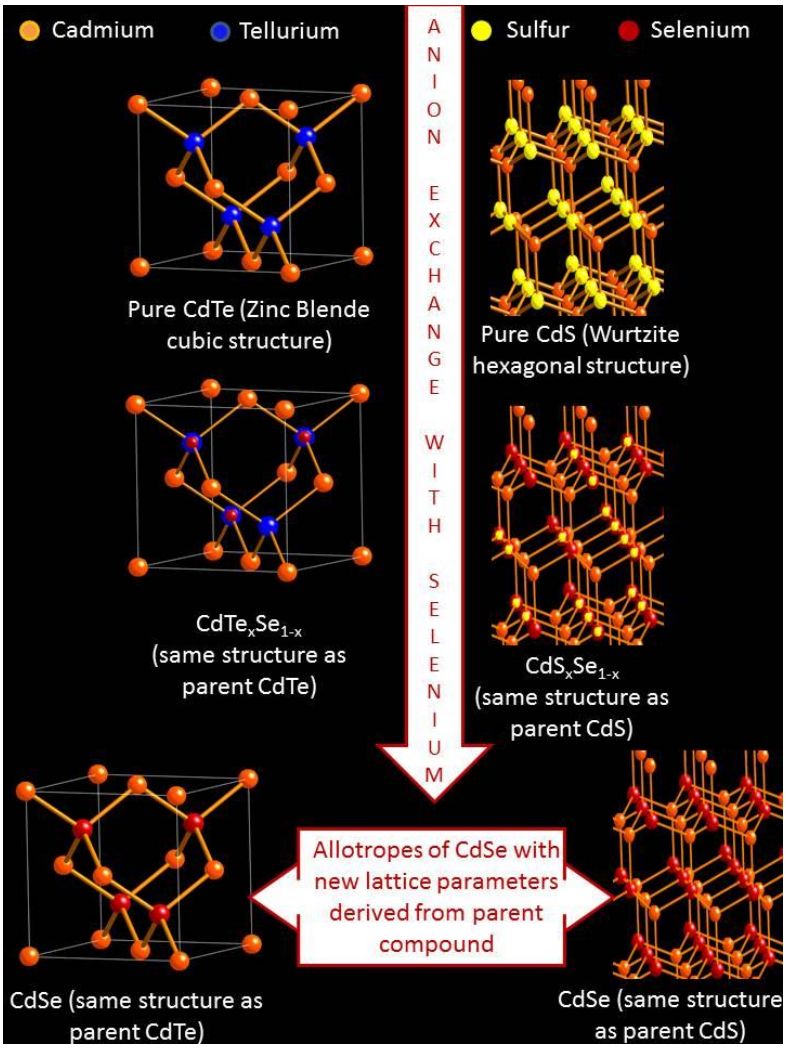

Figure 2.11 Schematic representation of atomic templating where allotropes (WZ and ZB) of a compound (CdSe) can be produced by performing anion exchange in starting compounds with different crystal structures (WZ CdS versus ZB CdTe).

2.9 References

1. Demchenko, D. O.; Robinson, R. D.; Sadtler, B.; Erdonmez, C. K.; Alivisatos, A. P.; Wang, L. W. *Acs Nano* **2008,** 2, (4), 627-636.

2. Il Park, W.; Kim, H. S.; Jang, S. Y.; Park, J.; Bae, S. Y.; Jung, M.; Lee, H.; Kim, J. *J. Mater. Chem.* **2008,** 18, (8), 875-880.

3. Jain, P. K.; Amirav, L.; Aloni, S.; Alivisatos, A. P. *J. Am. Chem. Soc.* **2010,** 132, (29), 9997-9999.

4. Jeong, U.; Xia, Y.; Yin, Y. *Chem. Phys. Lett.* **2005,** 416, (4–6), 246-250.

5. Jeong, U. Y.; Camargo, P. H. C.; Lee, Y. H.; Xia, Y. N. *J. Mater. Chem.* **2006,** 16, (40), 3893-3897.

6. Lee, J. Y.; Kim, D. S.; Park, J. H. *Chem. Mater.* **2007,** 19, (19), 4663-4669.

7. Ma, C.; Ding, Y.; Moore, D.; Wang, X.; Wang, Z. L. *J Am Chem Soc* **2004,** 126, (3), 708-9.

8. Ma, R.; Wang, Y.; Mallouk, T. E. *Small* **2009,** 5, (3), 356-360.

9. Moon, G. D.; Ko, S.; Xia, Y. N.; Jeong, U. *Acs Nano* **2010,** 4, (4), 2307-2319.

10. Piccione, B.; Agarwal, R.; Jung, Y.; Agarwal, R. *Philos Mag (Abingdon)* **2013,** 93, (17), 2089-2121.

11. Robinson, R. D.; Sadtler, B.; Demchenko, D. O.; Erdonmez, C. K.; Wang, L. W.; Alivisatos, A. P. *Science* **2007,** 317, (5836), 355-358.

12. Sadtler, B.; Demchenko, D. O.; Zheng, H.; Hughes, S. M.; Merkle, M. G.; Dahmen, U.; Wang, L. W.; Alivisatos, A. P. *J. Am. Chem. Soc.* **2009,** 131, (14), 5285-5293.

13. Son, D. H.; Hughes, S. M.; Yin, Y. D.; Alivisatos, A. P. *Science* **2004,** 306, (5698), 1009-1012.

14. Zhang, B.; Jung, Y.; Chung, H. S.; Van Vugt, L.; Agarwal, R. *Nano Lett* **2010,** 10, (1), 149-55.

15. Dloczik, L.; Engelhardt, R.; Ernst, K.; Fiechter, S.; Sieber, I.; Konenkamp, R. *Appl. Phys. Lett.* **2001,** 78, (23), 3687-3689.

16. Dloczik, L.; Konenkamp, R. *Nano Lett* **2003,** 3, (5), 651-653.

17. Eliseev, A. A.; Chernysheva, M. V.; Verbitskii, N. I.; Kiseleva, E. A.; Lukashin, A. V.; Tretyakov, Y. D.; Kiselev, N. A.; Zhigalina, O. M.; Zakalyukin, R. M.; Vasiliev, A. L.; Krestinin, A. V.; Hutchison, J. L.; Freitag, B. *Chem. Mater.* **2009,** 21, (21), 5001-5003.

18. Koktysh, D. S.; McBride, J. R.; Dixit, S. K.; Feldman, L. C.; Rosenthal, S. J. *Nanotechnology* **2007,** 18, (49).

19. Shim, H. S.; Shinde, V. R.; Kim, J. W.; Gujar, T. P.; Joo, O. S.; Kim, H. J.; Kim, W. B. *Chem. Mater.* **2009,** 21, (9), 1875-1883.

20. Shinde, V. R.; Gujar, T. P.; Noda, T.; Fujita, D.; Lokhande, C. D.; Joo, O. S. *J Phys Chem C* **2009,** 113, (32), 14179-14183.

21. Xie, Y.; Yan, P.; Lu, J.; Qian, Y. T.; Zhang, S. Y. *Chem. Commun.* **1999**, (19), 1969-1970.

22. Feng, S. H.; Xu, R. R. *Acc. Chem. Res.* **2001,** 34, (3), 239-247.

23. Holt, D. B.; Yacobi, B. G.; Knovel (Firm), Extended defects in semiconductors electronic properties, device effects and structures. In Cambridge University Press,: Cambridge ; New York, 2007; pp xi, 631 p.

24. Agarwal, R.; Lieber, C. M. *Appl. Phys. A* **2006,** 85, (3), 209-215.

25. Hayden, O.; Agarwal, R.; Lieber, C. M. *Nat Mater* **2006,** 5, (5), 352-6.

26. Piccione, B.; Cho, C. H.; van Vugt, L. K.; Agarwal, R. *Nat Nanotechnol* **2012,** 7, (10), 640-5.

27. Piccione, B.; van Vugt, L. K.; Agarwal, R. *Nano Lett* **2010,** 10, (6), 2251-6.

28. van Vugt, L. K.; Piccione, B.; Cho, C. H.; Nukala, P.; Agarwal, R. *Proc Natl Acad Sci U S A* **2011,** 108, (25), 10050-5.

29. Lange, H.; Artemyev, M.; Woggon, U.; Thomsen, C. *Physica Status Solidi B-Basic Solid State Physics* **2009,** 246, (11-12), 2817-2819.

30. Tell, B.; Damen, T. C.; Porto, S. P. S. *Phys Rev* **1966,** 144, (2), 771-&.

31. Lu, L.; Xu, X. L.; Liang, W. T.; Lu, H. F. *J Phys-Condens Mat* **2007,** 19, (40).

32. Venugopal, R.; Lin, P. I.; Liu, C. C.; Chen, Y. T. *J. Am. Chem. Soc.* **2005,** 127, (32), 11262-11268.

33. Lawaetz, P. *Phys Rev B* **1972,** 5, (10), 4039.

34. Yeh, C. Y.; Lu, Z. W.; Froyen, S.; Zunger, A. *Phys Rev B* **1992,** 46, (16), 10086-10097.

35. Kulakov, M. P.; Balyakina, I. V. *J. Cryst. Growth* **1991,** 113, (3–4), 653-658.

36. Shan, C. X.; Liu, Z.; Hark, S. K. *Appl. Phys. Lett.* **2005,** 87, (16), 163108.

37. Liu, L. P.; Zhuang, Z. B.; Xie, T.; Wang, Y. G.; Li, J.; Peng, Q.; Li, Y. D. *J. Am. Chem. Soc.* **2009,** 131, (45), 16423-16429.

38. Mohamed, M. B.; Tonti, D.; Al-Salman, A.; Chemseddine, A.; Chergui, M. *J. Phys. Chem. B* **2005,** 109, (21), 10533-10537.

39. Capek, R. K.; Moreels, I.; Lambert, K.; De Muynck, D.; Zhao, Q.; Vantomme, A.; Vanhaecke, F.; Hens, Z. *J Phys Chem C* **2010,** 114, (14), 6371-6376.

40. Deng, Z. T.; Cao, L.; Tang, F. Q.; Zou, B. S. *J. Phys. Chem. B* **2005,** 109, (35), 16671-16675.

41. Zelaya-Angel, O.; Lozada-Morales, R. *Phys Rev B* **2000,** 62, (19), 13064-13069.

42. Vogel, W.; Urban, J.; Kundu, M.; Kulkarni, S. K. *Langmuir* **1997,** 13, (4), 827-832.

43. Jun, Y. W.; Lee, S. M.; Kang, N. J.; Cheon, J. *J. Am. Chem. Soc.* **2001,** 123, (21), 5150-5151.

44. Cao, Y. C.; Wang, J. H. *J. Am. Chem. Soc.* **2004,** 126, (44), 14336-14337.

45. Agarwal, R.; Zakharov, D. N.; Krook, N. M.; Liu, W.; Berger, J. S.; Stach, E. A. *Nano Lett.* **2015,** 15, (5), 3303-8.

46. Li, Q.; Gong, X. G.; Wang, C. R.; Wang, J.; Ip, K.; Hark, S. *Adv. Mater.* **2004,** 16, (16), 1436-+.

47. Islam, S. S.; Rath, S.; Jain, K. P.; Abbi, S. C.; Julien, C.; Balkanski, M. *Phys Rev B* **1992,** 46, (8), 4982-4985.

48. Lee, J. S.; Giles, N. C.; Rajavel, D.; Summers, C. J. *Phys Rev B* **1994,** 49, (3), 1668-1676.

49. Liu, M. C.; Wang, L. Z.; Lu, G. Q.; Yao, X. D.; Guo, L. J. *Energy Environ. Sci.* **2011,** 4, (4), 1372-1378.

50. Medlin, D. L.; Snyder, G. J. *Curr Opin Colloid In* **2009,** 14, (4), 226-235.

51. Porter, D. A.; Easterling, K. E.; Sherif, M. Y., *Phase transformations in metals and alloys*. 3rd ed.; CRC Press: Boca Raton, FL, 2009; p xix, 500 p.

52. Cox, J. D.; Wagman, D. D.; Medvedev, V. A., CODATA key values for thermodynamics. Hemisphere Pub. Corp.: New York, 1989; p xiii, 271 p.

CHAPTER 3: Cation Exchange in II-VI Semiconducting Nanostructures

Adapted and reprinted in parts from:

R. Agarwal, Y. Kim, S. Liu, L.Z. Tan, W. Liu, A. M. Rappe and R. Agarwal, "Atomic Templating Based Chemical Transformation in II-VI Semiconducting Nanostructures" Under preparation for submission.

3.1 Introduction

Chalcogenide compounds, in bulk and especially at the nanoscale, find diverse applications in a variety of fields owing to their unique physical properties and bonding characteristics[1-12]. Therefore, there exists a tremendous scope of exploring unique chalcogenide based chemical compositions in different crystal structures which may further enhance their unique physical properties. Chemical transformation in nanostructures is a promising route of creating such novel systems which are challenging to synthesize otherwise[13-28]. In chapter 2, we discussed lattice framework and defect distribution preserving anion exchange reaction in II-VI semiconductors via atomic templating which enabled synthesis of metastable phases of well-known compounds such as zincblende (ZB) CdS and CdSe (Chapter 2). In this chapter, we extend the concept of atomic templating by exchanging the cationic species in II-VI semiconducting nanomaterials with elements from dissimilar groups such as IV A and V A of the periodic table that possess different bonding characteristics as compared to elements of group II B. ZB CdTe and wurtzite (WZ) CdSe, compounds with different crystal structures, were chosen as the starting material owing to the ease with which Cd^{2+} cationic species can be replaced[13,28]. As a function of reaction temperature, we observe varied degrees of cation

exchange leading to formation of unique chemical and crystallographic heterostructures and completely transformed products. The structural and chemical transformation mechanism has been explained through observations via TEM based characterization techniques. The physical properties and relative chemical stability of the intermediate and final products of cation exchange reactions are obtained by first-principles calculations performed with density functional theory (DFT) and are utilized to predict possible applications of these unique materials.

3.2 Cation Exchange in Zincblende CdTe with Pb

To gauge the reactivity of II-VI compounds with elements from dissimilar groups of the periodic table, ZB CdTe nanostructures, a cubic close-packed compound, were exposed to Pb (group IV A) vapor in a chemical vapor deposition (CVD) set-up at elevated temperatures. Cd and Te atoms are present in tetrahedral coordination with ionic nature of bonding in ZB CdTe whereas Pb and Te atoms usually exist in octahedral coordination with covalent nature of bonding in the Pb-Te compounds. Therefore, reaction between CdTe and Pb could theoretically yield products ranging from layered $PbTe_2$ to rocksalt (RS) PbTe. At 475 ^{o}C, the reaction between ZB CdTe nanostructures and Pb resulted in a CdTe-PbTe heterostructure while the selected area electron diffraction (SAED) pattern indicated single-crystalline cubic close-packed crystal structure (Figure 3.1 A-B). On increasing the reaction temperature to 500 ^{o}C, ZB CdTe nanostructures completely transformed into single crystalline cubic close-packed PbTe (Figure 3.1 C-D). To inspect whether the transformed product, a cubic close-packed structure, was present in ZB or RS configuration, optical second harmonic generation

(SHG) technique was utilized[29] (see Appendix A). ZB compounds, which are non-centrosymmetric, produce SHG signal whereas RS compounds which possess a crystallographic inversion center, do not produce SHG signal. PbTe nanostructures obtained via chemical transformation failed to produce SHG signal and therefore it was confirmed that the compound was present in RS configuration.

The observed chemical transformation can be understood as follows. At lower temperatures, only partial cation exchange is accomplished owing to slower reaction kinetics and sluggish diffusion leading to formation of chemical heterostructures where as complete cation exchange is accomplished at higher temperatures[28]. It is important to note that CdTe-PbTe heterostructures are formed along the <111> direction since the lowest interfacial energy between the two phases exist along the close packed {111} planes[30]. Since both ZB and RS crystal structure have identical anionic framework (close-packed layers in ABCABC… stacking as seen in Figure 3.1 E and 3.1 G), there is no driving force for anions to be displaced during cation exchange. Therefore, chemical transformation from ZB CdTe to RS PbTe only involves replacement of Cd atoms in tetrahedral coordination with Pb atoms in octahedral coordination while Te atoms remain stationary. Another proof of the anionic framework preserving nature of this cation exchange reaction is the retention of planar defects from ZB CdTe, namely {111} twin boundaries (TBs), into resulting PbTe nanostructures (Figure 3.1 A and 3.1 C). Besides providing crucial information about the structural transformation mechanism, TBs in PbTe offer interesting physical properties for thermoelectric application. PbTe is a small band-gap semiconductor with relatively low thermal conductivity and is therefore a good

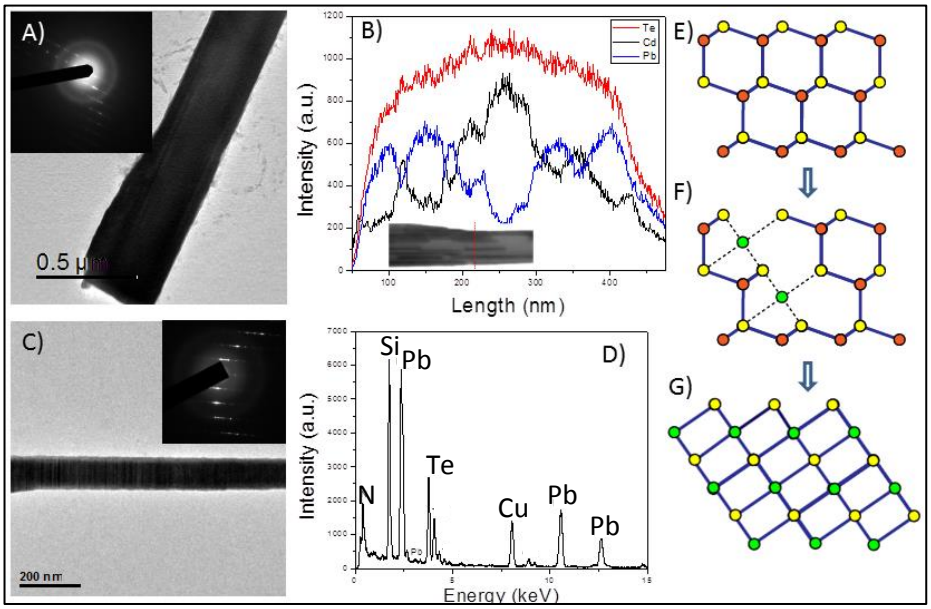

Figure 3.1 Characterization of nanostructures after undergoing partial and complete chemical transformation from ZB CdTe to RS PbTe. A) Bright field TEM micrograph of a ZB CdTe-RS PbTe heterostructure obtained from partial chemical transformation of ZB CdTe NB by introducing Pb at 475 ^{0}C. Inset: SAED pattern indicating single crystalline close-packed cubic structure (ZB/RS) while retaining TBs from parent ZB CdTe in the CdTe-PbTe heterostructure. B) EDS line scan across the NB shown in A (along the red dotted line in inset) confirming presence of CdTe-PbTe heterostructure. C) Bright field TEM micrograph of a RS PbTe NW obtained from complete chemical transformation of ZB CdTe NW by introducing Pb at 500 ^{0}C. Inset: SAED pattern indicating single crystalline close-packed cubic structure (ZB/RS) while retaining periodic TBs from parent ZB CdTe. D) EDS point scan of the NW shown in C confirming complete chemical transformation from CdTe into PbTe. E) Atomic model of ZB CdTe viewed along <110>. Orange atoms correspond to Cd whereas yellow atoms correspond to Te. Both Cd and Te are present in tetrahedral coordination. F) Reaction of ZB CdTe with Pb leading to replacement of Cd in tetrahedral coordination (orange atoms) with Pb in octahedral coordination (green atoms) while Te remains stationary (yellow atoms). G) Further introduction of Pb leads to complete chemical transformation of ZB CdTe into RS PbTe.

candidate as a thermoelectric material[12]. Planar defects such as TBs act as efficient phonon scattering centers which further reduce thermal conductivity of the material[31]. Besides, first-principles calculations using DFT predict that PbTe in the TB region is metallic (Figure 3.2) and therefore can provide channels with high electrical conductivity thereby increasing the electrical conductivity of the entire material. Therefore, PbTe

nanostructures with TBs, as obtained in our experiments, can prove to be highly efficient thermoelectric materials with higher figure of merit than ordinary PbTe nanostructures.

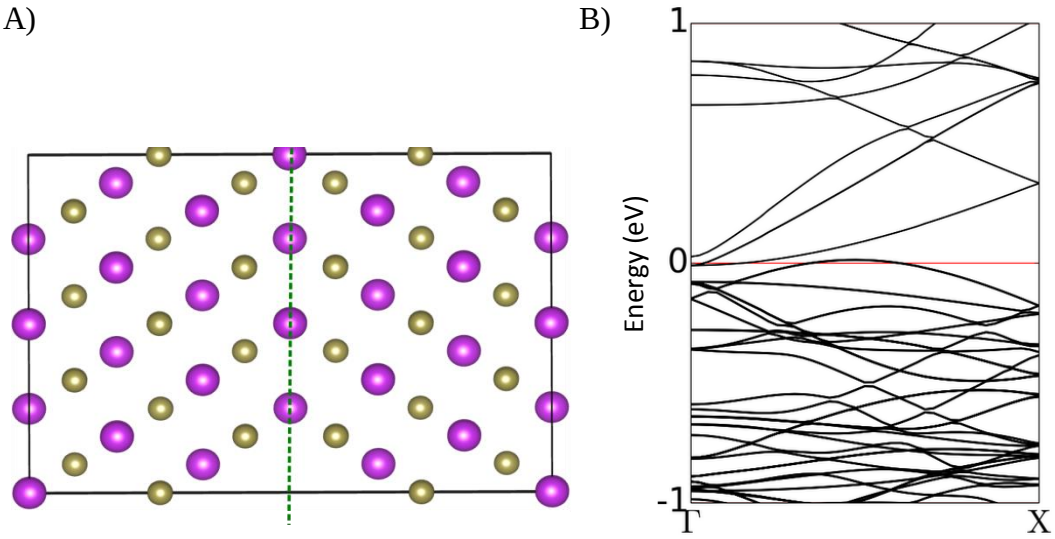

Figure 3.2 Crystal and band structure of PbTe near twin boundary. A) Rocksalt PbTe with {111} twin boundary depicted by green dashed line. B) Band structure of rocksalt PbTe in the vicinity of the twin boundary. Fermi level (zero energy red line) intersects with the valence and the conduction band at different points in k-space thereby giving the material a metallic character.

3.3 Cation Exchange in Zincblende CdTe with Bi

To further explore the reactivity of II-VI compounds with elements from other groups in the periodic table besides II B[28] and IV A, ZB CdTe nanostructures were exposed to Bi (group V A) vapor in a chemical vapor deposition (CVD) set-up at elevated temperatures. Upon reacting ZB CdTe nanostructures with Bi at 525 °C, complete chemical transformation into BiTe was achieved while retaining the single crystallinity, close-packed crystal structure and defect distribution of the parent CdTe (Figure 3.3). Since the resulting products did not produce optical SHG signal, the crystal structure was determined to be RS instead of ZB and therefore it was concluded that the transformed products were RS BiTe, a metastable compound that has been rarely studied in the past[32].

The most common compound of bismuth and tellurium is the layered compound Bi_2Te_3 where Bi and Te atoms exist in octahedral coordination and the nature of bonding is predominantly covalent. However, unlike ZB and RS configuration, Te atoms in Bi_2Te_3 follow ABC x BCA x CAB stacking (where 'x' denotes van der Waal's layer) and

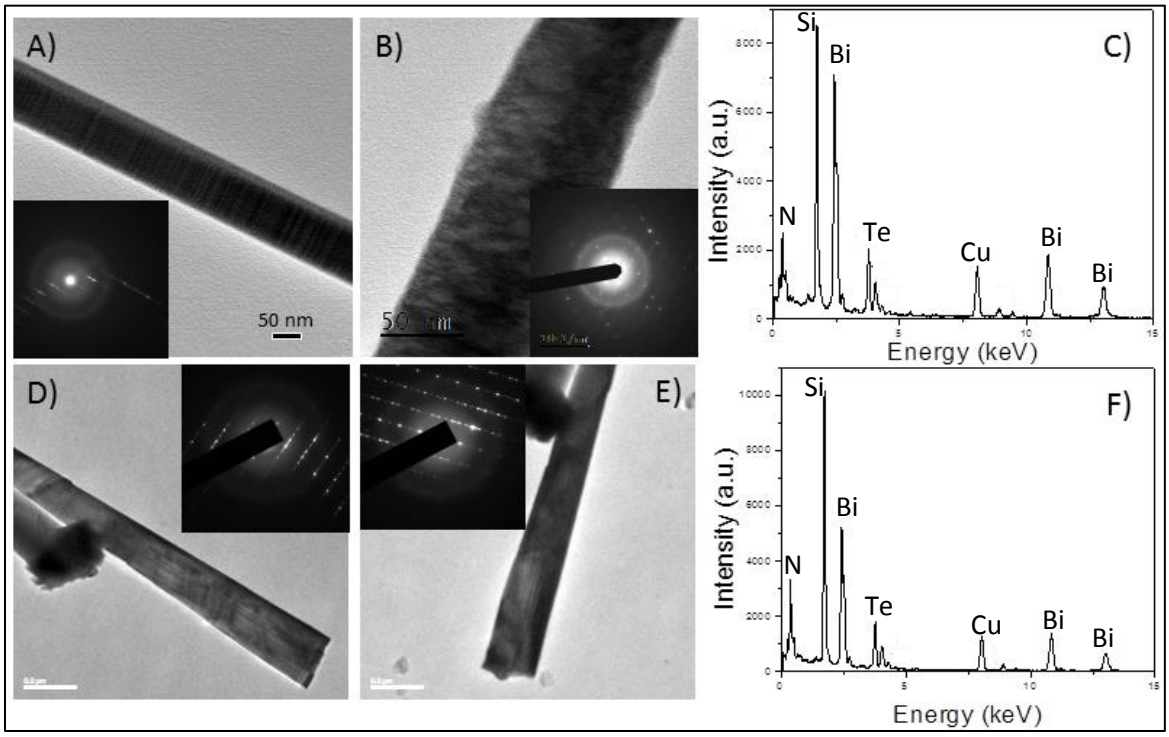

Figure 3.3 Characterization of nanostructures after undergoing complete chemical transformation from ZB CdTe to RS BiTe. A) Bright field TEM micrograph of an as-grown ZB CdTe NW with periodic {111} TBs along the growth direction <111>. Inset: SAED pattern confirming presence of twin boundaries in ZB CdTe NW. B) Bright field TEM micrograph of RS BiTe NW obtained from complete chemical transformation of ZB CdTe NW shown in A by introducing Bi at 525 °C. Inset: SAED pattern indicating single crystalline close-packed cubic structure (ZB/RS) while retaining periodic TBs from parent ZB CdTe NW. C) EDS point scan of the NW shown in B confirming complete chemical transformation from CdTe into BiTe. D) Bright field TEM micrograph of an as-grown ZB CdTe NB with {111} TBs perpendicular to the growth direction <112>. Inset: SAED pattern confirming presence of twin boundaries in ZB CdTe NB. E) Bright field TEM micrograph of RS BiTe NB obtained from complete chemical transformation of ZB CdTe NB shown in D by introducing Bi at 525 °C. Inset: SAED pattern indicating single crystalline close-packed cubic structure (ZB/RS) while retaining periodic TBs from parent ZB CdTe NB. F) EDS point scan of the NB shown in E confirming complete chemical transformation from CdTe into BiTe.

therefore transformation of CdTe into Bi_2Te_3 would require large scale atomic motion of the anions. Even though theoretical calculations using DFT indicate greater chemical stability of Bi_2Te_3 as compared to RS BiTe, the reaction favors the compound which requires least atomic rearrangement and can easily accommodate the heavy influx of Bi atoms. We have calculated the cohesive energy of BiTe in a RS geometry and Bi_2Te_3 in a rhombohedral structure, defined by $\Delta E_c = (E_{AnBm} - n\,E_A - m\,E_B)/(n+m)$. The cohesive energies of BiTe and Bi_2Te_3 are -2.54 eV and -4.17 eV at room temperature and pressure, suggesting BiTe in a RS phase is meta-stable. The concept of atomic templating was once again utilized to obtain a metastable nanostructure by

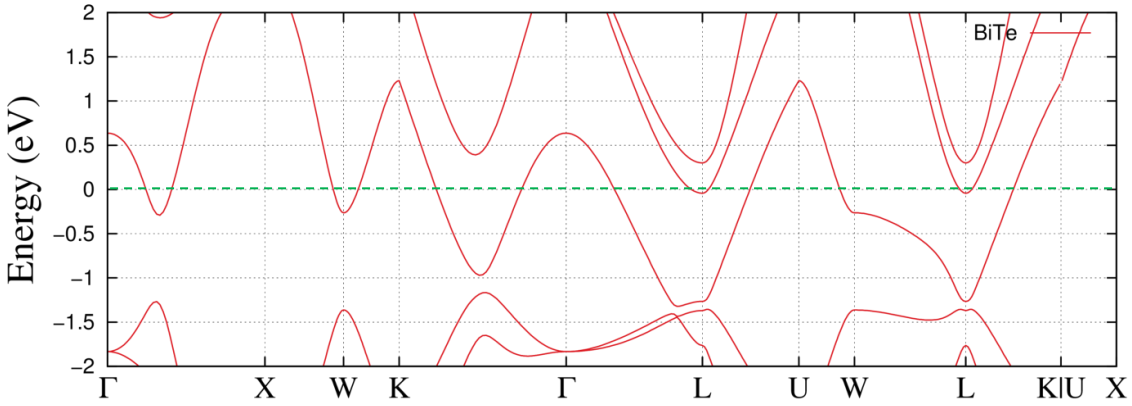

Figure 3.4 Band structure of BiTe in a RS geometry. The Fermi energy is set to zero (green dashed line).

kinetically freezing the motion of anionic lattice framework while replacing the cationic species thereby resulting in a compound which is very challenging to obtain otherwise[32]. First-principles calculations predict that RS BiTe will be an n-type degenerately doped metal with the fermi level present in the conduction band (Figure 3.4). However, presence of TBs, which were retained from parent CdTe, might make this material interesting for a number of applications ranging from thermoelectrics to phase change memory materials[8,31].

3.3 Cation Exchange in Wurtzite CdSe with Pb

Thus far, ZB CdTe was chosen as the starting compound which exists in cubic close-packed structure and therefore could be easily transformed into RS crystal structure upon chemical transformation. However, it would be interesting to observe how a hexagonal close-packed II-VI semiconductor such as WZ CdSe will chemically and structurally transform under similar reaction conditions. Therefore, WZ CdSe nanostructures were reacted with Pb vapor in a chemical vapor deposition (CVD) set-up over a range of temperatures and the products were analyzed for chemical composition and structure via TEM based techniques. Similar to ZB CdTe, Cd and Se atoms in WZ CdSe are present in tetrahedral coordination with ionic bonding whereas Pb and Se are present in octahedral coordination with covalent bonding in the only known line compound, RS PbSe. At 450 °C, reaction between WZ CdSe nanowire (NW) and Pb vapor resulted in a $Cd_xPb_{1-x}Se$ alloy and the SAED pattern indicated a mixture of hexagonal WZ and cubic close packed phases such that the close packed plane of both crystal structures remained parallel (Figure 3.5 A-B). Presence of cubic close packed phase indicated the initiation of RS PbSe formation. Upon reacting the same alloyed NW at 475 °C with Pb vapor, it was completely transformed into a PbSe compound with no residual Cd, but structurally, the NW consisted of alternating domains of hexagonal and cubic close packed phases while maintaining the parallel close packed planes of the two crystal structures (Figure 3.5 C-E). On further increasing the reaction temperature to 500 °C, the NW remained chemically stable but structurally transformed into a uniform cubic close packed phase similar to RS PbSe. Even though the final product of chemical

transformation is the expected RS PbSe phase, the intermediate hexagonal PbSe compound is intriguing and deserves greater attention. Also, it is important to note that

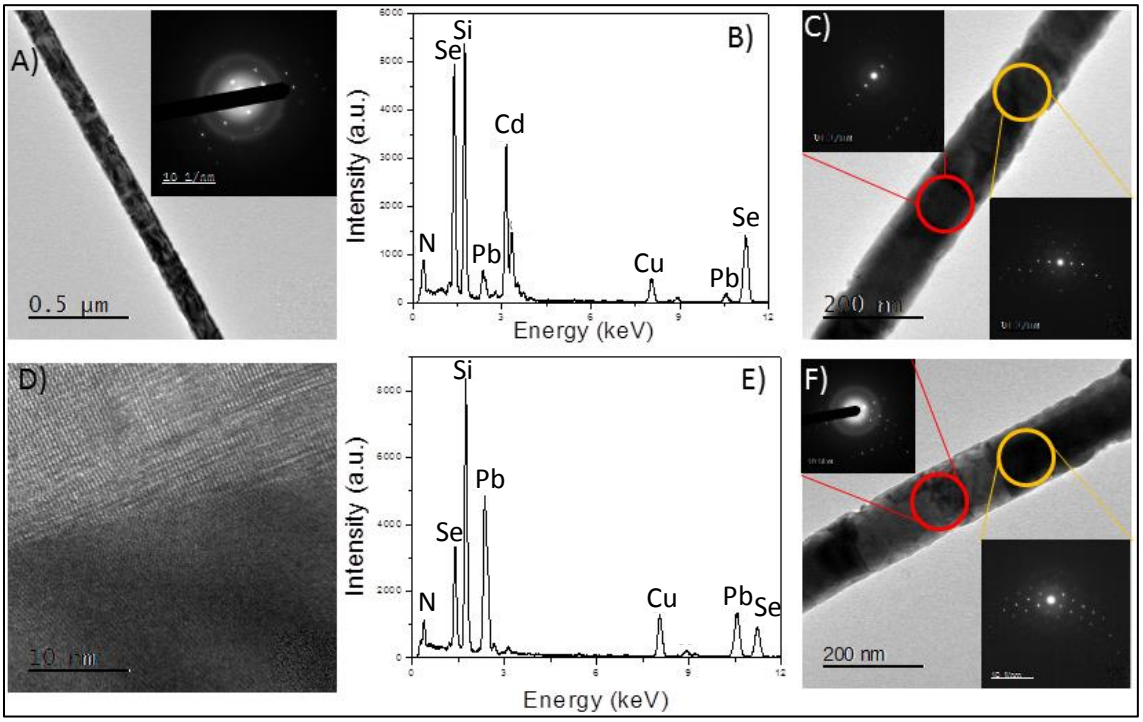

Figure 3.5 Characterization of a single NW at different stages of chemical transformation from WZ CdSe to RS PbSe via hex-PbSe phase. A) Bright field TEM micrograph of a $Cd_xPb_{1-x}Se$ NW obtained by reacting WZ CdSe NW with Pb at 450 ^{0}C. Inset: SAED pattern indicating superimposed WZ and cubic close-packed crystal structure such that the closed packed planes are parallel to each other in both structures. B) EDS point scan of the NW shown in A indicating incorporation of Pb in CdSe NB. C) Bright field TEM micrograph of RS PbSe- hex-PbSe heterostructure obtained by reacting the NW shown in A with Pb at 475 ^{0}C. Upper left inset: SAED pattern of the lighter contrast NW region (red circle) indicating hexagonal crystal structure (hex-PbSe). Bottom right inset: SAED pattern of the darker contrast NW region (orange circle) indicating cubic closed packed crystal structure (PbSe). D) HRTEM micrograph of NW shown in C at the domain boundary confirming the lighter region corresponds to hexagonal structure where as darker region corresponds to cubic closed packed structure. E) EDS point scan of the NW shown in C confirming complete chemical transformation into PbSe with no residual Cd. F) Bright field TEM micrograph of RS PbSe NW obtained by reacting the NW shown in C with Pb at 500 ^{0}C. SAED pattern of the lighter contrast NW region (red circle) in the upper left inset and bottom right inset SAED pattern of the darker contrast NW region (orange circle) in the bottom right inset both indicating cubic closed packed crystal structure (PbSe).

RS PbSe has a different anionic stacking sequence (ABCABCABC…) as compared to the starting WZ CdSe (ABABAB…) and therefore it becomes important to understand this transformation mechanism which requires in-plane atomic rearrangement over several layers. Besides, RS PbSe-hexagonal PbSe heterostructures at the nanoscale may resist heat flow better than pure RS PbSe nanostructures owing to enhanced phonon scattering from the interface between the two phases. Also, DFT calculations suggest that hexagonal PbSe will behave as a metal (Figure 3.6) thereby enhancing the electrical conductivity of the heterostructure making it a very good candidate for thermoelectric applications.

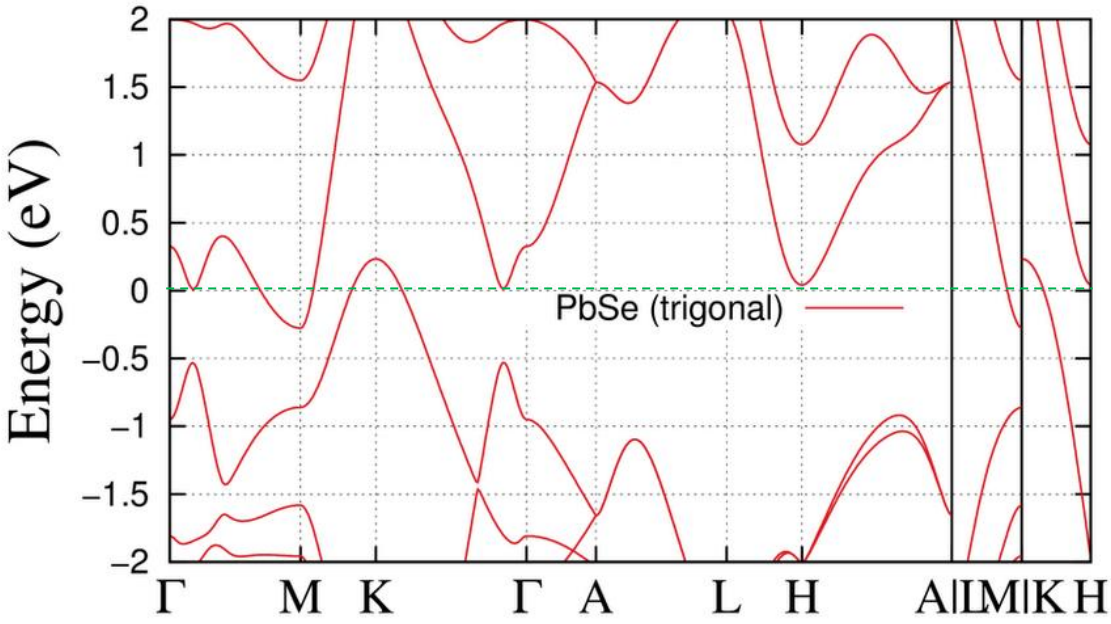

Figure 3.6 Band structure of PbSe in hexagonal geometry. The Fermi energy is set to zero (green dashed line).

To understand the transformation pathway between WZ CdSe and RS PbSe via the unique intermediate hexagonal PbSe phase, a large WZ CdSe nanobelt (NB) was chosen for the reaction with Pb. At 450 °C, the NB transformed into $Cd_xPb_{1-x}Se$ alloy and

the SAED pattern indicated a mixture of hexagonal WZ and cubic close packed phases such that the close packed plane of both crystal structures remained parallel (Figure 3.7 A-B) similar to Figure 3.5 A-B. On increasing the reaction temperature to 475 °C, the

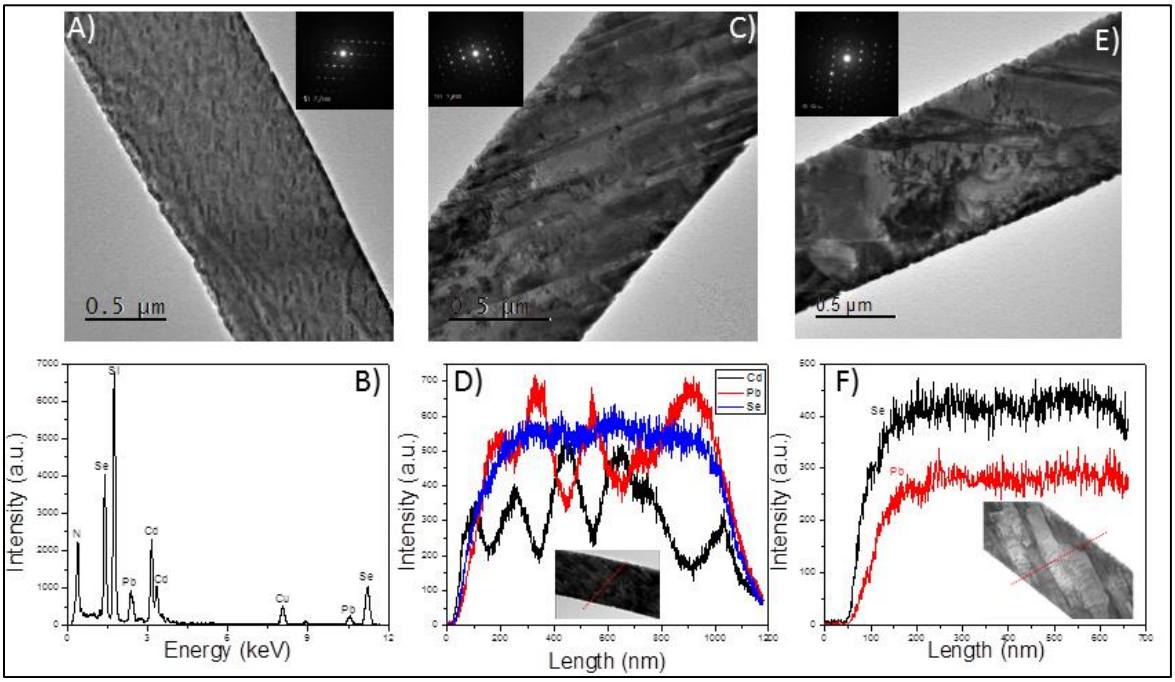

Figure 3.7 Characterization of a single NB at different stages of chemical transformation from WZ CdSe to RS PbSe via hexagonal PbSe phase. A) Bright field TEM micrograph of a $Cd_xPb_{1-x}Se$ NB obtained by reacting WZ CdSe NB with Pb at 450 ^{0}C. Inset: SAED pattern indicating superimposed WZ and cubic close-packed crystal structure such that the closed packed planes of both are parallel. B) EDS point scan of the NW shown in A indicating incorporation of Pb in CdSe NW. C) Bright field TEM micrograph of WZ CdSe-PbSe heterostructure obtained by reacting the NB shown in A with Pb at 475 ^{0}C. Inset: SAED pattern of the NB indicating superimposed WZ and cubic close-packed crystal structure such that the closed packed planes of both are parallel. D) EDS line scan across the NB shown in C (along the red dotted line in the inset) confirming the presence of CdSe-PbSe heterostructure. E) Bright field TEM micrograph of PbSe NB obtained by reacting the NB shown in C with Pb at 500 ^{0}C. Inset: SAED pattern of the NB indicating superimposed WZ and cubic close-packed crystal structure such that the closed packed planes of both are parallel. F) EDS line scan across the NB shown in E (along the red dotted line in the inset) confirming complete transformation into PbSe with no residual Cd.

same alloyed NB transformed into a chemical heterostructure with alternating domains of Cd rich and Pb rich selenide while the crystal structure remained similar as before in both domains (Figure 3.7 C-D). On further increasing the reaction temperature to 500 °C, the alloyed NB completely chemically transformed into spatially homogenous PbSe compound while the crystal structure remained same as before (Figure 3.7 E-F). Any further increase in reaction temperature led to sublimation of the NB and no structural or chemical transformation was observed. This inability of large nanostructures to fully transform from WZ to RS crystal structure revealed important information regarding the transformation mechanism while establishing the capability of chemical transformation in nanostructures to obtain unique phases of materials such as CdSe-PbSe heterostructure.

3.4 Mechanism of Rocksalt PbSe Formation from Wurtzite CdSe

The hypothesis explaining the observed transformation between WZ CdSe and RS PbSe via the intermediate hexagonal PbSe phase is as follows. Upon reacting WZ CdSe with Pb at elevated temperatures, Pb atoms will displace Cd atoms from their tetrahedral position (Figure 3.8 A) while themselves occupying the preferred octahedral position (Figure 3.8 B). Se atoms which are bonded to both Pb and Cd atoms will be highly strained owing to different coordination numbers of the two elements and therefore it will be energetically favorable for the Pb rich and the Cd rich domains to segregate until all Cd is replaced by Pb. Complete replacement of Cd by Pb will lead to formation of a hexagonal allotrope of RS PbSe (Figure 3.8 C) which can be visualized as RS PbSe with every Se layer acting as a TB (red dotted line in Figure 3.8 C). In the hexagonal PbSe phase, Se close packed layers continue to exist in WZ like ABABAB stacking, whereas

Pb close packed layers occupy C position throughout thereby creating an identical diffraction pattern as WZ CdSe. Formation of hexagonal PbSe with alternating TBs highlights the role of atomic templating of the anionic species in dictating the crystal structure of chemically transformed products. However, based on DFT calculations

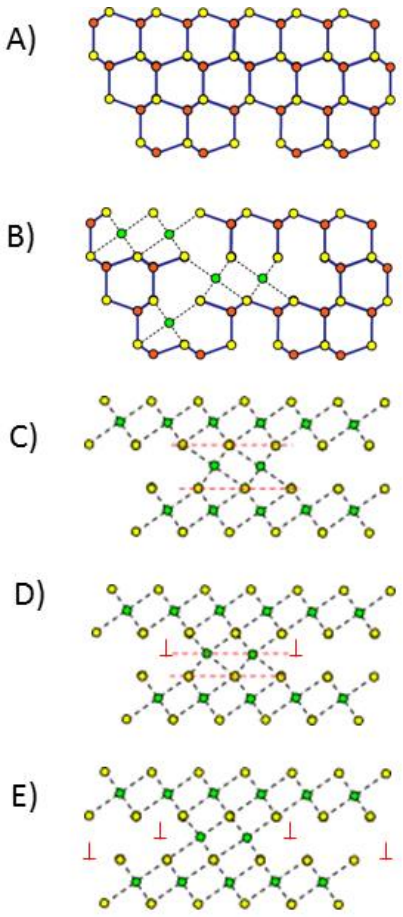

Figure 3.8 Schematic illustrating the transformation mechanism of WZ CdSe into RS PbSe via hexagonal $PbSe_2$. A) Atomic model of WZ CdSe viewed along *a-axis*. Orange atoms correspond to Cd whereas yellow atoms correspond to Se. Both Cd and Se are present in tetrahedral coordination. B) Reaction of WZ CdSe with Pb leading to replacement of Cd in tetrahedral coordination (orange atoms) with Pb in octahedral coordination (green atoms) while Te remains stationary (yellow atoms). Incomplete replacement of Cd with Pb leads to formation of CdSe-PbSe heterostructure. C) Further introduction of Pb leads to complete chemical transformation of WZ CdSe into hex-PbSe (RS PbSe with {111} twin boundaries). D) Further introduction of Pb leading to growth of Pb rich domains finally causing twin boundaries to heal through creation and migration of partial dislocations. E) The entire system converting to RS PbSe upon further dislocation motion thereby relaxing all the twin boundaries in the system.

which predict that hexagonal PbSe is metastable as compared to RS PbSe, the hexagonal PbSe phase will eventually transform into RS PbSe. We have calculated the cohesive energy of PbSe in a hexagonal geometry and RS PbSe, defined by $\Delta E_c = (E_{AnBm} - n\,E_A - m\,E_B)/(n+m)$. The cohesive energies of hexagonal PbSe and RS PbSe are -3.0777 eV and -3.1913 eV, respectively at the reaction temperature (500 °C), suggesting PbSe in a hexagonal phase is meta-stable. This transformation, which will involve change in stacking sequence of Se and Pb close packed layers from hexagonal close packed to cubic close packed configuration, will most likely proceed through motion and separation of Shockley partial dislocations with Burgers vector $\vec{b} = \frac{a}{6} < 11\bar{2} >$ [33-35] (Figure 3.8 D). Change in stacking sequence of one atomic layer will directly influence the nearest neighbor layer thereby catalyzing its transformation leading to an overall change from hexagonal to cubic close packed system (Figure 3.8 E). In smaller nanostructures such as NWs (Figure 3.5), especially when the close packed layers are < 100 nm, partial dislocations can be created, separated and annihilated at the surface thereby changing the atomic stacking sequence with relative ease. However, this process is much more challenging in larger nanostructures such as NBs where the close packed layers are much larger in size (> 1 μm) and partial dislocations are incapable of changing the stacking sequence of the entire close packed layer since it would involve two partial dislocations separated from each other over large distances (Figure 3.7). From bright field TEM micrographs (Figure 3.7 A,C and E) and dark field TEM micrographs (Figure 3.9), line contrasts (corresponding to stacking fault contrasts), which originate and terminate inside the NB, along the closed packed planes can be observed which support the partial

dislocation mediated stacking sequence transformation mechanism. This transformation mechanism explains our observations while highlighting the role of atomic templating in directing the chemical and structural transformation in nanostructures and dictating the final transformed product which may be controlled by varying the experimental parameters such as size of the parent material and reaction temperature. The above discussed transformation mechanism is similar to the observed transformation in II-VI compounds from WZ to RS phase upon application of pressure, a mechanical stimulus that leads to atomic rearrangement[36-37]. However, in our case, we are able to achieve such a transformation through a chemical and thermal stimulus where atomic substitution is the driving force for the observed phase transformation.

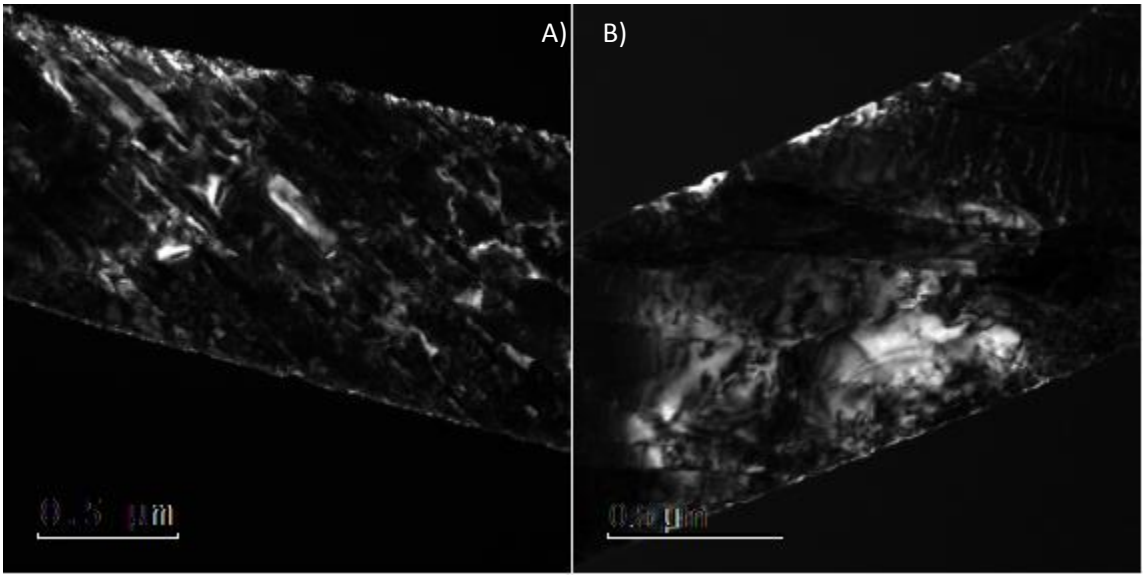

Figure 3.9 A) DFTEM micrograph of CdSe-PbSe heterostructure NB (corresponding to Figure 3.7 C) obtained by selecting (1100) diffraction spot of the hexagonal structure. Line contrasts correspond to domain boundaries between Cd rich and Pb rich selenide regions and stacking faults separating hexagonal and rocksalt PbSe phase. B) DFTEM micrograph of PbSe NB (corresponding to Figure 3.7 E) obtained by selecting (1100) diffraction spot of the hexagonal phase. Line contrasts correspond to stacking faults separating hexagonal and rocksalt PbSe phase.

3.5 Stacking Faults in CdS Nanobelts upon In-Situ TEM Heating

To inspect the Shockley partial dislocation dynamics in a WZ II-VI semiconducting nanostructure, we heated a WZ CdS NB inside TEM to 500 °C (to mimic the temperature of the reaction conditions) and observed the structural transformation in real-time. Along with sublimation at the NB edges, Figure 3.10 (snapshots from a movie) indicates line contrasts originating and moving perpendicular to *c*-axis (along the close packed plane) leaving behind a trail which we interpret as a stacking fault. The forward moving tip of this line contrast is the leading partial dislocation where as the other tip, trying to catch up with the forward tip, is the trailing partial dislocation. These dislocations are observed to originate inside the NB and glide towards the surface (Figure 3.10 C) where they leave behind a step. The line contrast left behind is then cleaned up by the trailing dislocation following the leading dislocation towards the surface. The stacking fault is nothing but a monolayer of WZ material transformed into ZB structure thereby changing the atomic stacking from A B A B A B type to A B C A B C type which is also the stacking sequence for RS crystal structure. This experiment establishes the possibility of partial dislocation mediated transformation from hexagonal to RS phase observed in our chemical transformation experiments between WZ CdSe and RS PbSe. Also, it can be clearly seen that for the stacking fault to remain stable, which can be interpreted in our experiment as the stability of the RS phase, partial dislocations have to be separated from each other and desirably, annihilated at opposite facets such that there is no possibility of stacking fault healing.

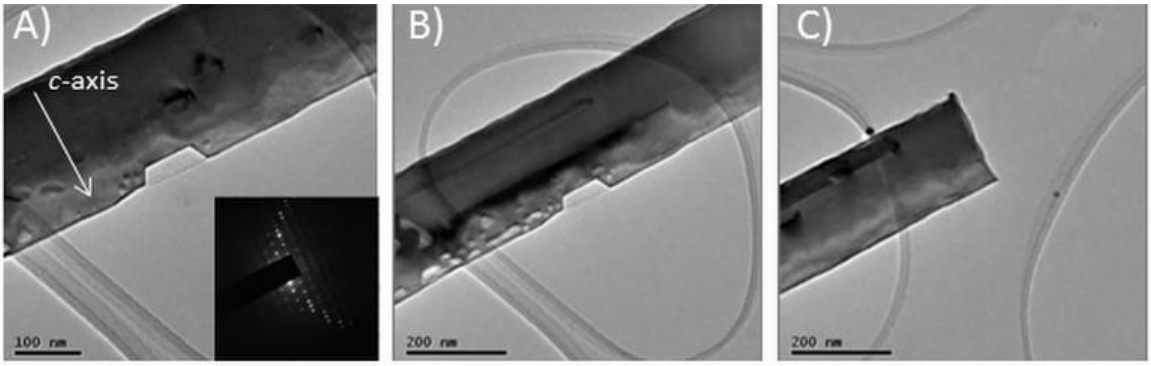

Figure 3.10 A) CdS NB with long axis perpendicular to *c*-axis showing sublimation at the edges and beginning of formation of line contrasts towards the center of the material. Inset: SAED pattern of the NB confirming the WZ crystal structure and growth orientation. B) Elongation of line contrasts by separation between leading and trailing partial dislocations. C) Partial dislocations migrating along the close packed plane towards the surface and eventually annihilating there leaving behind a step.

3.6 Conclusion

In conclusion, we have demonstrated the ability of controlled chemical transformations, by using II-VI semiconducting nanostructures as a model system, in engineering novel phases of materials ranging from pure compounds to chemical and crystallographic heterostructures with the capacity to control the defect distribution. More importantly, the underlying mechanism of such transformations have been explained which opens up newer avenues for nanostructure engineering. Also, the ability to substitute elements from dissimilar groups of the periodic table increases our capacity to engineer materials with desired composition and crystal structure for targeted applications.

3.7 References

1. Holt, D. B.; Yacobi, B. G.; Knovel (Firm), Extended defects in semiconductors electronic properties, device effects and structures. Cambridge University Press,: Cambridge ; New York, 2007; pp xi.

2. Xia, Y. N.; Yang, P. D.; Sun, Y. G.; Wu, Y. Y.; Mayers, B.; Gates, B.; Yin, Y. D.; Kim, F.; Yan, Y. Q. Adv. Mater. 2003, 15, (5), 353.

3. Agarwal, R.; Lieber, C. M. Appl. Phys. A 2006, 85, (3), 209.

4. Thelander, C et al. Mater. Today 2006, 9, (10), 28.

5. Lieber, C. M. MRS Bull. 2003, 28, (7), 486.

6. Piccione, B.; van Vugt, L. K.; Agarwal, R. Nano Lett 2010, 10, (6), 2251.

7. Agarwal, R.; Zakharov, D. N.; Krook, N. M.; Liu, W.; Berger, J. S.; Stach, E. A. Nano Lett. 2015, 15, (5), 3303.

8. Nukala, P.; Agarwal, R.; Qian, X. F.; Jang, M. H.; Dhara, S.; Kumar, K.; Johnson, A. T. C.; Li, J.; Agarwal, R. Nano Lett. 2014, 14, (4), 2201.

9. Piccione, B.; Agarwal, R.; Jung, Y.; Agarwal, R. Philos Mag (Abingdon) 2013, 93, (17), 2089.

10. van Vugt, L. K.; Piccione, B.; Cho, C. H.; Nukala, P.; Agarwal, R. Proc Natl Acad Sci U S A 2011, 108, (25), 10050.

11. Jung, Y.; Agarwal, R.; Yang, C. Y. Nanotechnology 2011, 22, (25), 254012.

12. Heremans, J. P.; Jovovic, V.; Toberer, E. S.; Saramat, A.; Kurosaki, K.; Charoenphakdee, A.; Yamanaka, S.; Snyder, G. J. Science 2008, 321, (5888), 554.

13. Demchenko, D. O.; Robinson, R. D.; Sadtler, B.; Erdonmez, C. K.; Alivisatos, A. P.; Wang, L. W. Acs Nano 2008, 2, (4), 627.

14. Dloczik, L.; Engelhardt, R.; Ernst, K.; Fiechter, S.; Sieber, I.; Konenkamp, R. Appl. Phys. Lett. 2001, 78, (23), 3687.

15. Dloczik, L.; Konenkamp, R. Nano Lett 2003, 3, (5), 651.

16. Eliseev, A. A et al. Chem. Mater. 2009, 21, (21), 5001.

17. Feng, S. H.; Xu, R. R. Acc. Chem. Res. 2001, 34, (3), 239.

18. Il Park, W.; Kim, H. S.; Jang, S. Y.; Park, J.; Bae, S. Y.; Jung, M.; Lee, H.; Kim, J. J. Mater. Chem. 2008, 18, (8), 875.

19. Jeong, U.; Xia, Y.; Yin, Y. Chem. Phys. Lett. 2005, 416, (4–6), 246.

20. Jeong, U. Y.; Camargo, P. H. C.; Lee, Y. H.; Xia, Y. N. J. Mater. Chem. 2006, 16, (40), 3893.

21. Koktysh, D. S.; McBride, J. R.; Dixit, S. K.; Feldman, L. C.; Rosenthal, S. J. Nanotechnology 2007, 18, (49).

22. Lee, J. Y.; Kim, D. S.; Park, J. H. Chem. Mater. 2007, 19, (19), 4663.

23. Moon, G. D.; Ko, S.; Xia, Y. N.; Jeong, U. Acs Nano 2010, 4, (4), 2307.

24. Sadtler, B.; Demchenko, D. O.; Zheng, H.; Hughes, S. M.; Merkle, M. G.; Dahmen, U.; Wang, L. W.; Alivisatos, A. P. J. Am. Chem. Soc. 2009, 131, (14), 5285.

25. Shim, H. S.; Shinde, V. R.; Kim, J. W.; Gujar, T. P.; Joo, O. S.; Kim, H. J.; Kim, W. B. Chem. Mater. 2009, 21, (9), 1875.

26. Shinde, V. R.; Gujar, T. P.; Noda, T.; Fujita, D.; Lokhande, C. D.; Joo, O. S. J Phys Chem C 2009, 113, (32), 14179.

27. Son, D. H.; Hughes, S. M.; Yin, Y. D.; Alivisatos, A. P. Science 2004, 306, (5698), 1009.

28. Zhang, B.; Jung, Y.; Chung, H. S.; Van Vugt, L.; Agarwal, R. Nano Lett 2010, 10, (1), 149.

29. Ren, M. L.; Liu, W.; Aspetti, C. O.; Sun, L.; Agarwal, R. Nat Commun 2014, 5, 5432.

30. Leitsmann, R.; Ramos, L. E.; Bechstedt, F. Phys Rev B 2006, 74, (8), 085309.

31. Snyder, G. J.; Toberer, E. S. Nat Mater 2008, 7, (2), 105.

32. Ball, D. L. Inorg. Chem. 1962, 1, (4), 805.

33. Suzuki, K.; Ichihara, M.; Nakagawa, K.; Maeda, K.; Takeuchi, S.; Iwanaga, H. Philos. Mag. A 1981, 43, (2), 499.

34. Osipyan, Y. A.; Smirnova, I. S. J. Phys. Chem. Solids 1971, 32, (7), 1521.

35. Meng, F.; Estruga, M.; Forticaux, A.; Morin, S. A.; Wu, Q.; Hu, Z.; Jin, S. Acs Nano 2013, 7, (12), 11369.

36. Solozhenko, V. L.; Kurakevych, O. O.; Sokolov, P. S.; Baranov, A. N. The Journal of Physical Chemistry A 2011, 115, (17), 4354.

37. Bealing, C.; Martoňák, R.; Molteni, C. Solid State Sciences 2010, 12, (2), 157.

CHAPTER 4: Chemical Transformation in Covalent Compounds

Adapted and reprinted in parts from:

R. Agarwal and R. Agarwal, "Chemical Transformation in Covalent Compounds" Under preparation for submission.

4.1 Introduction

Thus far, chemical transformation in ionic compounds of II-VI semiconductors has been studied where an ionic species, either the anion or the cation, was substituted by another element. It would be interesting to explore the chemical reactivity of compounds where the bonding is predominantly covalent in nature. Therefore, germanium telluride (GeTe), a IV-VI compound semiconductor, was chosen to study chemical transformation on reaction with selenium (Se), another chalcogenide material. Besides, the covalent nature of bonding in GeTe, it is also known to possess 8-10% structural Ge vacancies[1] which makes it an ideal material for any diffusion based chemical reaction study. It was observed that GeTe was completely transformed into single crystalline $GeSe_2$, a layered direct band-gap semiconductor compound[2], at appropriate reaction conditions. In this chapter, we discuss the reaction conditions, results and possible transformation mechanisms.

4.2 Synthesis and Characterization of GeTe Nanowires

GeTe nanowires were synthesized in a quartz tube furnace using evaporation of 99.995% pure GeTe powder[3] (Sigma-Aldrich). 5 mg of GeTe powder was placed in a quartz boat in the middle of the tube, and Si substrates covered by a 8 nm thick Au layer using e-beam evaporation were placed 15 cm downstream (referenced to the middle of

the tube). The tube was evacuated to 20 mTorr and argon carrier gas was introduced at a flow of 15 SCCM to reach a stable pressure of 5 Torr. The tube was rapidly heated to 720 °C and maintained there for 60 minutes after which the furnace was cooled by a forced airflow. GeTe nanowires, which at room temperature possess a rhombohedral crystal structure (Space group: R3*m*, a = 5.98 Å, α = 88.35°) that can be imagined as a slightly distorted rocksalt structure, generally grow along <110> axis such that the zone-axis is <111> (Figure 4.1 A). Every Ge and Te atom is in an octahedral coordination (six nearest neighbors) in a perfect rocksalt crystal structure. However, because of Peirels' distortion, each atom is off-centered from its ideal rocksalt position, thereby possessing three short and three long bonds instead of six uniform length chemical bonds[1,3](Figure 4.1 B).

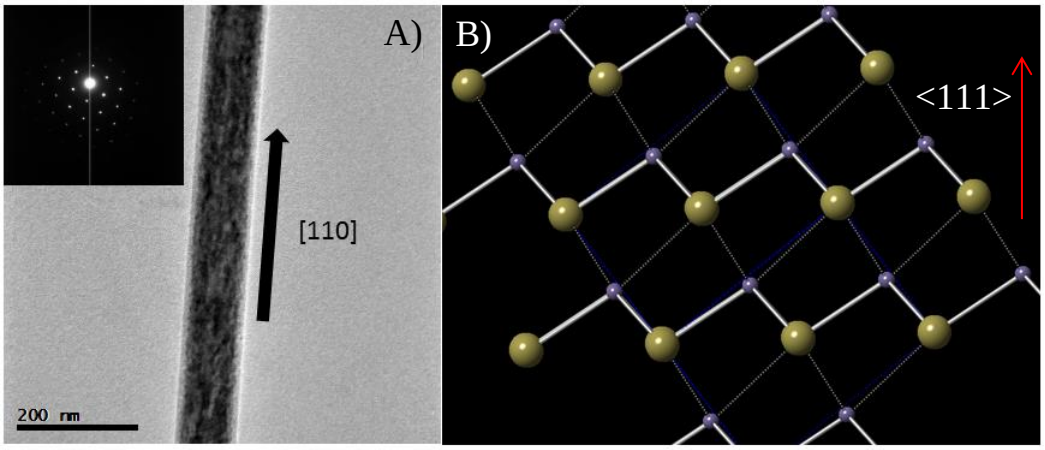

Figure 4.1 A) TEM micrograph of as-grown GeTe NW growing along <110> with zone-axis along <111> confirmed by SAED pattern (Inset). B) Crystal structure of GeTe closed packed planes stacked along <111> (red arrow) and viewed along <110> depicting short (thick white) and long (thin gray) bonds.

4.3 Chemical Reaction of GeTe with Se

As-grown GeTe NWs were transferred onto a TEM compatible SiN_x/Si grid and were placed in an experimental set-up similar to the one described in Chapters 2 and 3. After one hour of reaction at 350 °C with Se, the chemically transformed NWs were

characterized for structure and composition via TEM. The starting GeTe NWs were completely transformed into a Ge-Se compound (Figure 4.2) while still preserving the morphology and single-crystallinity of the parent nanostructure. However, the crystal structure of the chemically transformed compound was drastically different from parent GeTe and matched closest with $GeSe_2$ (Space group: $P2_1/c$, a = 7.02 Å, b = 16.8 Å, c = 11.8 Å, $\alpha = \gamma = 90^o, \beta = 90.65^o$) which is a layered monoclinic crystal that is a direct band-gap semiconductor with a band-edge emission in the green light region (E_g = 2.54 eV)[2,4].

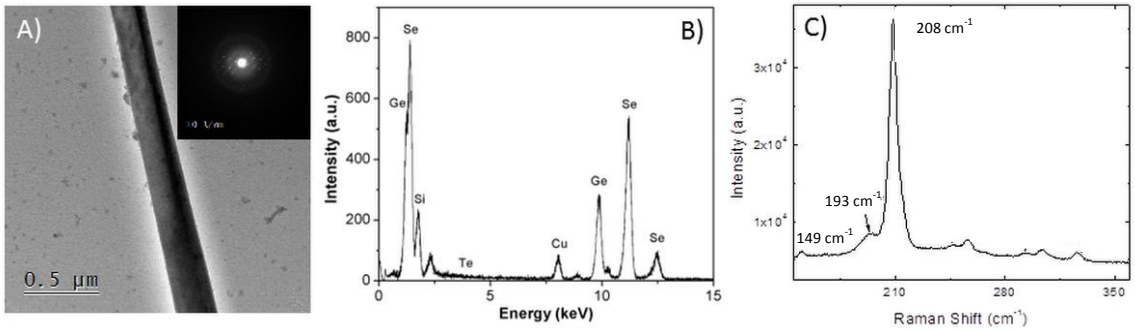

Figure 4.2 A) TEM micrograph of chemically transformed $GeSe_2$ nanowire such that the zone-axis is along *c*-direction and the long axis is at an angle of 60^0 with respect to the *b*-direction. B) EDS point scan of the completely chemically transformed NW in A confirming no residual Te. C) Raman spectrum of the same NW matching the spectrum of pure $GeSe_2$ confirming that the transformed product is indeed $GeSe_2$.

4.4 Chemical Transformation Mechanism in GeTe to form $GeSe_2$

To fully understand the transformation mechanism of single-crystalline GeTe into single crystalline, layered $GeSe_2$, we need to first understand the crystal structure of $GeSe_2$. The compound consists of layers of $GeSe_4$ tetrahedra stacked along the *c*-direction. Each layer consists of $GeSe_4$ tetrahedra connected to each other either at the vertices or the edges thereby forming a continuous network in the plane perpendicular to the *c*-axis (Figure 4.3). Even though the concept of close packed planes does not exist in

this type of a monoclinic crystal structure, it can be seen that pseudo-close packed atomic layers of Ge and Se are stacked in the *c*-direction. We believe that on introducing Se in GeTe at elevated temperatures, Se atoms diffuse through Ge vacancies and react with Ge atoms to replace Te and form Ge-Se bond. Since our reaction conditions introduce an excess of Se as compared to the given Ge atoms in relatively small nanostructures, the

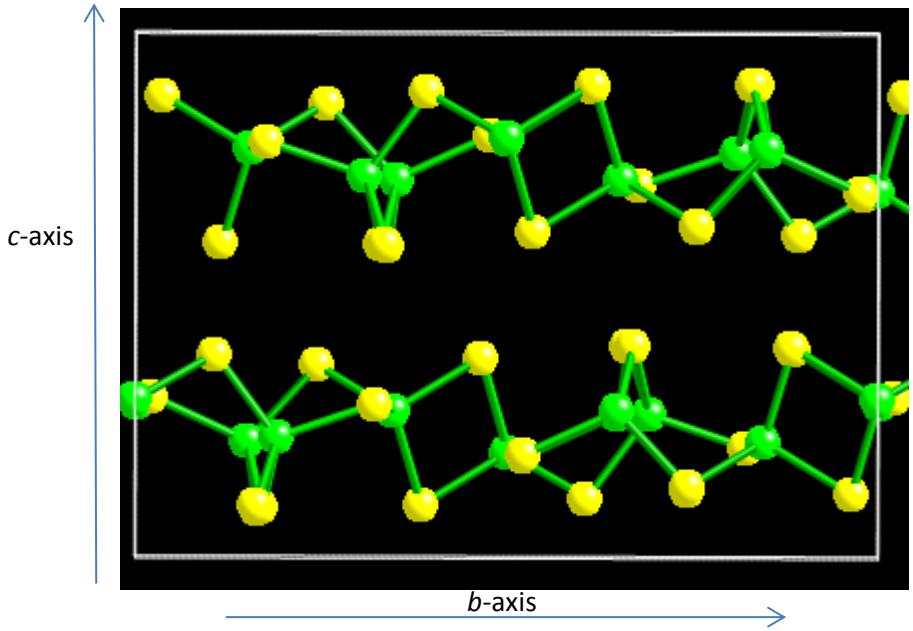

Figure 4.3 Crystal structure of a unit cell of $GeSe_2$ viewed along the *a*-axis. Every unit cell consists of two layers of $GeSe_4$ tetrahedra connected to each other by corners and edges as can be seen in the structure.

forward reaction forces the formation of $GeSe_2$ instead of orthorhombic-GeSe, even though the latter is structurally more similar to rhombohedral GeTe. Orthorhombic GeSe could very well be the intermediate phase during the chemical transformation from GeTe into $GeSe_2$ but we did not observe any such phase during our experiments including low temperature reactions. Therefore, we conclude that an excess of Se in the vicinity of Ge forces it to obtain a tetrahedral coordination with Se while slightly readjusting its atomic position locally to yield $GeSe_2$. Since the material remains single-crystalline even upon

complete chemical transformation, a large scale atomic diffusion of Ge is out of question and therefore Ge atoms act as a pseudo template such that even upon change in the crystal structure, single crystallinity of the nanostructure remains intact. Also, since Ge has only three short and strong versus the three long and weak bonds with Te, it is easier for Se to form bonds with Ge while replacing Te and thereby giving it enough room to readjust into a tetrahedral configuration. In a GeTe nanowire growing along <110> and zone-axis as <111>, there are two more <110> in the plane of the nanostructure. Upon chemical transformation of GeTe into $GeSe_2$, the *c*-axis continues to be aligned along the previous <111> zone-axis as observed in our results (Figure 4.2 B). The *b*-axis however aligns along the <110> of the previous structure, however it has three different <110> to choose from in the plane of the nanostructure. That choice is made by considering the least energy consuming transformation which corresponds to <110> direction not along the NW's long axis since atomic rearrangement in that direction would face severe repulsion from the NW's volume. On the other hand, choosing a <110> at 60° to the long axis, which is relatively smaller volume to atomically readjust over, is a more energetically favorable more and hence observed in our results (Figure 4.2 B). Also, for every unit cell of GeTe, conversion into $GeSe_2$ would require almost no expansion in the *c*-plane (close packed plane of GeTe) since the atomic densities remain almost the same before and after conversion (ρ_{GeTe} = 15.3 $Å^2$/atom and ρ_{GeSe2} = 15.68 $Å^2$/atom). Most of the expansion in readjusting the unit cell size will happen in the *c*-direction which is not as energetically challenging since the NW dimension in that direction is the minimum

(diameter). Expansion in *c*-direction (zone-axis) cannot be inferred from the TEM and AFM type experiments will be more conducive to deduce such dimensional changes.

4.5 Conclusion

Through this work, we have displayed the capability of producing novel nanostructures by performing chemical transformation in covalently bonded compounds besides ionic materials thereby further expanding the opportunities that exist in materials engineering. We also highlight the role of atomic vacancies as an important pathway for chemical transformation to occur in large nanostructures. Unlike all of our previous work, there is no strict atomic template that is followed in this chemical transformation, however the host atoms (Ge) do retain their local arrangement so as to produce a single-crystalline material even upon such a dramatic change in crystal structure thereby retaining the morphology of the nanostructure as well. This work can lead to synthesis of more such interesting materials the properties of which might be exciting for a range of applications.

4.6 References

1. A.H. Edwards, A.C. Pineda, P.A. Schultz, M.G. Martin, A.P. Thompson, H.P. Hjalmarson and C.J. Umrigar, Phys. Rev. B 73 (2006) p.045210.

2. L. Zhang et al. J. Nanomat. 2014 (2014) doi:10.1155/2014/310716.

3. P. Nukala et al., Nano Lett. 14 (2014) p.2201.

4. Wang, X., Liu, B., Wang, Q., Song, W., Hou, X., Chen, D., Cheng, Y.-b. and Shen, G. Adv. Mater., 25 (2013), p.1479.

CHAPTER 5: Morphological Transformations in II-VI Semiconducting Nanobelts

Adapted and reprinted in parts from:

R. Agarwal, D. N. Zakharov, N. M. Krook, W. Liu, J. Berger, E. A. Stach and R. Agarwal, "Real-time Observation of Morphological Transformations in II-VI Semiconducting Nanobelts via Environmental Transmission Electron Microscopy" Nano Letters 5, (2015), p.3303. Reproduced with permission.

5.1 Introduction

Semiconducting nanostructures of varied morphologies have been widely studied for their useful physical properties leading to numerous potential applications ranging from electronics, photonics, energy conversion and storage to sensors[1-10]. To realize their full potential, it is desirable to develop techniques that can also transform them into tunable and precisely controlled crystal structures and morphologies, which cannot be obtained during growth, and to understand the exact physical mechanisms behind such transformations[11-21]. We report transformation of single-crystalline wurtzite (WZ) cadmium sulfide (CdS) and cadmium telluride (CdTe) nanobelts (NBs) into a periodically branched single-crystalline NB upon heating. To understand the atomistic details of the branching mechanism, we studied the phenomenon in real-time in an environmental transmission electron microscope **(**ETEM**)** with high spatial resolution under different environmental conditions. The mechanism of branching is observed to be due to surface reconstruction of high-energy surfaces and environment-dependent anisotropic chemical etching of certain crystal surfaces. These studies, in addition to providing atomic level insights about the structural transformations in materials also

underscores the importance of in situ microscopy techniques for characterization of complex materials phenomenon.

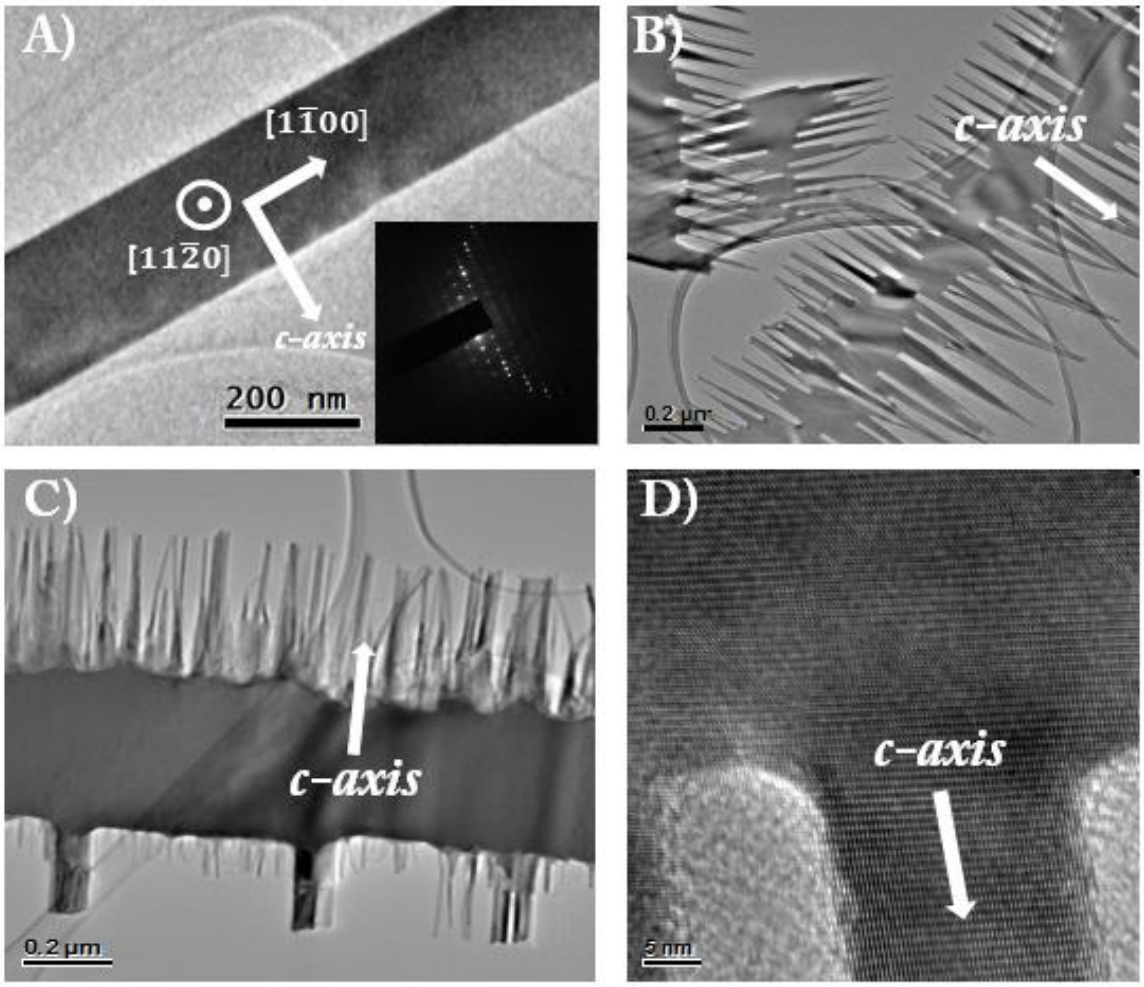

Figure 5.1 Structural characterization of branched CdS nanostructures obtained by heating CdS nanobelts in moderate vacuum. A) Transmission Electron Microscope image of an as-grown wurtzite CdS nanobelt growing perpendicular to the c-axis. Inset: selected area electron diffraction (SAED) pattern of the nanobelt. B) and C) TEM images of two periodically branched nanobelts obtained by heating CdS nanobelts inside a tube furnace (pumped down to moderate base pressure of ~25 mTorr) at 600 ^{0}C under Argon flow (100 Torr at 15 sccm). D) High-resolution TEM micrograph of the branched region confirming retention of single crystallinity and crystal orientation of the entire structure after the morphological transformation.

5.2 Branching in Wurtzite CdS Nanobelts

CdS NBs were synthesized via the vapor-liquid-solid (VLS) mechanism in a tube furnace set-up[7] at 760 ºC and were subsequently characterized for crystallography and chemical composition via TEM equipped with energy dispersive X-ray spectroscopy detector. All the measured NBs were single-crystalline and grew in the WZ crystal structure (Space group: $P6_3mc$), with a majority of them grown along the $< 1\bar{1}00 >$ direction perpendicular to the *c*-axis$< 0001 >$. Therefore, the samples are conventionally oriented along the $<11\bar{2}0 >$ zone-axis during TEM imaging (Figure 5.1 A). When CdS NBs were heated at 600 ^{0}C for 1 hour inside the same tube furnace initially pumped down to moderate vacuum levels of ~25 mTorr) in an inert atmosphere (Argon), it is interesting to note that they transformed into branched nanostructures

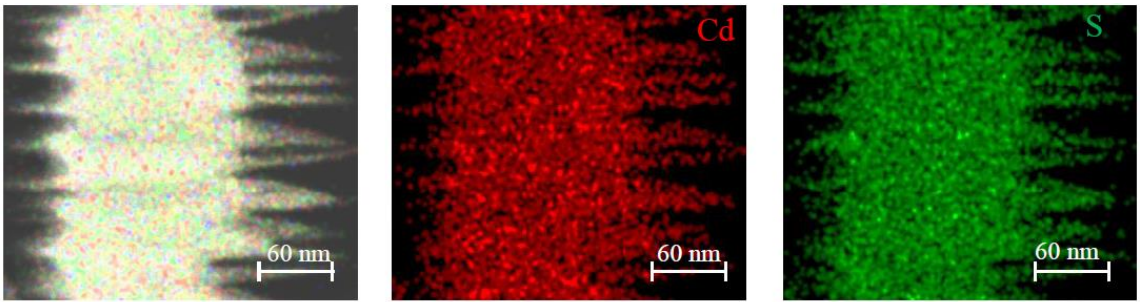

Figure 5.2 Energy dispersive X-ray spectroscopy map of a branched wurtzite CdS nanobelt obtained after heating in a tube furnace at moderate vacuum of 25 mTorr. The branched nanobelt remains chemically uniform after the morphological transformation.

comprising of a central trunk from which nanoscale whiskers emanated in both directions, with a periodicity of tens of nanometers (Figure 5.1 B-C). TEM study of the new transformed morphology showed that the branched structures retained the crystallographic characteristics (single crystallinity and WZ crystal structure, Figure 5.1 D) and chemical composition (Figure 5.2) of the parent CdS NB. The most surprising

aspect of this transformation is the presence of nano-whiskers (branches) at a periodic length scale pointing in the direction of *c*-axis along the entire length of the CdS NB.

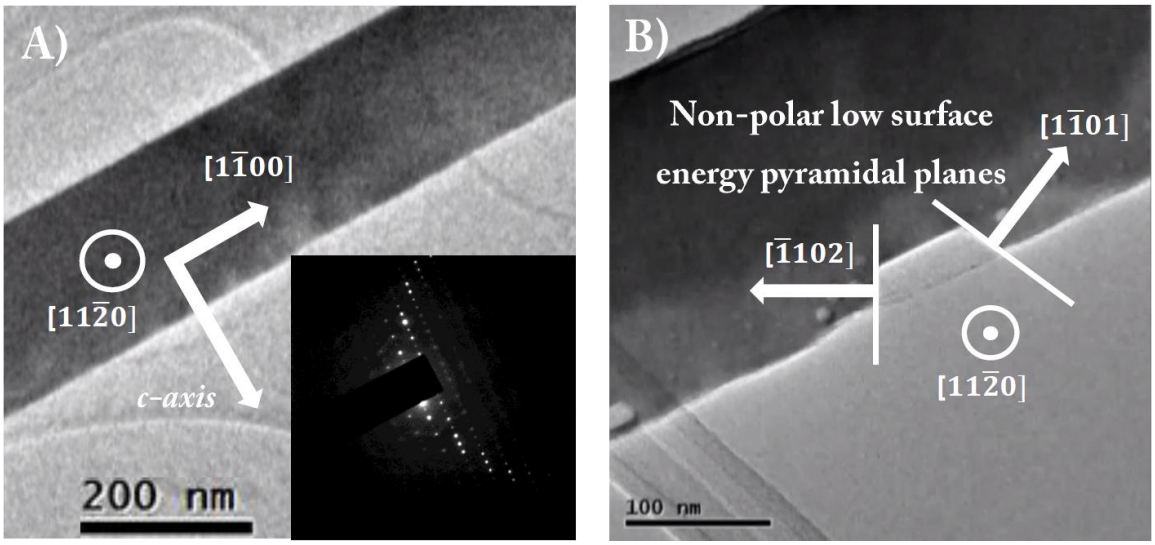

Figure 5.3 In-situ TEM heating of CdS nanobelts in ultra-high vacuum at 600 ºC. A) Transmission Electron Microscope image of an as-grown Wurtzite CdS nanobelt growing perpendicular to the c-axis. Inset: SAED pattern of the belt. B) TEM micrograph of the CdS nanobelt shown in A) after sublimation has started taken place along the pyramidal planes on heating the belt inside a TEM at 600 ^{0}C under UHV (~ 10^{-7} Torr).

This morphological anisotropy and uniqueness warrants a deeper investigation into the exact transformation mechanism. Therefore, to observe the morphological transformation process in CdS nanobelts in real-time, we performed in-situ heating experiments inside a conventional TEM under high vacuum (HV) at a base pressure of ~10^{-7} Torr using the Gatan heating holder up to a temperature of 600 ºC (ramping rate of 1 ºC/sec). Upon heating the as-grown CdS NBs (Figure 5.3 A), we could only observe sublimation of the material occurring at different regions of the NB without any periodicity or correlation with each other, with the basal plane transforming into lower energy pyramidal planes (Figure 5.3 B). Sublimation typically initiated at the lateral

edges, which then proceeded towards the core of the nanobelt, thereby increasing the surface area of the pyramidal planes at the cost of basal planes, eventually leading to the disappearance of the entire nanostructure.

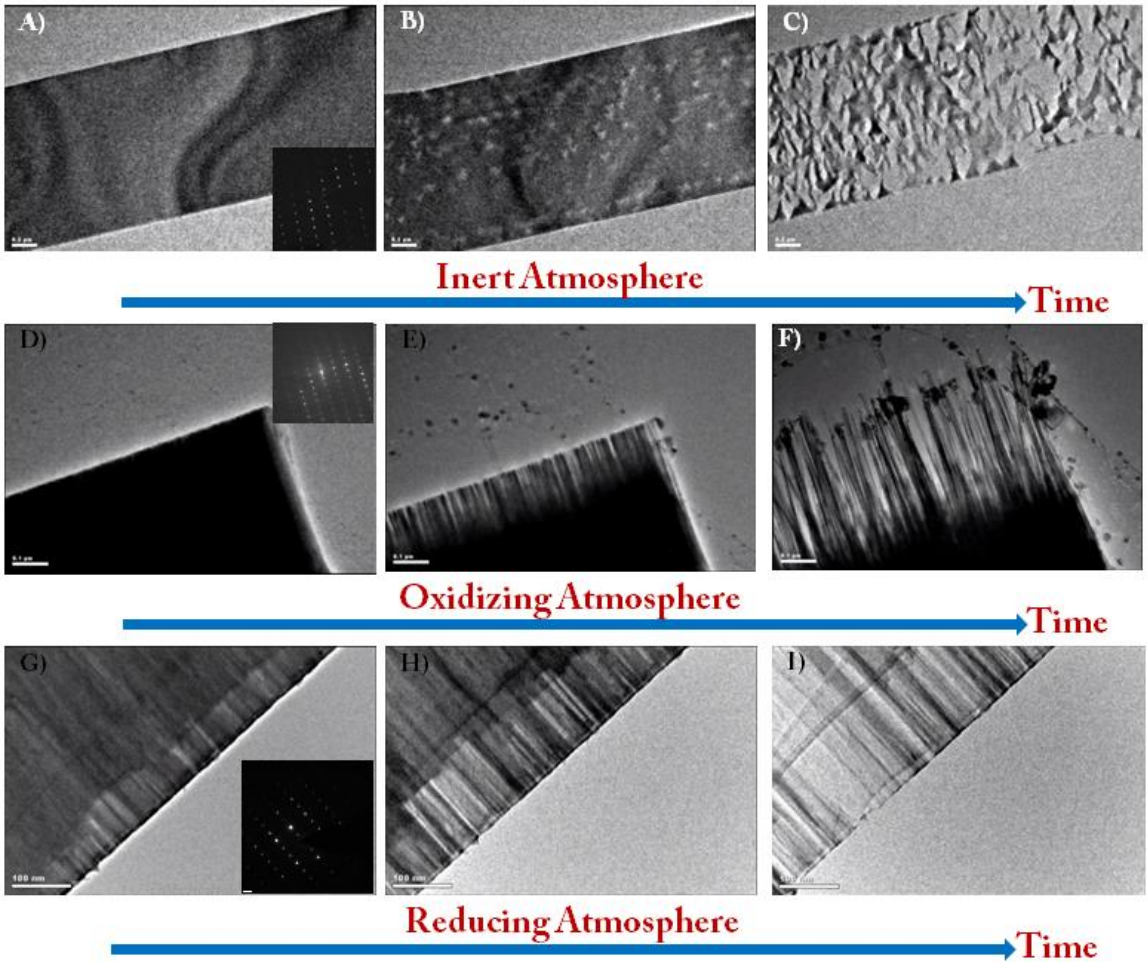

Figure 5.4 Real-time observation of morphological transformation in wurtzite CdS nanobelts upon heating in environmental TEM under various atmospheric conditions. A) - C) Snapshots from movie showing real-time sublimation but no branching in a wurtzite CdS nanobelt in the presence of inert helium (0.16 Torr) inside an environmental TEM upon heating to a temperature of 600 ^{0}C. Inset: SAED pattern of the nanobelt. Scale bar: 200 nm D) - F) Snapshots from movie showing real-time branching of a wurtzite CdS nanobelt in the presence of oxygen (0.16 Torr) inside an environmental TEM at 500 ^{0}C. Inset: SAED pattern of the nanobelt. Scale bar: 100 nm G) - I) Snapshots from movie showing real-time branch formation in a wurtzite CdS nanobelt in the presence of hydrogen (0.16 Torr) inside an environmental TEM at 500 ^{0}C. Inset: SAED pattern of the nanobelt. Scale bar: 100 nm

5.3 Environmental TEM Experiments on Wurtzite CdS

Heating experiments inside a TEM under HV differs significantly from those performed inside the tube furnace owing to the differences in the pressure and composition of the two environments. Therefore, to replicate the tube furnace conditions, i.e., higher base pressure and real gaseous environments, and also observe the mechanism of morphological transformation of CdS NBs in real-time with high spatial resolution, measurements in an ETEM are required. ETEM, a unique and powerful experimental technique, allows real-time observation and detailed study of the morphological, chemical and structural evolution of crystalline structures under a variety of atmospheric conditions with high spatial resolution[22-27]. We therefore heated CdS NBs inside the ETEM in different atmospheric conditions. Upon heating CdS NBs in an inert atmosphere (He ~0.16 Torr) up to 600 ^{0}C, only sublimation of the material was observed, similar to the results described for heating inside a HV TEM (Figure 5.4 A-C). Interestingly, upon repeating the ETEM experiment in an oxygen atmosphere (~ 0.16 Torr) at 500 ^{0}C, we observed that the CdS NBs did transform into periodically branched nanostructures (Figure 5.4 D-F) similar to the results obtained from heating them in a tube furnace (Figure 5.1). We observed that the transformation process initiated from the basal plane (lateral surface of NBs) with the development of a periodic contrast along the growth axis of the NB $< 1\bar{1}00 >$, which progressed inwards in the direction of the c-axis (Figure 5.4 E). These periodic contrasts due to modulation in the thickness of the NB gradually disappear, leaving behind what appears as the final branched product (Figure 5.4 F). The in situ ETEM heating experiment was repeated in a hydrogen atmosphere (~

0.16 Torr) and a similar morphological transformation as in the case of an oxidizing atmosphere (Figure 5.4 G-I) was observed. The only observable difference is the continuous carbon shell left behind on the transformed nanostructure which is a result of different reaction and electron beam exposure conditions. These observations demonstrate the role of reactive atmosphere in the branching mechanism of the CdS NBs.

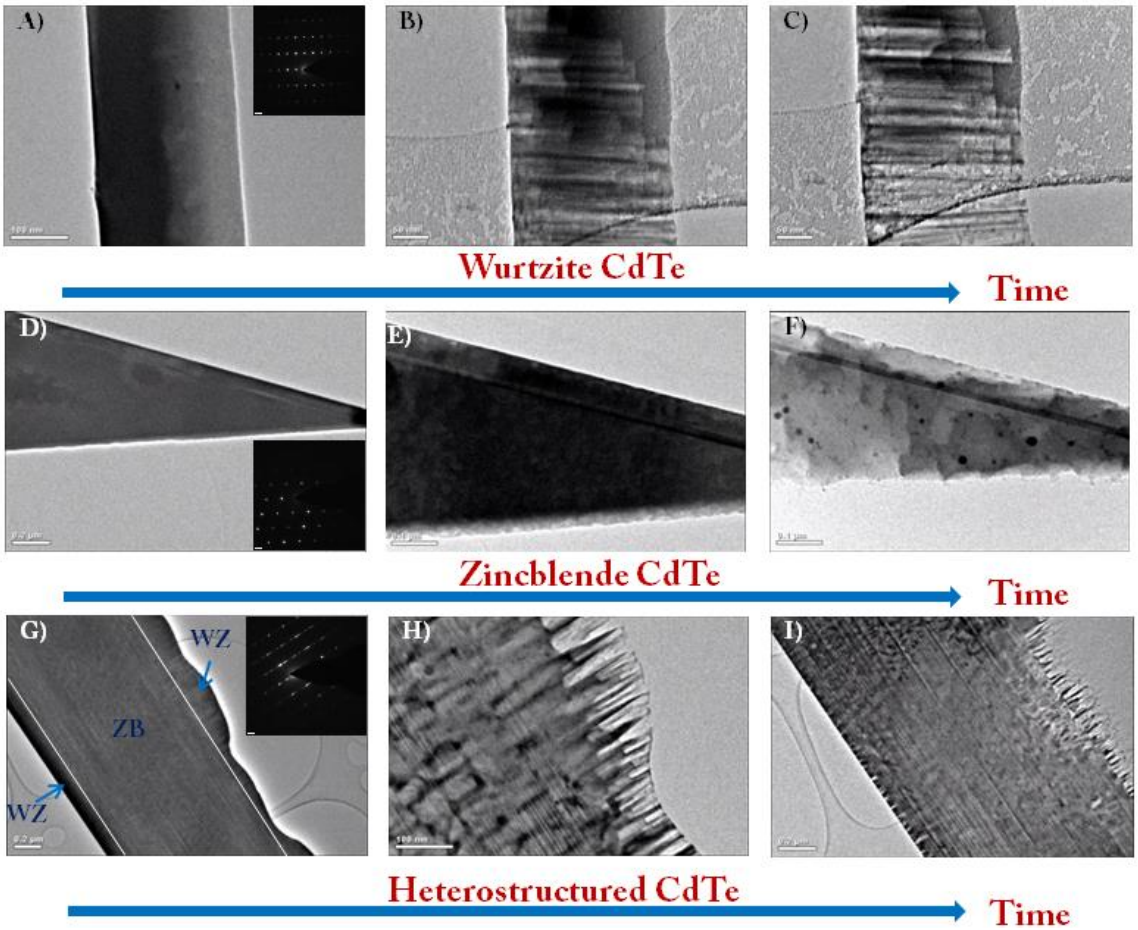

Figure 5.5 Real-time observation of morphological transformation in WZ and ZB CdTe nanobelts upon heating in environmental TEM under various atmospheric conditions A) - C) Snapshots from movie showing real-time branching of a WZ CdTe NB in the presence of oxygen (0.16 Torr) inside an environmental TEM at 500 ^{0}C. D) - F) Snapshots from movie showing real-time sublimation but no branching of a ZB CdTe NB in the presence of oxygen (0.16 Torr) inside an environmental TEM up to 600 ^{0}C. G) – I) Snapshots from movie showing real-time branching and sublimation of a CdTe NB in the presence of oxygen (0.16 Torr) inside an environmental TEM at 600 ^{0}C. The NB contains both ZB and WZ phases and branching is only observed in the WZ phase while sublimation is observed in the ZB phase.

5.4 Environmental TEM Experiments on Wurtzite and Zincblende CdTe

To further explore if the transformation to a branched structure occurs in other chemical systems upon heating NBs, we performed similar in-situ ETEM heating experiments in an oxygen atmosphere. CdTe NBs, synthesized via the VLS mechanism in a tube furnace set-up were obtained in both the WZ and zincblende (ZB) crystal structures. WZ CdTe NBs are identical to their CdS counterparts in terms of their crystallography, whereas ZB CdTe NBs (Space group:$F\bar{4}3m$) grow along the <112> direction, and their lateral surfaces are the polar {111} high surface energy planes. Therefore, the top surface of ZB CdTe NBs are the non-polar lowest surface energy {110} planes[28]. In the ETEM heating experiments, we observed that WZ CdTe NBs undergo branching when heated up to 500 ^{0}C (Figure 5.5 A-C), similar to WZ CdS NBs, whereas ZB NBs sublimate around 600 ^{0}C without any branching (Figure 5.5 D-F). Some of the CdTe NBs naturally form heterostructures with the ZB structure in the center and WZ structure towards the lateral edges; in situ heating these materials (until 600 ^{0}C) under an oxidizing atmosphere displayed branching only in the WZ region and sublimation in the ZB region (Figure 5.5 G-I). These observations establish that the morphological transformation process is dependent on the crystal structure of the material besides temperature and atmospheric conditions.

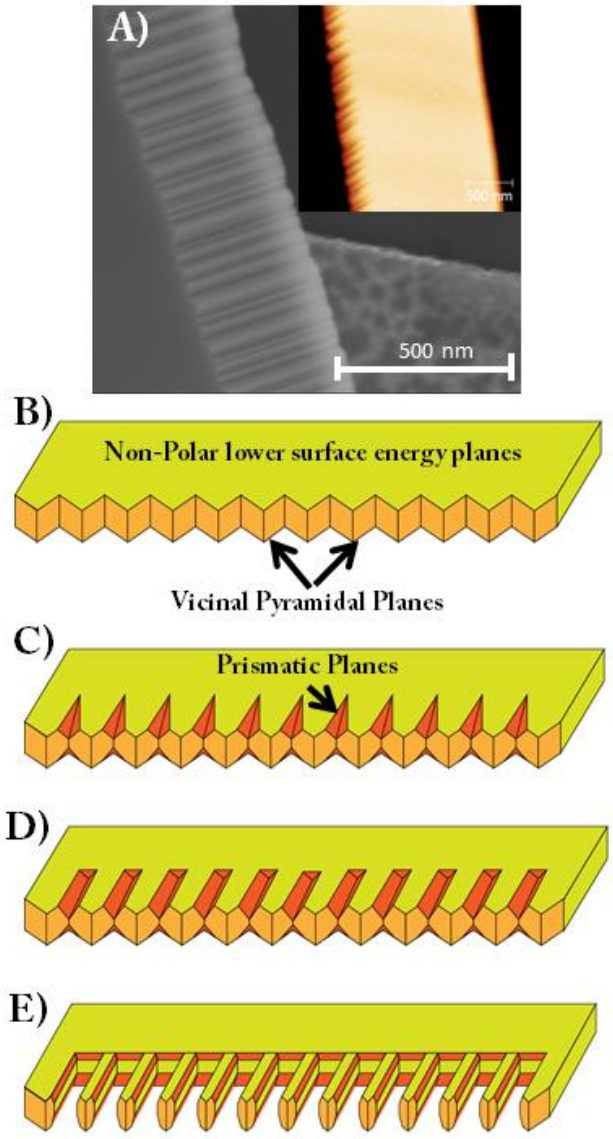

Figure 5.6 Schematic of the branching mechanism in II-VI wurtzite nanobelts. A) SEM micrograph of an as-grown CdS nanobelt clearly displaying periodic vicinal surfaces along the basal plane. Inset: AFM micrograph of a nanobelt displaying periodic vicinal surfaces. B) Schematic of an as grown wurtzite CdS nanobelt with periodic vicinal planes (exaggerated for clarity) along the basal plane. C) Subsequent etching of the prismatic planes (top surface) of the nanobelt owing to oxidation/reduction (depending on the environmental conditions) leading to periodic thickness variation along the length of the nanobelt. D) Further etching into both the prismatic and basal planes leads to periodic thickness contrasts in the nanobelt. E) Complete etching of the thinner regions leaves behind the relatively thicker parts in CdS nanobelts, leading to the formation of periodically branched nanostructures.

5.5 Mechanism of Observed Morphological Transformation

Based on these observations, a mechanism for the branching phenomenon is proposed. The branching mechanism is essentially a chemical etching process in a reactive atmosphere that proceeds only along preferential crystallographic planes thereby resulting in a highly anisotropic morphological transformation. It is well known that the basal planes of polar compounds such as II-VI semiconductors have the highest surface energy in spite of being closed packed due to their polar nature (presence of only Cd^{2+} or S^{2-} atoms), and therefore the system tries to reduce its free energy by minimizing the surface area of these planes during crystal growth[29,30]. Therefore in CdS NBs, the high surface energy basal plane, either entirely or to a large extent, often rearranges to form lower surface energy vicinal planes of the pyramidal type while the lowest surface energy top surface (non-polar prismatic plane) remains smooth[31,32]. This was confirmed via scanning electron microscopy (SEM) and atomic force microscopy (AFM) of the lateral surfaces, which show that either the entire basal plane or a large fraction of it consists of vicinal surfaces with a periodicity of tens of nanometers (Figure 5.6A), similar to the periodicity of the observed branches in the transformed structure. Therefore, the presence of these periodic vicinal surfaces is instrumental in the branching process since they provide a template for the chemical etching process to initiate while retaining the original periodicity in the transformed nanostructure**.**

For the chemical etching process of the NBs, the etchant is either oxygen or hydrogen gas that reacts with CdS at elevated temperatures, which leads to controlled sublimation of the NB material. Periodic vicinal planes, present only on the lateral edges

of as-grown WZ NBs, provide a nucleation site for the etching process to initiate (Figure 5.6 B). The initial etching should take place on the remainder of the basal plane owing to its high surface energy and chemical reactivity and convert it into vicinal surfaces (Figure 5.6 B). The etching reaction may also initiate at high-energy planar defects such as stacking faults and twin boundaries, which are often present in II-VI semiconducting materials, especially WZ/ZB heterostructured materials. This can be observed in Figure 5.5 G where etching is simultaneously initiated at stacking faults at the WZ/ZB interface in addition to the lateral surface of the nanobelt. However, this etching process lacks periodicity observed at the lateral surface since the defect plane is a continuous surface and not corrugated. The reaction should then proceed at the vicinal planes and the top surface, especially at the edges where the two meet creating notches (Figure 5.6 C). The notches will expose the other set of low surface energy prismatic planes that are parallel to the *c*-axis, thereby dictating the anisotropy in the process and ensuring that further etching occurs only along the *c*-axis. This step is also important since the periodicity of the final product is determined by the periodicity of the notches created at the edge, which in turn is dependent on the initial periodicity of the vicinal planes. Further etching of the top surface, initiated at the notches, along the *c*-axis leads to a periodic thickness modulation observed as a thickness contrast (Figure 5.6 D). Once this thinnest part of the NB is completely etched, we are left with the periodically branched NB structures (Figure 5.6 E). Inside our tube furnace set-up, which can be pumped at most to a base pressure is ~25mTorr, there is enough residual partial pressure of oxygen to cause etching of the NBs. On heating WZ NBs in HV or an inert atmosphere inside ETEM, where the base pressure (~ 10^{-7} Torr) reduces the residual oxygen to a negligible level, only sublimation

(without any chemical etching) occurs at high temperatures (~ 600 ^{0}C) due to the lack of any etching agents. As observed in our experiments, high temperature sublimation does not necessarily follow the periodicity of the vicinal planes or other crystallographic directions owing to higher sublimation rates such that the vicinal planes sublimate and merge to form large voids even before periodic notch formation can be initiated (Figure 5.3) and therefore doesn't lead to the formation of periodically branched NBs. Zincblende CdTe NBs fail to exhibit branching mechanism for several key reasons; the lateral surfaces of ZB NBs are polar high energy {111} surfaces, which may not reconfigure into vicinal planes since one of the resulting vicinal surface will be another high energy {100} polar surface[28]. Another important factor is that the top surface of the ZB NB is the non-polar low energy {110} surface: upon etching, this surface will tend to reconfigure into another set of {110} low surface energy planes. However, unlike the case of the low symmetry WZ crystal structure, these planes will not always be parallel to the [111] direction and therefore the etching mechanism loses directionality leading to only random sublimation (Figure 5.7).

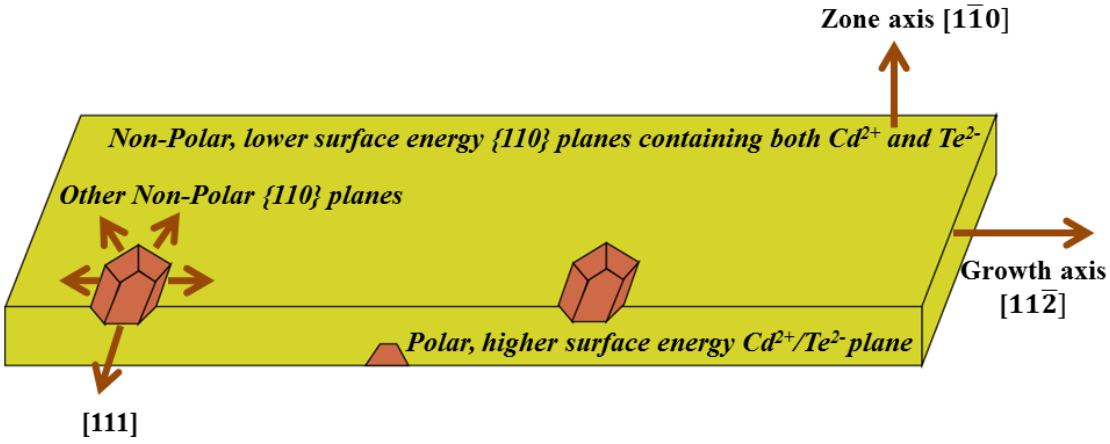

Figure 5.7 Schematic of a CdTe nanobelt undergoing etching along the {110} surfaces (orange planes) in other directions in addition to the [111] direction thus leading to a more isotropic sublimation.

5.6 Ex-situ TEM Control Experiment

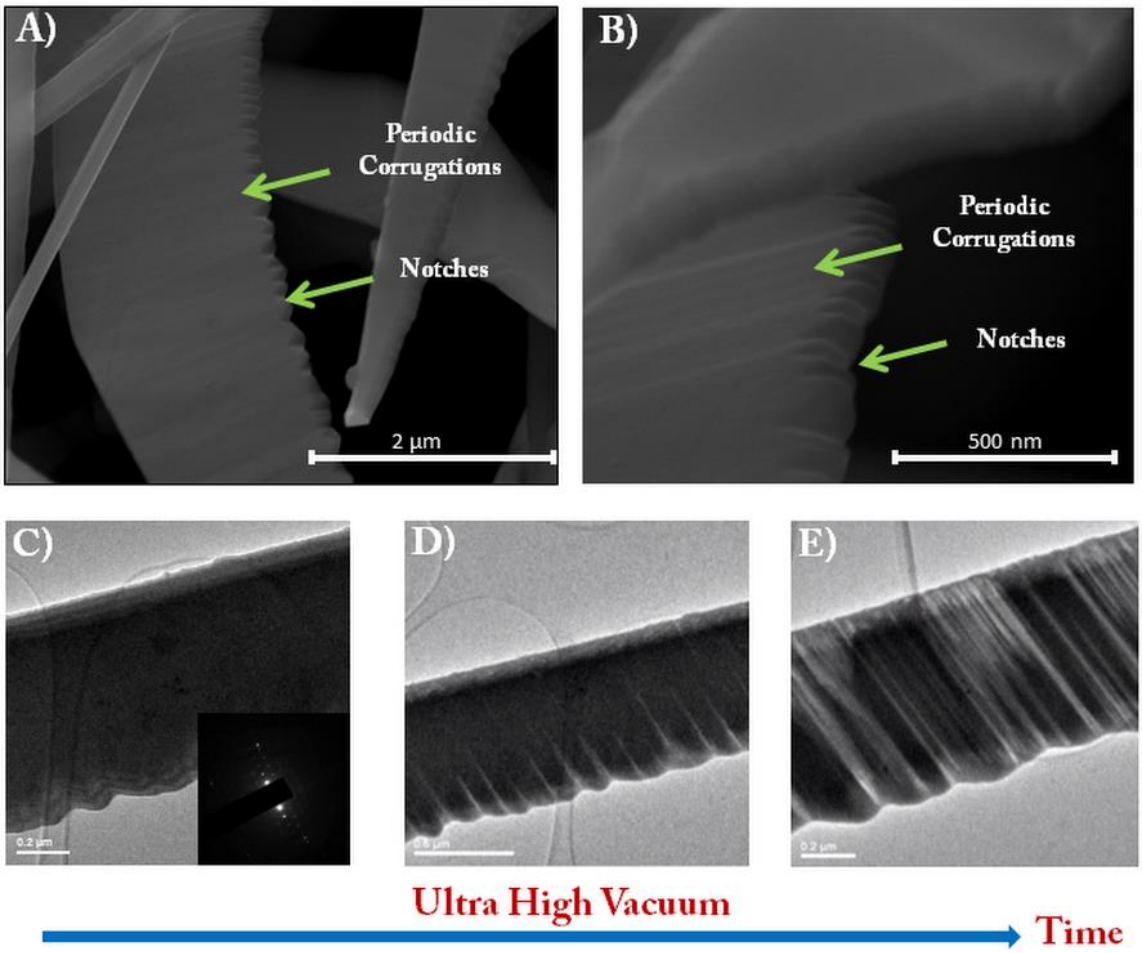

Figure 5.8 A control experiment comprising of ex-situ heating of CdS nanobelts in a tube furnace at moderate vacuum levels followed by in situ TEM heating under HV. A) – B) SEM micrograph of wurtzite CdS nanobelts after heating in a tube furnace for 10 minutes at 550 ^{0}C (base pressure 25 mTorr). Evolution of the etched surfaces on both the basal and prismatic planes can be clearly observed leading to the formation of notches. C) – E) Snapshots from movie showing real-time branch formation in a pre-notched wurtzite CdS nanobelt, whose long axis is at an angle of 105^0 with respect to *c-axis*, upon heating inside a conventional TEM under UHV at 500 ^{0}C. Inset: SAED pattern of the nanobelt confirming the crystal structure and growth direction.

To further confirm our hypothesis, a control experiment was devised to understand the role of vicinal surfaces and subsequent notch formation in the branching mechanism. As-grown WZ CdS nanobelts were heated to 550 ^{0}C in a tube furnace under ambient conditions for only 10 minutes since the purpose of the experiment was to

initiate and arrest the branching process in its nascent stage for analysis. Characterization of these partially transformed structures in SEM showed that the NBs displayed well-defined vicinal planes on the lateral surface and the beginning of the development of notches along with periodic corrugations on the top surface, which confirm the role of these vicinal surfaces in the directional etching process leading to branching (Figure 5.8 A-B). These NBs were then heated under HV inside a regular HV TEM to ~500 ^{0}C. Unlike the earlier experiments, where as-grown CdS NBs upon heating in-situ under HV sublimate randomly, pre-notched CdS NBs now transformed into periodic branches (Figure 5.8C-E), although not as well defined as the ones observed in ETEM experiments owing to a higher sublimation rate in HV TEM, which competes with the etching process. This observation illustrates the importance of the onset of the directional etching process on the top surface of the NBs, which dictates the subsequent morphological transition, and the absence of which leads to only random sublimation of the material.

5.7 Conclusion

In conclusion, we have succeeded in observing in real-time a complex morphological transformation by using a powerful technique such as the ETEM under various experimental conditions in II-VI NBs. Upon heating II-VI semiconducting NBs in a variety of environmental conditions, we observe a controlled chemical etching process which retains the original periodicity of the WZ vicinal surfaces leading to the formation of a periodically branched nanostructure**.** In addition to obtaining new insights into the atomistic mechanism of morphological transformations of nanostructures, a simple route to engineer novel morphologies at the nanoscale has been realized. Based on

these insights, new morphologies can be obtained in nanostructures, which can be utilized for a variety of electronic, photonic and sensing devices.

5.8 References

1. Agarwal, R.; Lieber, C. M. Appl. Phys. A 2006, 85, (3), 209.

2. Wei, B. Q.; Vajtai, R.; Jung, Y.; Ward, J.; Zhang, R.; Ramanath, G.; Ajayan, P. M. Nature 2002, 416, (6880), 495.

3. Hayden, O.; Agarwal, R.; Lieber, C. M. Nat. Mater. 2006, 5, (5), 352.

4. Lieber, C. M. MRS Bull. 2003, 28, (7), 486.

5. Piccione, B.; Agarwal, R.; Jung, Y.; Agarwal, R. Philos. Mag. 2013, 93, (17), 2089.

6. Xia, Y. N.; Yang, P. D.; Sun, Y. G.; Wu, Y. Y.; Mayers, B.; Gates, B.; Yin, Y. D.; Kim, F.; Yan, Y. Q. Adv. Mater. 2003, 15, (5), 353.

7. Piccione, B.; van Vugt, L. K.; Agarwal, R. Nano Lett. 2010, 10, (6), 2251.

8. Thelander, C.; Agarwal, P.; Brongersma, S.; Eymery, J.; Feiner, L. F.; Forchel, A.; Scheffler, M.; Riess, W.; Ohlsson, B. J.; Gosele, U.; Samuelson, L. Mater. Today 2006, 9, (10), 28.

9. Agarwal, R. Small 2008, 4, (11), 1872.

10. Nukala, P.; Agarwal, R.; Qian, X. F.; Jang, M. H.; Dhara, S.; Kumar, K.; Johnson, A. T. C.; Li, J.; Agarwal, R. Nano Lett. 2014, 14, (4), 2201.

11. Jung, Y.; Ko, D. K.; Agarwal, R. Nano Lett. 2007, 7, (2), 264.

12. Herman, I.; Yeo, J.; Hong, S.; Lee, D.; Nam, K. H.; Choi, J. H.; Hong, W. H.; Lee, D.; Grigoropoulos, C. P.; Ko, S. H. Nanotechnology 2012, 23, (19).

13. Zhang, B.; Jung, Y.; Chung, H. S.; Van Vugt, L.; Agarwal, R. Nano Lett. 2010, 10, (1), 149.

14. Dick, K. A.; Deppert, K.; Larsson, M. W.; Martensson, T.; Seifert, W.; Wallenberg, L. R.; Samuelson, L. Nat. Mater. 2004, 3, (6), 380.

15. Pradhan, D.; Sharon, M.; Kumar, M.; Ando, Y. J. Nanosci. Nanotechnol. 2003, 3, (3), 215.

16. Bierman, M. J.; Jin, S. Energy Environ. Sci. 2009, 2, (10), 1050.

17. Ting, J. M.; Chang, C. C. Appl. Phys. Lett. 2002, 80, (2), 324.

18. Qiu, Y. C.; Yan, K. Y.; Deng, H.; Yang, S. H. Nano Lett. 2012, 12, (1), 407.

19. Kuznetsov, D. K.; Shur, V. Y.; Negashev, S. A.; Lobov, A. I.; Pelegov, D. V.; Shishkin, E. I.; Zelenovskiy, P. S.; Platonov, V. V.; Ivanov, M. G.; Osipov, V. V. Ferroelectrics 2008, 373, 133.

20. Numao, S.; Judai, K.; Nishijo, J.; Mizuuchi, K.; Nishi, N. Carbon 2009, 47, (1), 306.

21. Yu, H. D.; Wang, D.; Han, M. Y. Adv. Mater. 2008, 20, (12), 2276.

22. Cargnello, M.; Doan-Nguyen, V. V. T.; Gordon, T. R.; Diaz, R. E.; Stach, E. A.; Gorte, R. J.; Fornasiero, P.; Murray, C. B. Science 2013, 341, (6147), 771.

23. Fujita, T.; Guan, P. F.; McKenna, K.; Lang, X. Y.; Hirata, A.; Zhang, L.; Tokunaga, T.; Arai, S.; Yamamoto, Y.; Tanaka, N.; Ishikawa, Y.; Asao, N.; Yamamoto, Y.; Erlebacher, J.; Chen, M. W. Nat. Mater. 2012, 11, (9), 775.

24. Yoshida, H.; Kuwauchi, Y.; Jinschek, J. R.; Sun, K. J.; Tanaka, S.; Kohyama, M.; Shimada, S.; Haruta, M.; Takeda, S. Science 2012, 335, (6066), 317.

25. Tao, F.; Salmeron, M. Science 2011, 331, (6014), 171.

26. Kim, S. M.; Pint, C. L.; Amama, P. B.; Zakharov, D. N.; Hauge, R. H.; Maruyama, B.; Stach, E. A. J. Phys. Chem. Lett. 2010, 1, (6), 918.

27. Stach, E. A.; Pauzauskie, P. J.; Kuykendall, T.; Goldberger, J.; He, R. R.; Yang, P. D. Nano Lett. 2003, 3, (6), 867.

28. Wright, K.; Watson, G. W.; Parker, S. C.; Vaughan, D. J. Am. Mineral. 1998, 83, (1-2), 141.

29. Ballentyne, D. W. G.; Rouse, L. M. J. Cryst. Growth 1977, 39, (2), 231.

30. Manna, L.; Wang, L. W.; Cingolani, R.; Alivisatos, A. P. J. Phys. Chem. B 2005, 109, (13), 6183.

31. Ma, C.; Ding, Y.; Moore, D.; Wang, X.; Wang, Z. L. J. Am. Chem. Soc. 2003, 126, (3), 708.

32. Ibach, H.; Emma Louise McClellan Fund., Physics of surfaces and interfaces. Springer: Berlin ; New York, 2006; p xii.

CHAPTER 6: Future Outlook

6.1 Introduction

Through our work on chemical and morphological transformation in nanostructures thus far, we hope to have convinced the reader that these techniques are a promising new avenue in the field of materials design and engineering at the nanoscale capable of synthesizing phases of material impossible to obtain otherwise. Even though we have shown a range of examples of chemical transformations, we believe that we have only scratched the surface of this emerging new technique and there is an unlimited scope of extending it to other material systems, only limited by scientific laws of bonding and one's imagination. In this section, we propose some future directions which are worth pursuing to further expand the horizons of our understanding of nanoscale materials engineering.

6.2 Replacing Cd in II-VI Semiconductors with Group III A Elements

Thus far, we have shown how chemical transformation involving replacement of Cd from II-VI semiconducting compounds with elements from group II B[1], IV A and V A (Chapter 3) affects the crystal structure and chemistry of the resulting nanostructure. However, in all these cases, the cationic species followed strict bonding coordination number withr the chalcogenide atom which was evident from the observed results. However, there are elements in the periodic table which may exist in both tetrahedral and octahedral configuration in the same compound. For example, indium from group III A of the periodic table is capable of forming In_2Se_3 type layered compound where In atoms exist in both tetrahedral as well as octahedral coordination[2]. Therefore, it would be

interesting to study the structural transition upon chemical transformation in II-VI semiconducting nanostructures, where bonding coordination is tetraheadral, into III-VI compounds, where the possibility of both tetrahedral and octahedral bonding exists. It might also be interesting to study the intermediate phases during the chemical transformation to understand how the atoms decide between tetrahedral and octahedral coordination.

6.3 Chemical Transformation in Transition Metal Di-Chalcogenides

After the emergence of graphene, the next generation of 2-D materials to attract such attention has been transition metal di-chalcogenides (TMDCs). These layered materials offer a range of physical properties as a function of their thickness in the layered direction. For example, a monolayer of molybdenum disulphide is a direct band gap semiconducting material whereas multilayer MoS_2 is an indirect band gap semiconductor[3,4]. So far, only layered materials or more specifically, materials bonded by weak van der Waals forces in a particular direction have been isolated in unit cell thickness while maintaining their chemical stability and structural integrity. This isolation process, accomplished through bottom-up or top-down approaches, has uncovered many interesting physical properties which are absent in bulk phase of these materials. Such ultra-thin 2-D films of non-layered materials is difficult to isolate naturally owing to the strong bonding nature between elements and lack of periodic and directional van der Waals type bonds. We believe that the unique morphology (monolayer) of the layered compounds can be exploited to synthesize non-layered compounds in ultra-thin film type

geometry by chemically substituting elements in mono or few layers of layered structures at elevated temperatures.

6.3.1 Substituting the chalcogenide species in MoS_2

First, to explore the reactivity of as-grown MoS_2, which is considered chemically stable, we aim to introduce Se atoms into the system at elevated temperatures. This chemical substitution reaction can utilize the sulfur vacancies in MoS_2, which can serve as primary reaction sites for incoming Se atoms. Also, since the substitution reaction aims at replacing the surface atom (S in this case), it should be energetically less challenging. The chemistry of the resulting product can be kinetically controlled by precisely modulating the concentration of precursor species and the reaction temperature. It will be interesting to study the chemically transformed products and we predict that with increasing precursor concentration, we should notice a gradual change in MoS_xSe_{2-x} alloy concentration which will eventually result in complete chemical transformation. These experiments can then be extended to bigger chalcogenide atoms such as tellurium to further explore the reactivity of MoS_2 to chalcogenide substitution. Besides chemical transformation, other important questions that will be answered are the role of lattice strain in physical properties of TMDCs and whether the structure retains its single crystallinity and morphology even upon complete chemical transformation. A systematic study of this nature will also help develop next generation of ternary and quaternary 2-D TMDCs of the type $MX_xY_yZ_{2-(x+y)}$ where M = transition metal and X,Y and Z are chalcogenide species where the physical properties such as band gap, spin –orbit

coupling, lattice parameters etc. can be fine-tuned to meet the necessary application requirements.

6.3.2 Substituting the transition metal in MoS_2

The uniqueness about MoX_2 and WX_2 stems from the nature of their bonding where the metal forms either an octahedral or a trigonal prismatic geometry having six nearest chalcogenide neighbors. The chalcogenide atoms form three bonds each with the metal atoms resulting in a unit cell consisting of two close packed layers of chalcogenide atoms sandwiching a close packed layer of metal atoms. The above described configuration stabilizes these compounds in a 2-D configuration with repeating layers of the unit cell in the third dimension held together by weak van der Waals forces and is the reason why they can exist as chemically stable monolayers when suitably grown or exfoliated from the bulk sample. Other transition metals besides Mo and W are incapable of forming such layered structures owing to a different number of d-shell electrons. For example Fe and Ni form dichalcogenides as well but in a pyrite structure which is a non-layered cubic structure held together by M-X and X-X homopolar bonds[5,6]. Also, monolayers of difficult to isolate layered compounds, such as PbS_2 and $PbSe_2$ can be easily synthesized by chemically substituting the transition metal atom with Pb. Substitution of Mo in MoS_2 with these elements will be interesting because:

1. It is of fundamental scientific interest if the transition metal in a relatively chemically stable compound will undergo chemical substitution under kinetically suitable conditions such as an excess of precursor concentration and high temperatures, aided by the presence of a large surface area.

2. It will be interesting to observe the structural and chemical evolution of such a chemically transformed structure which is now forced to exist as an ultra-thin film (a few unit cells thick) owing to the limited chalcogenide atoms originating from MoS_2 monolayer.

3. Properties of these unique, ultra-thin materials will reveal unique behavior owing to the unprecedented confinement of well-known bulk materials in one direction. For example, scaling down NiS_2 results in an insulator to metallic phase transition[7] and can also be utilized as super capacitors[8]. Also, nanostructured FeS_2 is known to be an excellent cathode material for Li^+ batteries[9].

6.4 References

1. Zhang, B.; Jung, Y.; Chung, H. S.; Van Vugt, L.; Agarwal, R. Nano Lett 2010, 10, (1), 149.

2. Pfitzner A., Lutz H.D. J Solid State Chem. 1996, 124, (2), 305.

3. R. Ganatra and Q. Zhang. ACS Nano 2014, 8, 4074.

4 M. Chhowalla, H.S. Shin, G. Eda, L.-J. Li, K. P. Loh and H. Zhang. Nature Chem. 2013, 5, 263.

5. M.L. Huggins. Phys. Rev. 1922, 19, 369.

6. P. Raybaud, G. Kresse, J. Hafner and H. Toulhoat. J. Phys.: Condens. Matter 1997, 9, 11085.

7. J. A. Wilson and G. D. Pitt. Phil. Mag. 1971, 23, 1297.

8. H. Pang, C. Wei, X. Li, G. Li, Y. Ma, S. Li, J, Chen and J. Zhang. Scientific Reports 2014, 4, 3577.

9. L. Li, M. C.-Acevedo, S. N. Girarda and S. Jin. Nanoscale, 2014, 6, 2112.

APPENDIX A: Crystallographic Characterization of II-VI Semiconducting Nanostructures via Optical Second Harmonic Generation

Adapted and reprinted in parts from:

M.-L. Ren*, R. Agarwal*, W. Liu and R. Agarwal, "Crystallographic Characterization of II-VI Semiconducting Nanostructures via Optical Second Harmonic Generation", Under review at ACS Nano Letters. * Equal Authorship

A.1 Introduction

Semiconducting nanostructures, e.g. nanowires (NWs) and nanobelts (NB), have witnessed tremendous development over the past several decades owing to their potential applications ranging from nanoelectronics[1,2] to nanophotonics[3,7]. Building a direct correlation between crystallographic structure and physical properties of a material requires complex characterization techniques. Although transmission electron microscopy (TEM) is one of the most powerful techniques to characterize nanomaterials, it is challenging or impossible to study thick (> 300 nm) nanostructures, especially if present on a non-electron transparent substrate as is often the case for functional devices. Second harmonic generation (SHG), converting two photons with electromagnetic frequency ω into a new photon with frequency 2ω, has been demonstrated as another alternative technique to probe morphology and crystallography of non-centrosymmetric materials owing to its distinct polarization properties[8-12]. Although polarized SHG has been studied in various photonic NWs, e.g. ZnO[13], GaN[14], $KNbO_3$[15,16], and ZnTe[17], and hybrids systems, e.g. Ag-coated CdS NWs[18], it hadn't been utilized until very recently to ascertain the growth orientation of single ZnS NWs[19]. Comparative studies on materials

which can exist in different crystal structures such as wurtzite (WZ) and zincblende (ZB) (e.g. CdTe) have been lacking thus far and are crucial to design functional devices with precise physical properties. In the present work, we have adopted SHG polarimetry and TEM techniques to investigate systematically semiconductor NWs and NBs with different growth orientations and crystal structures. The distinct SHG polarimetric patterns, intrinsically corresponding to materials' optical nonlinear tensor, have been observed and analyzed to determine the crystal structure (e.g. WZ or ZB) and growth orientation of various nanostructures, which is in excellent agreement with TEM observations. Moreover, materials' intrinsic properties such as optical nonlinear coefficients and geometry-dependent in-coupling coefficient have also been obtained by this novel SHG technique, thus demonstrating its utility as a powerful tool to perform crystallographic characterization in non-centrosymmetric nanostructures, especially in non-TEM compatible device architecture.

A.2 Theoretical expression of second harmonic generation (SHG) form CdS and CdTe nanostructures

Considering the coordinate systems: the crystal axes ($\vec{e}_x\vec{e}_y\vec{e}_z$) and lab coordinate system ($\vec{e}_1\vec{e}_2\vec{e}_3$) (inset of Fig. 1a). Here $\vec{e}_x$=(1,0,0), $\vec{e}_y$=(0,1,0) and $\vec{e}_z$=(0,0,1). Assume $\vec{e}_2 = (a_x, a_y, a_z)$ is along the long-axis of nanowires (NW) and nanobelts (NB), which is perpendicular to the zone axis or propagation direction of the excitation light with a unit wavevector $\vec{k} = (k_x, k_y, k_z)$ (considered as $\vec{e}_1$-direction). Then $\vec{e}_1 = \vec{k}$ and $\vec{e}_3 = (b_x, b_y, b_z) = \vec{e}_1 \times \vec{e}_2 = (a_z k_y - a_y k_z, a_x k_z - a_z k_x, a_y k_x - a_x k_y)$. Here $\sqrt{a_x^2 + a_y^2 + a_z^2} = 1$

and $\sqrt{k_x^2+k_y^2+k_z^2}=1$. The electric field, $\vec{E}_\omega=(E_{\omega,x},E_{\omega,y},E_{\omega,z})$, is in the $\vec{e}_2\vec{e}_3$ plane and has an angle of θ_ω with respect to $\vec{e}_2$,

$$\vec{E}_\omega=E_0\cos\theta_\omega\vec{e}_2+\gamma_{\omega,in}E_0\sin\theta_\omega\vec{e}_3, \tag{S1}$$

namely,

$$\begin{pmatrix}E_{\omega,x}\\E_{\omega,y}\\E_{\omega,z}\end{pmatrix}=E_0\begin{pmatrix}a_x\cos\theta_\omega+\gamma_{\omega,in}b_x\sin\theta_\omega\\a_y\cos\theta_\omega+\gamma_{\omega,in}b_y\sin\theta_\omega\\a_z\cos\theta_\omega+\gamma_{\omega,in}b_z\sin\theta_\omega\end{pmatrix}, \tag{S2}$$

where $\gamma_{\omega,in}=2/(1+\varepsilon_\omega)$, stands for the in-coupling coefficient of the electric field which is polarized perpendicular to the nanowire. ε_ω indicates the dielectric constant of the nanowire (CdS or CdTe) at the frequency of ω. Therefore, the electric field of second harmonic generation (SHG) signal, $\vec{E}_{2\omega}=(E_{2\omega,x},E_{2\omega,y},E_{2\omega,z})$, can be described by the matrix[1],

$$\begin{pmatrix}E_{2\omega,x}\\E_{2\omega,y}\\E_{2\omega,z}\end{pmatrix}=\{d_{ij}\}\begin{pmatrix}E_{\omega,x}^2\\E_{\omega,y}^2\\E_{\omega,z}^2\\2E_{\omega,y}E_{\omega,z}\\2E_{\omega,z}E_{\omega,x}\\2E_{\omega,x}E_{\omega,y}\end{pmatrix}, \tag{S3}$$

where $\{d_{ij}\}$ (i=1,2,3; j=1,2,3,4,5,6) represents second-order nonlinear tensor of the nanowire (CdS or CdTe). Then the components of SHG which is parallel ($\vec{E}_{2\omega,p}$) or perpendicular ($\vec{E}_{2\omega,s}$) to the nanowire (or $\vec{e}_2$) is written as,

$$\vec{E}_{2\omega,p}=(\vec{E}_{2\omega}\cdot\vec{e}_2)\vec{e}_2, \tag{S4}$$

$$\vec{E}_{2\omega,s} = (\gamma_{2\omega,out}\vec{E}_{2\omega}\cdot\vec{e}_3)\vec{e}_3, \tag{S5}$$

where $\gamma_{2\omega,out}$ depicts the out-coupling coefficient of the electric field which is polarized perpendicularly to the nanowire. In nanobelts, the width is typically much larger than the excitation wavelength and then $\gamma_{2\omega,out} = \gamma_{2\omega,in} = \gamma_{\omega,in} \sim 1$. The SHG intensity, whose polarization is at an angle of $\theta_{2\omega}$ with respect to $\vec{e}_2$ in the $\vec{e}_2\vec{e}_3$ plane, is given by the expression

$$I_{2\omega}(\theta_{2\omega},\theta_{\omega}) = \left|\vec{E}_{2\omega,p}\cos\theta_{2\omega} + \vec{E}_{2\omega,s}\sin\theta_{2\omega}\right|^2 \tag{S6}$$

A.2.1 SHG from CdS nanostructures

Due to the point group *6mm*, CdS nanowires of wurtzite crystal structure exhibit the second-order nonlinear coefficient tensor,

$$\{d_{ij}\} = \begin{pmatrix} 0 & 0 & 0 & 0 & d_{15} & 0 \\ 0 & 0 & 0 & d_{15} & 0 & 0 \\ d_{31} & d_{31} & d_{33} & 0 & 0 & 0 \end{pmatrix} \tag{S7}$$

Substituting Eq. (S2) and Eq. (S7) into Eq. (S3),

$$\begin{pmatrix} E_{2\omega,x} \\ E_{2\omega,y} \\ E_{2\omega,z} \end{pmatrix} = \begin{pmatrix} 2d_{15}E_{\omega,z}E_{\omega,x} \\ 2d_{15}E_{\omega,y}E_{\omega,z} \\ d_{31}E_{\omega,x}^2 + d_{31}E_{\omega,y}^2 + d_{33}E_{\omega,z}^2 \end{pmatrix} \tag{S8}$$

Therefore, the parallel and perpendicular SHG is derived from Eq. (S4) and Eq. (S5),

$$\vec{E}_{2\omega,p} = (\vec{E}_{2\omega}\cdot\vec{e}_2)\vec{e}_2 = d_{33}E_0^2[u_p\cos^2\theta_{\omega} + v_p\sin 2\theta_{\omega} + w_p\sin^2\theta_{\omega}]\vec{e}_2, \tag{S9}$$

$$\vec{E}_{2\omega,s} = (\gamma_{2\omega,out}\vec{E}_{2\omega}\cdot\vec{e}_3)\vec{e}_3 = \gamma_{2\omega,out}d_{33}E_0^2[u_s\cos^2\theta_{\omega} + v_s\sin 2\theta_{\omega} + w_s\sin^2\theta_{\omega}]\vec{e}_3, \tag{S10}$$

where

$$\begin{pmatrix} u_p \\ v_p \\ w_p \end{pmatrix} = d_{33}^{-1} \begin{pmatrix} [(2d_{15}+d_{31})-(2d_{15}+d_{31}-d_{33})a_z^2]a_z \\ \gamma_{\omega,in}[d_{15}-(2d_{15}+d_{31}-d_{33})a_z^2]b_z \\ \gamma_{\omega,in}^2[d_{31}-(2d_{15}+d_{31}-d_{33})b_z^2]a_z \end{pmatrix}, \quad \text{(S11)}$$

$$\begin{pmatrix} u_s \\ v_s \\ w_s \end{pmatrix} = d_{33}^{-1} \begin{pmatrix} [d_{31}-(2d_{15}+d_{31}-d_{33})a_z^2]b_z \\ \gamma_{\omega,in}[d_{15}-(2d_{15}+d_{31}-d_{33})b_z^2]a_z \\ \gamma_{\omega,in}^2[(2d_{15}+d_{31})-(2d_{15}+d_{31}-d_{33})b_z^2]b_z \end{pmatrix} \quad \text{(S12)}$$

If we consider $\vec{k} = (1,-1,0)/\sqrt{2}$, $a_x = a_y$ and $(b_x, b_y, b_z) = (-a_z, -a_z, 2a_x)/\sqrt{2}$. Assume the long-axis (or $\vec{e}_2$) of CdS nanowire has an angle of α_0 with respect to $\vec{e}_z$ where $\vec{e}_2$ ranges between (0,0,1) and (1,1,0), namely $\vec{e}_2 = \cos\alpha_0(0,0,1) + \sin\alpha_0(-1,-1,0)/\sqrt{2}$. Also, $a_x = a_y = -\sin\alpha_0/\sqrt{2}$, $a_z = \cos\alpha_0$.

If the nanowire is growing along [001], which is the case for the majority of CdS nanowires, then α_0 =0 and $\vec{e}_2 = \vec{e}_z$. $\vec{e}_3 = (-1,-1,0)/\sqrt{2}$, then

$$\begin{pmatrix} u_p \\ v_p \\ w_p \end{pmatrix} = \begin{pmatrix} 1 \\ 0 \\ \gamma_{\omega,in}^2 d_{31} d_{33}^{-1} \end{pmatrix} \text{ and } \begin{pmatrix} u_s \\ v_s \\ w_s \end{pmatrix} = \begin{pmatrix} 0 \\ \gamma_{\omega,in} d_{15} d_{33}^{-1} \\ 0 \end{pmatrix}$$

$$\vec{E}_{2\omega,p} = d_{33}E_0^2(\cos^2\theta_\omega + \gamma_{\omega,in}^2 d_{31} d_{33}^{-1} \sin^2\theta_\omega)\vec{e}_2, \quad \text{(S13)}$$

$$\vec{E}_{2\omega,s} = \gamma_{2\omega,out}\gamma_{\omega,in} d_{15} E_0^2 \sin 2\theta_\omega \vec{e}_3 \quad \text{(S14)}$$

In this case where θ_ω =0°, $\vec{E}_{2\omega,s} = 0$ and $\vec{E}_{2\omega,p} = d_{33}E_0^2\vec{e}_2 = d_{33}E_0^2\vec{e}_z$. While if θ_ω =90°, $\vec{E}_{2\omega,s} = 0$ and $\vec{E}_{2\omega,p} = \gamma_{\omega,in}^2 d_{31}E_0^2\vec{e}_z$.

If α_0 =90°, $\vec{e}_2 \perp \vec{e}_z$. Then $\vec{e}_2 = (-1,-1,0)/\sqrt{2}$, $\vec{e}_3 = (0,0,-1) = \vec{e}_z$,

$$\begin{pmatrix} u_p \\ v_p \\ w_p \end{pmatrix} = \begin{pmatrix} 0 \\ -\gamma_{\omega,in} d_{15} d_{33}^{-1} \\ 0 \end{pmatrix} \text{and} \begin{pmatrix} u_s \\ v_s \\ w_s \end{pmatrix} = \begin{pmatrix} -d_{31} d_{33}^{-1} \\ 0 \\ -\gamma_{\omega,in}^2 \end{pmatrix}$$

$$\vec{E}_{2\omega,p} = -E_0^2 \gamma_{\omega,in} d_{15} \sin 2\theta_\omega \vec{e}_2, \tag{S15}$$

$$\vec{E}_{2\omega,s} = -\gamma_{2\omega,out} d_{33} E_0^2 [d_{31} d_{33}^{-1} \cos^2 \theta_\omega + \gamma_{\omega,in}^2 \sin^2 \theta_\omega] \vec{e}_3 \tag{S16}$$

In this case of θ_ω =0, $\vec{E}_{2\omega,p} = 0$ and $\vec{E}_{2\omega,s} = -\gamma_{2\omega,out} d_{31} E_0^2 \vec{e}_3 = \gamma_{2\omega,out} d_{31} E_0^2 \vec{e}_z$. If θ_ω =90, $\vec{E}_{2\omega,p} = 0$ and $\vec{E}_{2\omega,s} = \gamma_{2\omega,out} \gamma_{\omega,in}^2 d_{33} E_0^2 \vec{e}_z$.

If $\alpha_0 \in (0, 90^\circ)$, $\vec{E}_{2\omega,p} = d_{33} E_0^2 u_p \vec{e}_2$ and $\vec{E}_{2\omega,s} = \gamma_{2\omega,out} d_{33} E_0^2 u_s \vec{e}_3$ by setting θ_ω =0° in Eqs. (S9) and (S10), and $\vec{E}_{2\omega,p} = d_{33} E_0^2 w_p \vec{e}_2$ and $\vec{E}_{2\omega,s} = \gamma_{2\omega,out} d_{33} E_0^2 w_s \vec{e}_3$ when θ_ω =90° in Eqs. (S9) and (S10).

A.2.2 SHG from CdTe nanostructures

Note that CdTe nanowires/nanobelts of zinc-blende crystal structure belong to the point group $4\bar{3}m$, and its second-order nonlinear coefficient is written as,

$$\{d_{ij}\} = \begin{pmatrix} 0 & 0 & 0 & d_{14} & 0 & 0 \\ 0 & 0 & 0 & 0 & d_{14} & 0 \\ 0 & 0 & 0 & 0 & 0 & d_{14} \end{pmatrix} \tag{S17}$$

Substituting Eq. (S2) and Eq. (S17) into Eq. (S3) and obtaining,

$$\begin{pmatrix} E_{2\omega,x} \\ E_{2\omega,y} \\ E_{2\omega,z} \end{pmatrix} = \begin{pmatrix} 2d_{14} E_{\omega,y} E_{\omega,z} \\ 2d_{14} E_{\omega,z} E_{\omega,x} \\ 2d_{14} E_{\omega,x} E_{\omega,y} \end{pmatrix} \tag{S18}$$

According to Eq. (S4) and Eq. (S5), we obtain,

$$\vec{E}_{2\omega,p} = (\vec{E}_{2\omega} \cdot \vec{e}_2) \vec{e}_2 = 2d_{14} E_0^2 [u_p \cos^2 \theta_\omega + v_p \sin 2\theta_\omega + w_p \sin^2 \theta_\omega] \vec{e}_2, \tag{S19}$$

$$\vec{E}_{2\omega,s} = (\vec{E}_{2\omega} \cdot \vec{e}_3)\vec{e}_3 = \gamma_{2\omega,out} 2d_{14} E_0^2 [u_s \cos^2\theta_\omega + v_s \sin 2\theta_\omega + w_s \sin^2\theta_\omega]\vec{e}_3, \quad \text{(S20)}$$

where

$$\begin{pmatrix} u_p \\ v_p \\ w_p \end{pmatrix} = \begin{pmatrix} 3a_x a_y a_z \\ \gamma_{\omega,in}(a_z a_y b_x + a_x a_z b_y + a_y a_x b_z) \\ \gamma_{\omega,in}^2(a_x b_y b_z + a_y b_z b_x + a_z b_x b_y) \end{pmatrix}, \quad \text{(S21)}$$

$$\begin{pmatrix} u_s \\ v_s \\ w_s \end{pmatrix} = \begin{pmatrix} (a_z a_y b_x + a_x a_z b_y + a_y a_x b_z) \\ \gamma_{\omega,in}(a_x b_y b_z + a_y b_z b_x + a_z b_x b_y) \\ 3\gamma_{\omega,in}^2 b_x b_y b_z \end{pmatrix} = \begin{pmatrix} v_p/\gamma_{\omega,in} \\ w_p/\gamma_{\omega,in} \\ 3\gamma_{\omega,in}^2 b_x b_y b_z \end{pmatrix} \quad \text{(S22)}$$

For $\vec{k} = (1,-1,0)/\sqrt{2}$,

$$\begin{pmatrix} u_p \\ v_p \\ w_p \end{pmatrix} = \begin{pmatrix} 3a_x a_y a_z \\ \dfrac{\gamma_{\omega,in}}{\sqrt{2}}\{(a_x + a_y)(a_y a_x - a_z^2)\} \\ \dfrac{\gamma_{\omega,in}^2}{2} a_z[a_z + (a_x + a_y)][a_z - (a_x + a_y)] \end{pmatrix}, \quad \text{(S23)}$$

$$\begin{pmatrix} u_s \\ v_s \\ w_s \end{pmatrix} = \begin{pmatrix} v_p/\gamma_{\omega,in} \\ w_p/\gamma_{\omega,in} \\ \dfrac{3\gamma_{\omega,in}^2}{2\sqrt{2}} a_z^2 (a_x + a_y) \end{pmatrix} \quad \text{(S24)}$$

Similar to the CdS case, we assume the long-axis ($\vec{e}_2$) is at an angle α_0 with respect to [001], therefore, $a_x = a_y = -\sin\alpha_0/\sqrt{2}$, $a_z = \cos\alpha_0$.

If $\alpha_0 = -(180^\circ - 35.26^\circ)$, $\cos\alpha_0 = -\sqrt{2/3}$, $\sin\alpha_0 = -1/\sqrt{3}$, $\vec{e}_2 = (1,1,-2)/\sqrt{6}$ and the growth axis is $[11\bar{2}]$. Then $a_x = a_y = 1/\sqrt{6}$, $a_z = -2/\sqrt{6}$, $\vec{e}_3 = (1,1,1)/\sqrt{3}$, and

$$\begin{pmatrix} u_p \\ v_p \\ w_p \end{pmatrix} = \begin{pmatrix} -\frac{1}{\sqrt{6}} \\ -\gamma_{\omega,in}\frac{1}{2\sqrt{3}} \\ 0 \end{pmatrix} \text{ and } \begin{pmatrix} u_s \\ v_s \\ w_s \end{pmatrix} = \begin{pmatrix} -\frac{1}{2\sqrt{3}} \\ 0 \\ \gamma_{\omega,in}^2\frac{1}{\sqrt{3}} \end{pmatrix}$$

$$\vec{E}_{2\omega,p} = 2d_{14}E_0^2[-\frac{1}{\sqrt{6}}\cos^2\theta_\omega - \gamma_{\omega,in}\frac{1}{2\sqrt{3}}\sin 2\theta_\omega]\vec{e}_2, \quad \text{(S25)}$$

$$\vec{E}_{2\omega,s} = \gamma_{2\omega,out}2d_{14}E_0^2[-\frac{1}{2\sqrt{3}}\cos^2\theta_\omega + \gamma_{\omega,in}^2\frac{1}{\sqrt{3}}\sin^2\theta_\omega]\vec{e}_3. \quad \text{(S26)}$$

When $\theta_\omega = 0^\circ, \vec{E}_{2\omega,p} = -\frac{2}{\sqrt{6}}d_{14}E_0^2\vec{e}_2$ and $\vec{E}_{2\omega,s} = -\gamma_{2\omega,out}\frac{1}{\sqrt{3}}d_{14}E_0^2\vec{e}_3$; when $\theta_\omega = 90^\circ$, $\vec{E}_{2\omega,p} = 0$ and $\vec{E}_{2\omega,s} = \gamma_{2\omega,out}\gamma_{\omega,in}^2\frac{2}{\sqrt{3}}d_{14}E_0^2\vec{e}_3$, then

$$I_{2\omega}(\theta_{2\omega}, \theta_\omega = 90^\circ) = \left|\vec{E}_{2\omega,p}\cos\theta_{2\omega} + \vec{E}_{2\omega,s}\sin\theta_{2\omega}\right|^2 \propto \sin^2\theta_{2\omega}, \quad \text{(S27)}$$

$$I_{2\omega}(\theta_{2\omega}, \theta_\omega = 0^\circ) = \left|\vec{E}_{2\omega,p}\cos\theta_{2\omega} + \vec{E}_{2\omega,s}\sin\theta_{2\omega}\right|^2 \propto \left|\cos\theta_{2\omega} + x\sin\theta_{2\omega}\right|^2, \quad \text{(S28)}$$

where $x = \gamma_{2\omega,out}/\sqrt{2}$.

A.3 Experimental Set-up

In order to interpret the data, consider the following coordinate systems: lab coordinate system ($\vec{e}_1\vec{e}_2\vec{e}_3$) and crystal axes ($\vec{e}_x\vec{e}_y\vec{e}_z$) with $\vec{e}_x$=(1,0,0), $\vec{e}_y$=(0,1,0) and $\vec{e}_z$=(0,0,1), and assume $\vec{e}_2$ is parallel to NW's long-axis, $\vec{e}_1$ is parallel to propagation direction of the incident laser beam, and the electric field E_ω (or $E_{2\omega}$) is polarized in the $\vec{e}_2\vec{e}_3$ plane at an angle of θ_ω (or $\theta_{2\omega}$) with respect to $\vec{e}_2$ (Figure A.1 A, inset). The subscript ω and 2ω represents the frequency of fundamental wave (FW) and second

harmonic generation (SHG) signal respectively. In the $\vec{e}_2\vec{e}_3$ plane, transverse magnetic (TM) component of SHG with electric field polarized along the NW long-axis ($\theta_{2\omega}$=0°) is written as (Eq. S9),

$$\vec{E}_{2\omega,p} = E_0^2[u_p \cos^2\theta_\omega + v_p \sin 2\theta_\omega + w_p \sin^2\theta_\omega]\vec{e}_2, \quad (1)$$

and the transverse electric (TE) component of SHG with polarization perpendicular to the NW long-axis ($\theta_{2\omega}$=90°) is (Eq. S10),

$$\vec{E}_{2\omega,s} = \gamma_{2\omega,out} E_0^2[u_s \cos^2\theta_\omega + v_s \sin 2\theta_\omega + w_s \sin^2\theta_\omega]\vec{e}_3 \quad (2)$$

Then TM- and TE-polarized SHG intensity becomes, $I_{2\omega,p} = \left|\vec{E}_{2\omega,p}\right|^2$ and $I_{2\omega,s} = \left|\vec{E}_{2\omega,s}\right|^2$, and polarimetric SHG is described as (Eq. S6),

$$I_{2\omega}(\theta_{2\omega}, \theta_\omega, \alpha_0) = \left|\vec{E}_{2\omega,p}\cos\theta_{2\omega} + \vec{E}_{2\omega,s}\sin\theta_{2\omega}\right|^2 \quad (3)$$

where E_0 represents the electric field of the incident light (FW), α_0 is the orientation angle between $\vec{e}_2$ (or NW's long-axis) and $\vec{e}_z$ (c-axis), $\gamma_{\omega,in}$ is the in-coupling coefficient of FW (ω), while $\gamma_{2\omega,out}$ is the out-coupling coefficient of SHG signal (2ω), the parameter, y_i (y=u, v, w; and i=p, s), is dependent on the orientation angle (α_0) and second-order nonlinear coefficients of the material (Eqs. S11, S12, S21 and S22). Among these, $u_{p,s}$ relates to TM-polarized component of FW ($E_{\omega,p}^2$), $w_{p,s}$ is associated with TE-polarized component ($E_{\omega,s}^2$) while $v_{p,s}$ for the cross term ($E_{\omega,p}E_{\omega,s}$) if the relative nonlinear coefficient is non-vanishing.

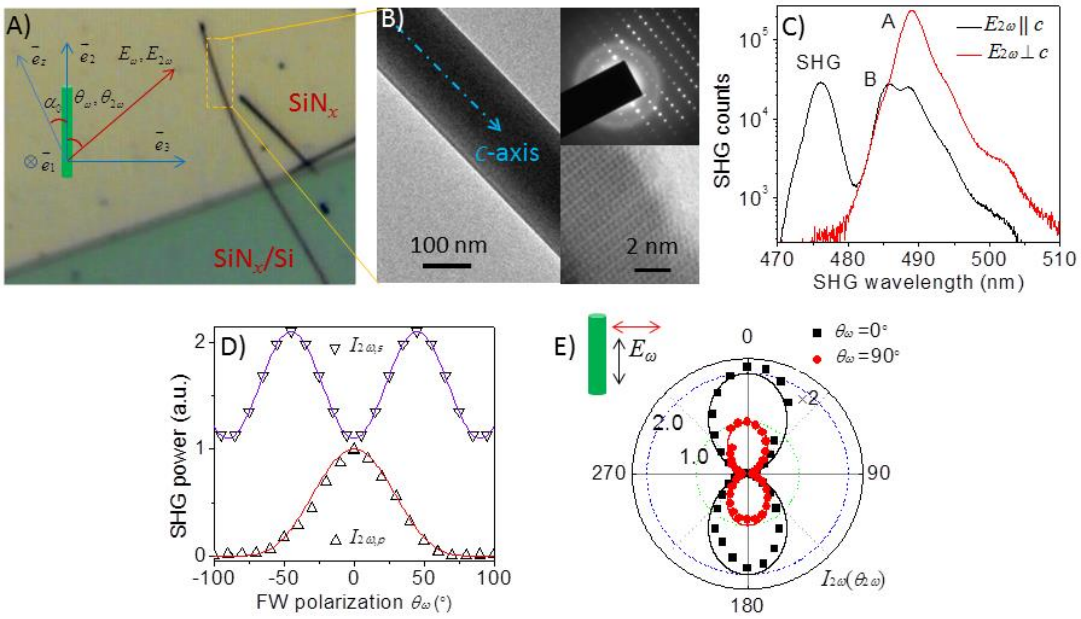

Figure A.1 Structural analysis of wurtzite CdS nanowire grown along the c-axis (c||NW) from photoluminescence and optical SHG polarimetry. A) Dry-transferred CdS NWs on e-beam transparent SiNx membrane (TEM grids). Inset indicates the coordinate systems (see main text). B) TEM micrograph of a CdS NW grown along the c-axis (α0=0°, c||NW) confirmed by the selected area electron diffraction (SAED) pattern (top inset) and high resolution TEM image (bottom inset). C) SHG and PL spectrum from the selected CdS NW (c||NW). The excitation laser is polarized along NW and tuned at a wavelength of 950 nm. D) TM- (I2ω,p) and TE- (I2ω,s) polarized SHG as a function of excitation polarization angle (θω), fitted (solid lines) using Eq. S14 for I2ω,p and Eq. S15 for I2ω,s E) Polarimetric plot of total SHG intensity (I2ω) under TM (black, θω=0°) and TE (red, θω=90°) excitation.

Single-crystalline CdS and CdTe NWs and NBs were synthesized via the vapor-liquid-solid mechanism in a tube furnace set-up[20,21]. In order to perform TEM characterization on the same nanostructures on which SHG polarimetry was studied, nanostructures were dry-transferred onto TEM compatible, e-beam transparent SiN_x/Si grids (Figure A.1 A). NWs and NBs were first characterized via TEM for crystal structure and growth orientation and then analyzed via optical SHG technique in an optical microscopy cryostat (Janis, ST-500) equipped with ×60, 0.7 NA objective (Nikon). In order to perform SHG polarimetry, a linearly polarized Ti: sapphire laser

(Chameleon) was utilized which can be tuned from 680 nm to 1080 nm with ~150 fs pulse width and 80 MHz repletion rate focused onto individually selected nanostructures with the laser spot size of ~2 μm at ~5 mW (average) power. The polarization of the laser was rotated in plane by using a half-wave plate (Thorlabs, AHWP05M-980). In particular, on a CdS NW with the *c*-axis along NW's long-axis (Figure A.1 B), low temperature measurements were performed at 77K by tuning the excitation laser at 950 nm, and it exhibited polarized light emission, including SHG signal at 475 nm and two-photon absorption induced photoluminescence (PL). In the PL emission, the A exciton peak near 488 nm is observed to be polarized perpendicular to the *c*-axis (or NW's long-axis) while the B exciton peak is isotropic near 485 nm, as reported previously[22]. Although the *c*-axis of a WZ structure can be detected from anisotropic polarization of A exciton emission, the experiment usually requires low temperature for observing strong and sharp A exciton peak. In contrast, the SHG signal polarized along the *c*-axis in WZ CdS, originating from its nonlinear coefficient d_{33}, is a clear indication of the crystal orientation of the nanostructure (more discussion below)[23]. This technique can work at any arbitrary temperature and optical frequency (FW), and can be instrumental in characterizing materials that display poor or no PL. In order to illustrate the utility of optical SHG polarimetry in structural characterization, we studied SHG at room temperature systematically in three WZ CdS nanostructures with different orientations (*c*-axis or $\vec{e}_z$): *c*-axis parallel to the long-axis (c||NW, α_0=0), *c*-axis perpendicular to the long-axis ($c \perp$ NW, α_0=90°) and *c*-axis at an angle of 56° with respect to the long-axis in

the counter-clockwise direction ($c\angle$NW, α_0 = -56°). The excitation laser was tuned at 1020 nm which produced the SHG signal at 510 nm accordingly.

A.4 CdS Nanowire Growing Along *c*-axis

In a CdS NW shown in Figure A.1 B, the selected area electron diffraction (SAED) pattern and high resolution TEM image reveal that the *c*-axis is aligned along the NW's long-axis (c||NW, α_0=0). In this simple case, TM- and TE-polarized SHG signal was measured as a function of the excitation polarization angle (θ_ω). As shown in Figure A.1 D, TE-polarized SHG ($I_{2\omega,s}$) exhibits sinusoidal like shape ($\sin^2\theta_\omega$) with the peaks at ±45° and dips at 0° and ±90°, and fits well to Eq. 2 and Eq. S14. In this process, the only non-vanishing nonlinear coefficient is d_{15} which contributes to the SHG signal by combining the cross term ($E_{\omega,p}E_{\omega,s}$). For TM-polarized SHG under TM excitation (θ_ω=0°), $I_{2\omega,p} \propto d_{33}^2$ while under TE excitation (θ_ω=90°), $I_{2\omega,p} \propto \gamma_{\omega,in}^2 d_{31}^2$ (Eq. S13). The in-coupling efficiency ($\gamma_{\omega,in}^2$) under TE excitation is smaller in comparison to TM excitation in a small NW (d_{NW} ~140 nm << λ_{FW})[24, 25]. In addition, the nonlinear coefficient, d_{31}, is approximately 50% smaller than the largest tensor element, d_{33}[23](Eq. S13). Therefore, TM-polarized SHG intensity ($I_{2\omega,p}$) is much stronger under TM excitation as compared to TE excitation and follows $\cos^4\theta_\omega$profile[18]. In Figure A.1 E, the SHG signal measured under TM and TE excitation by rotating the polarizer in front of the detector and fitted by Eq. 3 shows that the SHG signal was always TM-polarized along NW's long-axis (or *c*-axis in this case) regardless of TM and TE excitation, which exactly matches the second-order nonlinear tensor of CdS (Eq. S7).

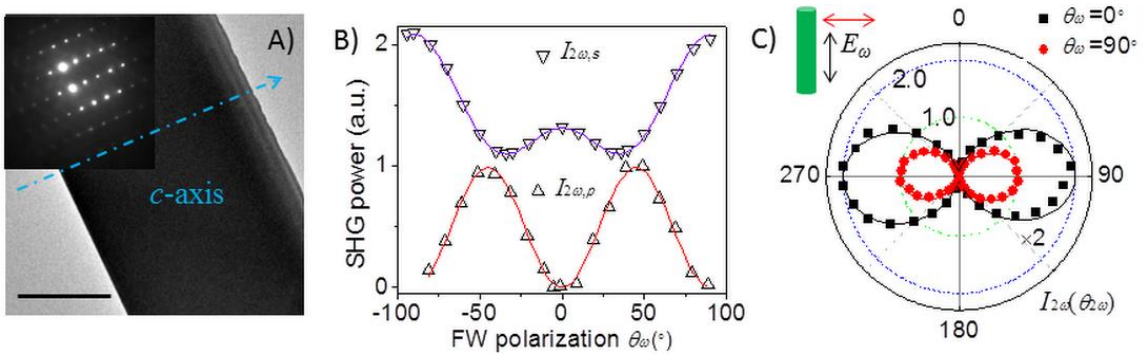

Figure A.2 Structural analysis of wurtzite CdS nanowire grown perpendicular to the *c*-axis (*c*⊥NW) from optical SHG polarimetry. A) TEM micrograph of CdS NW (α_0=90°, *c*⊥NW). Inset: SAED pattern of the NW indicating WZ crystal structure and *c*⊥NW growth orientation. Scale bar: 500 nm. B) TM- and TE-polarized SHG signal as a function of the excitation polarization angle. C) Polarimetric plot of total SHG intensity ($I_{2\omega}$) under TM (black, θ_ω=0°) and TE (red, θ_ω=90°) excitation.

A.5 CdS Nanobelt Growing Perpendicular to *c*-axis

For the case of WZ CdS NW with the *c*-axis perpendicular to the long axis of the NW (*c*⊥NW, α_0=90°) (Figure A.2 A), TM-polarized SHG intensity ($I_{2\omega,p}$) exhibits $\sin^2$ θ_ω profile as a function of the excitation polarization angle θ_ω (Eq. S15), which only depends on the nonlinear coefficient d_{15} (Figure A.2 B). More interestingly, TE-polarized SHG intensity ($I_{2\omega,s}$) reveals features (dips and peaks), which were not observed for the case where *c-axis*||NW (Figure A.1 D). TE-polarized SHG intensity under TM excitation (θ_ω=0°) is $I_{2\omega,s} \propto d_{31}^2$ while under TE excitation (θ_ω=90°) is $I_{2\omega,s} \propto \gamma_{\omega,in}^2 d_{33}^2$ (Eq. S16). Owing to a relatively smaller value of nonlinear coefficient ($d_{31} \sim d_{33}/2$), TE-polarized SHG signal excited at θ_ω=0° (TM excitation) is approximately five times smaller than that at θ_ω=90° (TE excitation). As the excitation polarization angle θ_ω changes from 0° to 90°, TE-polarized SHG first decreases and then increases to the maximum at θ_ω=90°. The dip feature observed in the SHG signal (Figure A.2 B, $I_{2\omega,s}$) can be attributed to the

destructive interference between TM-and TE-excited components of SHG and revealed d_{31} possessing an opposite sign with respect to d_{33}[23]. In Figure A.2 C, the polarimetric SHG plotted under TM and TE excitation shows that the SHG signal is always TE-polarized but again along the *c*-axis. Therefore, from the two cases (*c*||NW and $c \perp$ NW), we conclude that the SHG signal is always polarized along the *c*-axis under both TM and TE excitation for WZ nanostructures.

A.6 CdS Nanobelt Growing at an Angle to *c*-axis

For a more complex case, we investigated another CdS NW where the *c-axis* was at an angle of 56° to the NW's long-axis in the counter-clockwise direction ($c \angle$NW, α_0 = -56, Figure A.3 A). As compared to the previous two cases (c || NW and c ⊥NW), TM- and TE-polarized SHG signal from this NW exhibits asymmetric response with respect to the rotation of the excitation polarization (Figure A.3 B). The polarimetric SHG signal differs under TM and TE excitation (Figure A.3 A), indicating its polarization does not follow the *c*-axis direction. These observations can be explained by a combination of factors such as the in- and out-coupling efficiency and different values of nonlinear coefficients (d_{15}, d_{31}, and d_{33}). Therefore, TM-and TE-excited SHG patterns along with the excitation polarization dependence of TM- and TE-polarized SHG was analyzed to extract NW orientation (Eq. S9 and S10). From fitted and measured data, NW's *c*-axis was determined to be ~54° in the counter-clockwise direction with respect to NW's long-axis, in good agreement with TEM characterization.

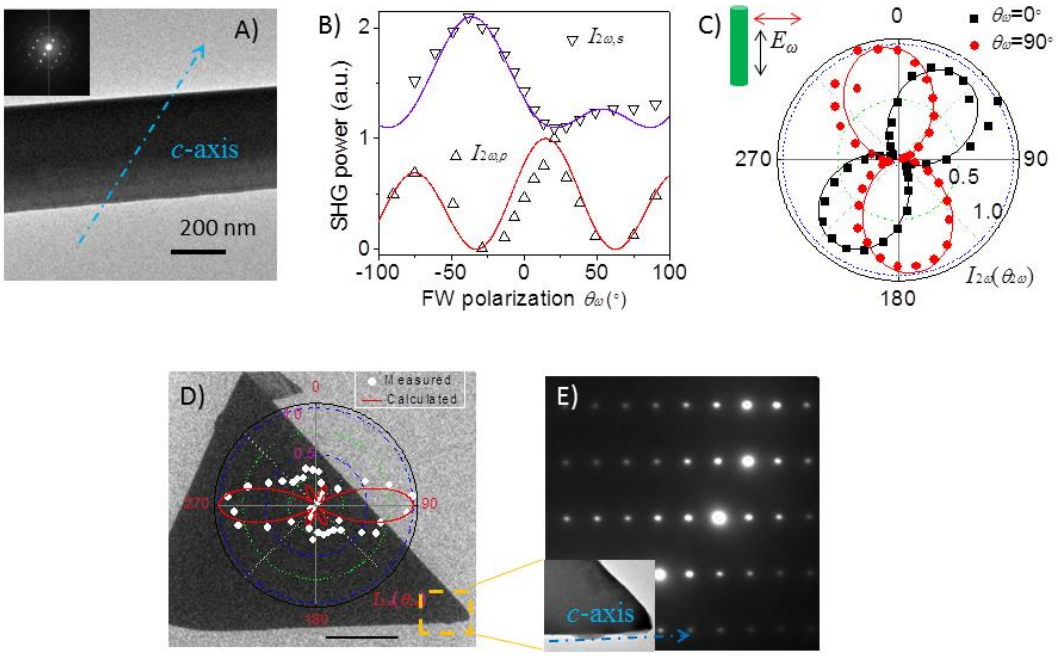

Figure A.3 Structural analysis of wurtzite CdS nanowire grown at an angle of 56° relative to the *c*-axis (*c*∠NW) and CdS nanoflake from optical SHG polarimetry. A) TEM micrograph of a selected CdS NW (*c*∠NW). Inset: SAED indicating WZ crystal structure and *c*∠NW growth orientation. B) TM- and TE-polarized SHG signal as a function of the excitation polarization angle. C) Polarimetric plot of total SHG intensity ($I_{2\omega}$) under TM (black, θ_ω=0°) and TE (red, θ_ω=90°) excitation. D) TEM micrograph of a CdS triangular nanoflake. Inset: polarimetric SHG pattern obtained from the nanoflake and fitted using Eq. 3, showing that the strongest SHG was polarized along the horizontal axis (bottom edge of the nanoflake). Scale bar: 2 μm. E) Selected area electron diffraction (SAED) of the CdS nanoflake, indicating the *c*-axis is along the bottom edge of the nanoflake. Inset depicting the bottom-right corner of the NF.

A.7 Arbitrary CdS Nanoflake

To demonstrate the utility of SHG polarimetry in crystallographic characterization of any single-crystalline WZ nanostructure with *c-axis* perpendicular to the propagation direction of the incident laser beam, a triangular nanoflake with no preferred growth orientation (unlike NWs), was selected (Figure A.3 D). The chosen nanoflake was large enough such that the in- and out- coupling efficiencies can be assumed to be 1. In such a WZ CdS nanoflake, the polarimetric SHG pattern should exhibit the strongest signal

when the excitation laser is polarized along the *c-axis* owing to the largest nonlinear coefficient d_{33}, which was confirmed by SHG results (inset of Figure A.3 D) and TEM experiments (Figure A.3 E). Therefore, SHG polarimetry can be utilized to determine in-plane *c-axis* orientation of a single-crystalline WZ material irrespective of its size and shape.

Besides structural analysis, anisotropy in SHG polarization can be utilized to determine fundamental material constants such as non-linear optical coefficients (d_{31}, d_{33} etc.), which can be perturbed by external stimuli, such as mechanical strain and electric field. For CdS, five large sized as-grown WZ NBs (> 2 μm wide), for which the *c*-axis was perpendicular to the long-axis of the NB and the in-coupling efficiency should be isotropic for any polarization angle, were tested. Similar to Figure A.2 B, TE-polarized SHG signal as a function of excitation polarization angle is plotted, and the average ratio of d_{31}/d_{33} ~-0.45 (±0.01) was extracted from the SHG dip, which matched the values reported in literature[23]. Similar analysis can be extended to determine d_{31}/d_{33} ratio for single crystals of other material compositions existing in WZ crystal structure (e.g. AgI, CdSe, ZnO, GaN, α-SiC etc.) thereby enabling the determination of material's anisotropic SHG response.

A.8 Determining Non-linear Optical Material Constants

Moreover, SHG polarimetry technique was extended to determine the size-dependent in-coupling coefficient of WZ NWs/NBs. In a tapered CdS WZ NB growing perpendicular to *c-axis*, TE-polarized SHG signal as a function of FW polarization differed in different regions owing to dissimilar size-dependent in-coupling efficiency

(Figure A.4 A). For example, in the narrowest region of the tapered NB (p1 ~150 nm, Figure A.4 A, inset), d_{31} is much larger than $\gamma^2_{\omega,in}\ d_{33}$ (Eq. S16) due to extremely small $\gamma^2_{\omega,in}$ and therefore, TE-polarized SHG signal exhibits $\cos^4\theta_\omega$ shape as a function of excitation polarization (similar to Figure A.1 D). However, as the width of the NB increases, i.e. as the incident spot is moved from p1 (~150 nm) to p2 (~200 nm) and then to p3 (~250 nm), the dip in the TE-polarized SHG signal shifts towards smaller angle (θ_ω). As the NB becomes wider, the SHG shape begins to resemble Figure A.2 B ($I_{2\omega,s}$). Combining the ratio of d_{31}/d_{33} extracted from CdS NBs and the shift in SHG intensity dip, the in-coupling efficiency as a function of the NB width was extracted as shown in Figure A.4 B. It is found that the in-coupling efficiency increases with the NB width approaching $\gamma^2_{\omega,in}$ ~1 for larger diameters. Knowledge of size dependent in-coupling efficiency is essential to carefully design high efficiency opto-electronic devices.

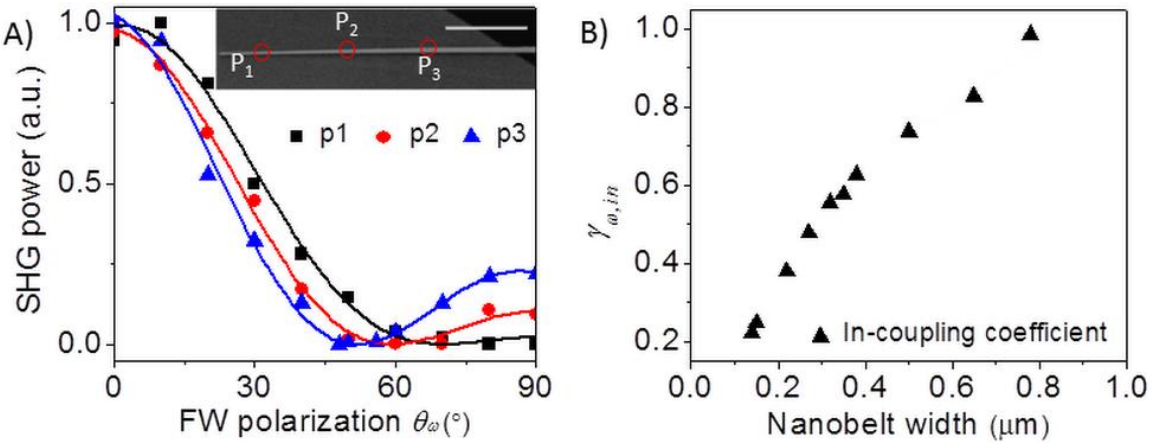

Figure A.4 Determination of nonlinear optical coefficients and in-coupling coefficient in wurtzite CdS nanobelts via optical SHG technique. A) TE-polarized SHG signal in a tapered CdS NB. Inset: SEM image of the NB indicating p1 (~150 nm), p2 (~200 nm) and p3 (~250 nm). B) In-coupling coefficient obtained as a function of NB width.

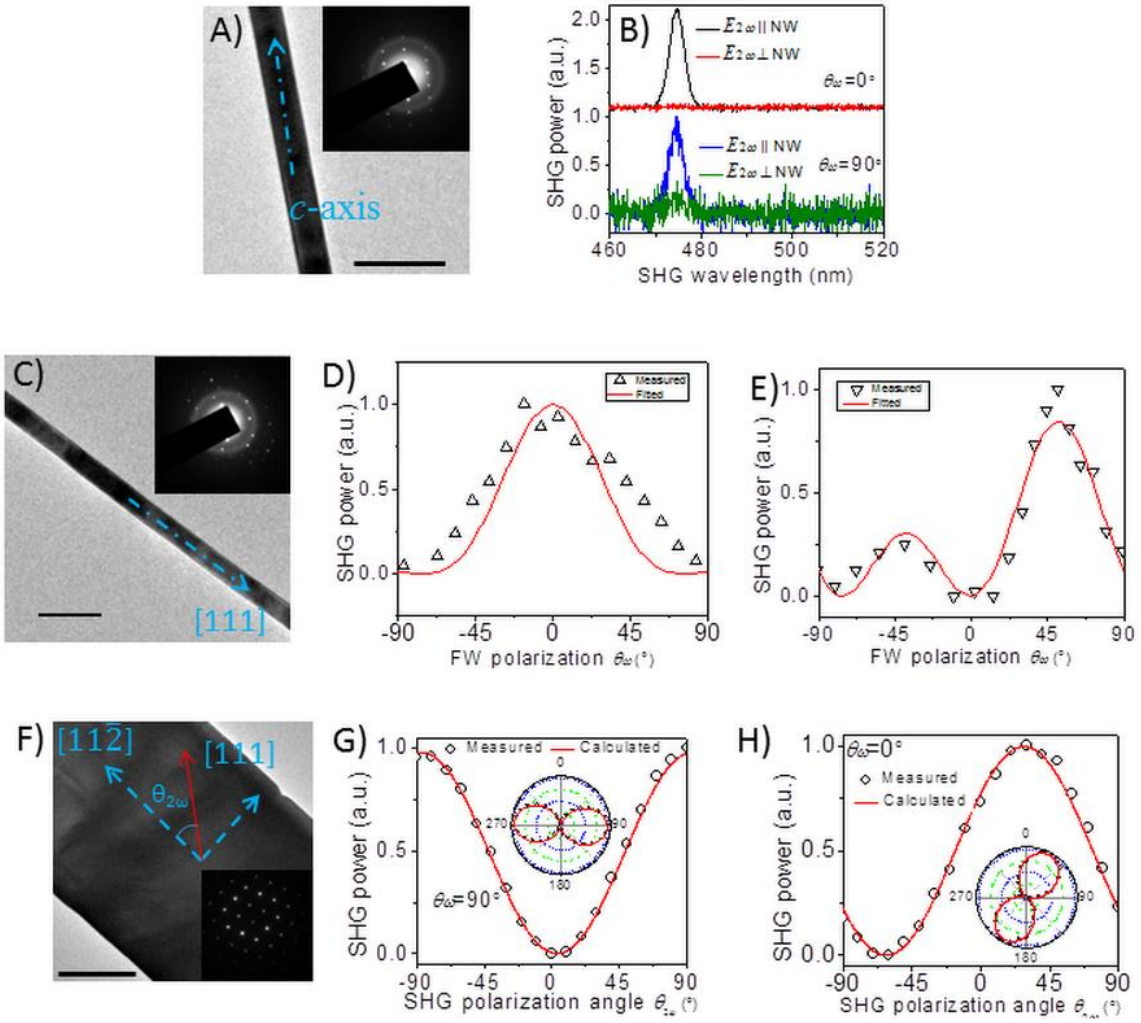

Figure A.5 Determination of crystal structure of wurtzite and zinc blende CdTe nanostructures using optical SHG polarimetry. A) TEM micrograph of a WZ CdTe NW grown along *c-axis*. Inset: SAED pattern indicating WZ crystal structure and *c-axis* growth orientation. Scale bar: 200 nm. **B)** SHG signal at two different excitation polarizations (TM and TE). **C)** TEM micrograph of a ZB CdTe NW grown along [111]. Inset: SAED pattern indicating ZB crystal structure and [111] growth orientation. Scale bar: 200 nm. **D) and E)** TM- and TE- polarized SHG as a function of excitation polarization angle (θ_ω), fitted (solid lines) using Eq. S25 for TM- and Eq. S26 for TE-polarized SHG signal. **F)** TEM micrograph of a ZB CdTe NB growing along [11$\bar{2}$]. Inset: SAED pattern indicating ZB crystal structure and 11$\bar{2}$ growth orientation. Scale bar: 1500 nm. **G)** and **H)** Polarimetric SHG signal under TE (θ_ω=90°) excitation (d), and under TM (θ_ω=0°) excitation (e).

A.9 Wurtzite CdTe Nanowire Growing Along *c*-axis

In order to show the ability of SHG technique to study different materials and distinguish between different crystal structures, CdTe NWs of WZ and ZB crystal structures were investigated. Similar to WZ CdS of *c*||NW (Figure A.1 D), SHG measurements carried out on WZ CdTe NW growing along the c-axis (Figure A.5 A) show that TM-polarized SHG is always dominant over TE-polarized SHG under both TM (θ_ω=0°) and TE (θ_ω=90°) excitation (Figure A.5 B). The weak signal observed for θ_ω = 90° was attributed to the poor in-coupling efficiency and small nonlinear coefficient (d_{31}). This experiment shows the applicability of SHG polarimetry technique towards single-crystalline WZ nanostructures irrespective of their chemical composition.

A.10 Zincblende CdTe Compared to Wurtzite CdS

ZB CdTe NW growing along [111] (Figure A.5 F) exhibits different SHG response as compared to a WZ CdS NW growing along *c-axis* (Figure A.1 B). WZ crystal structure's *c-axis* is equivalent to ZB's <111> since both directions are normal to the close packed plane of the crystal structure and therefore SHG response in ZB CdTe NB in Figure 5C can be compared with WZ CdS NW in Figure 1B to distinguish between the two crystal structures. TM-polarized SHG intensity in CdTe NW (Figure 5D) is much stronger under TM excitation as compared to TE excitation and follows $\cos^4\theta_\omega$ profile similar to the CdS NW (Figure A.1 D, $I_{2\omega,p}$). However, TE-polarized SHG intensity as a function of excitation polarization in CdTe NW (Figure A.5 E) is asymmetric with respect to NW's long axis and therefore differs from CdS NW (Figure A.1 D, $I_{2\omega,s}$) owing to crystal structure based anisotropy in ZB which is absent in WZ CdS[21]. The SHG

response shows a stronger peak at θ_ω ~54º corresponding to $[22\bar{1}]$ (resulting SHG is polarized along $[\bar{1}\bar{1}2]$ or TE polarized) as compared to the peak at θ_ω ~ -36º corresponding to $[114]$ (resulting SHG is polarized at an angle to $[\bar{1}\bar{1}2]$) as evident from Eq. S26). To further highlight the difference between SHG response in WZ and ZB nanostructures, ZB CdTe NB growing perpendicular to [111] (Figure A.5 F) was chosen and compared with WZ CdS NW growing perpendicular to *c-axis* (Figure A.2 A). When the excitation laser is polarized along [111] (θ_ω=90°, TE), the SHG signal is observed to be TE-polarized (also along [111]) (Figure A.5 G) (Eq. S27), similar to the case of WZ CdS (red curve in Figure A.2 C). However, as shown in Figure 5H, TM- and TE-polarized SHG signals are comparable under TM-excitation assuming perfect out-coupling efficiency ($\gamma_{2\omega,out}$ ~1) and the maximum SHG intensity is observed along $[22\bar{1}]$ (Eq. S28). This is different from the WZ CdS NB case where the SHG signal is polarized along the *c-axis* (TE-polarized in Figure A.2) irrespective of the incident polarization (Figure A.2 C). Therefore, distinct SHG response can help us distinguish between WZ and ZB crystal structures in single-crystalline materials and enables SHG polarimetry technique to characterize materials such as II-VI and III-V semiconductors that exist in both WZ and ZB crystal structures, which influences their physical properties to produce different responses[21,26,27].

A.11 Conclusion

In summary, optical SHG polarimetry was utilized to study crystallography of II-VI semiconductor nanostructures. The SHG response of nanostructures observed for different growth orientations and crystal structures (WZ and ZB) was intrinsically

associated with materials' nonlinear tensor and was analyzed to determine the crystallography of these nanomaterials, which also enabled us to differentiate between WZ and ZB crystal structures. Also, the technique allowed us to determine some materials' constants such as optical non-linear coefficients and size-dependent in-coupling coefficients. These techniques are promising to obtaining the crystal structures of nanostructure, especially on a device platform, which are not compatible with conventional TEM techniques in order to make a direct correlation between structure-property relationships, something that is critical yet still challenging in nanoscience.

A.12 References

1. Lu, W.; Lieber, C. M. Nat Mater 2007, 6, (11), 841-850.

2. Nam, S. W.; Chung, H. S.; Lo, Y. C.; Qi, L.; Li, J.; Lu, Y.; Johnson, A. T. C.; Jung, Y. W.; Nukala, P.; Agarwal, R. Science 2012, 336, (6088), 1561-1566.

3. Agarwal, R.; Barrelet, C. J.; Lieber, C. M. Nano Lett 2005, 5, (5), 917-920.

4. Cao, L. Y.; White, J. S.; Park, J. S.; Schuller, J. A.; Clemens, B. M.; Brongersma, M. L. Nat Mater 2009, 8, (8), 643-647.

5. Yan, R. X.; Gargas, D.; Yang, P. D. Nat Photonics 2009, 3, (10), 569-576.

6. Piccione, B.; Cho, C. H.; van Vugt, L. K.; Agarwal, R. Nat Nanotechnol 2012, 7, (10), 640-645.

7. Piccione, B.; Aspetti, C. O.; Cho, C. H.; Agarwal, R. Rep Prog Phys 2014, 77, (8).

8. Malard, L. M.; Alencar, T. V.; Barboza, A. P. M.; Mak, K. F.; de Paula, A. M. Phys Rev B 2013, 87, (20), 201401.

9. Kumar, N.; Najmaei, S.; Cui, Q. N.; Ceballos, F.; Ajayan, P. M.; Lou, J.; Zhao, H. Phys Rev B 2013, 87, (16), 161403.

10. Yin, X. B.; Ye, Z. L.; Chenet, D. A.; Ye, Y.; O'Brien, K.; Hone, J. C.; Zhang, X. Science 2014, 344, (6183), 488-490.

11. Sheng, Y.; Best, A.; Butt, H. J.; Krolikowski, W.; Arie, A.; Koynov, K. Opt Express 2010, 18, (16), 16539-16545.

12. Denev, S. A.; Lummen, T. T. A.; Barnes, E.; Kumar, A.; Gopalan, V. J Am Ceram Soc 2011, 94, (9), 2699-2727.

13. Johnson, J. C.; Yan, H. Q.; Schaller, R. D.; Petersen, P. B.; Yang, P. D.; Saykally, R. J. Nano Lett 2002, 2, (4), 279-283.

14. Long, J. P.; Simpkins, B. S.; Rowenhorst, D. J.; Pehrsson, P. E. Nano Lett 2007, 7, (3), 831-836.

15. Dutto, F.; Raillon, C.; Schenk, K.; Radenovic, A. Nano Lett 2011, 11, (6), 2517-2521.

16. Nah, S.; Kuo, Y. H.; Chen, F.; Park, J.; Sinclair, R.; Lindenberg, A. M. Nano Lett 2014, 14, (8), 4322-4327.

17. Liu, W. W.; Wang, K.; Liu, Z.; Shen, G. Z.; Lu, P. X. Nano Lett 2013, 13, (9), 4224-4229.

18. Ren, M. L.; Liu, W. J.; Aspetti, C. O.; Sun, L. X.; Agarwal, R. Nat Commun 2014, 5, 5432.

19. Hu, H.; Wang, K.; Long, H.; Liu, W.; Wang, B.; Lu, P. Nano Lett 2015, 15, (5), 3351-7.

20. Piccione, B.; van Vugt, L. K.; Agarwal, R. Nano Lett 2010, 10, (6), 2251-2256.

21. Agarwal, R.; Zakharov, D. N.; Krook, N. M.; Liu, W.; Berger, J. S.; Stach, E. A. Nano Lett 2015, 15, (5), 3303-8.

22. Thomas, D. G.; Hopfield, J. J. Phys Rev 1959, 116, (3), 573-582.

23. Boyd, R. W., Nonlinear optics. 3rd ed.; Academic Press: Burlington, MA, 2008.

24. Wang, J. F.; Gudiksen, M. S.; Duan, X. F.; Cui, Y.; Lieber, C. M. Science 2001, 293, (5534), 1455-1457.

25. Barzda, V.; Cisek, R.; Spencer, T. L.; Philipose, U.; Ruda, H. E.; Shik, A. Appl Phys Lett 2008, 92, (11), 113111.

26. Dick, K. A.; Caroff, P.; Bolinsson, J.; Messing, M. E.; Johansson, J.; Deppert, K.; Wallenberg, L. R.; Samuelson, L. Semicond Sci Tech 2010, 25, (2).

APPENDIX B: Nanotwin Detection and Domain Polarity Determination via Optical Second Harmonic Generation

Adapted and reprinted in parts from:

M.-L. Ren*, R. Agarwal*, P. Nukala, W. Liu and R. Agarwal, "Crystallographic Characterization of II-VI Semiconducting Nanostructures via Optical Second Harmonic Generation", Under preparation. * Equal Authorship

B.1 Introduction

Structure-property relationship is strongly determined by the nature of defects in a material, especially at the nanoscale. For example, defects such as dislocation pairs can enhance carrier collection for highly efficient CdTe solar cells[1]. Moreover, planar defects such as twin boundaries (TBs) and stacking faults (SFs), commonly found in II-VI and III-V semiconducting nanostructures of zincblende (ZB) and wurtzite (WZ) crystal structure grown by the vapor-liquid-solid (VLS) mechanism[2-7], have been observed to enhance cathodoluminescence (CL)[8] and enable efficient charge separation for solar hydrogen generation[9]. Therefore, detection and analysis of the nature of defects is of critical importance for efficient materials design. While established techniques such as diffraction and phase contrast transmission electron microscopy (TEM), and combinations of conductive atomic force microscopy (c-AFM) and piezo-force microscopy (PFM) are routinely used to characterize such extended defects such as dislocation pairs and twin boundaries, each of them suffer from certain limitations. For instance, conventional diffraction and phase contrast TEM techniques are limited in distinguishing between intensities of diffraction spots with opposite *k*-vectors owing to

Friedel's law which renders the Fourier transform of a crystal centrosymmetric[10-11]. This translates to a fundamental limitation of diffraction contrast TEM in not being able to detect the nature of the stacking TBs, upright or inverted, which can potentially show different carrier generation/separation behavior in the context of solar cell applications[12]. Optical second harmonic generation (SHG) polarimetry, which is sensitive to material crystallography in non-centrosymmetric materials[13-17], is capable of overcoming certain limitations of diffraction-contrast TEM, and reveal quantitative complimentary structural information. Here we adapt this technique in the polarimetry mode to study ZB CdTe nanostructures, which are known to contain both upright and inverted TBs, and show that SHG is not only capable of detecting TBs, which was verified via TEM, but can further quantitatively resolve the nature of the TBs (upright versus inverted), a task which is challenging to accomplish using any alternate single technique.

B.2 Theoretical expression of second harmonic generation (SHG) form ZB CdTe nanostructures

Considering the coordinate systems: the crystal axes ($\vec{e}_x\vec{e}_y\vec{e}_z$) and lab coordinate system ($\vec{e}_1\vec{e}_2\vec{e}_3$) (inset of Fig. 1a). Here $\vec{e}_x$=(1,0,0), $\vec{e}_y$=(0,1,0) and $\vec{e}_z$=(0,0,1). Assume $\vec{e}_2 = (a_x, a_y, a_z)$ depicts the long-axis of nanowires (NW) and nanobelts (NB), which is perpendicular to the zone axis or propagation direction of the excitation light with a unite wavevector $\vec{k} = (k_x, k_y, k_z)$ (considered as $\vec{e}_1$-direction). Then $\vec{e}_1 = \vec{k}$ and $\vec{e}_3 = (b_x, b_y, b_z) = \vec{e}_1 \times \vec{e}_2 = (a_z k_y - a_y k_z, a_x k_z - a_z k_x, a_y k_x - a_x k_y)$. Here $\sqrt{a_x^2 + a_y^2 + a_z^2} = 1$

and $\sqrt{k_x^2+k_y^2+k_z^2}=1$. The electric field, $\vec{E}_\omega=(E_{\omega,x},E_{\omega,y},E_{\omega,z})$, is in the $\vec{e}_2\vec{e}_3$ plane and has an angle of θ_0 with respect to $\vec{e}_2$,

$$\vec{E}_\omega = E_0\cos\theta_0\vec{e}_2+\gamma_{\omega,in}E_0\sin\theta_0\vec{e}_3, \tag{S1}$$

namely,

$$\begin{pmatrix}E_{\omega,x}\\E_{\omega,y}\\E_{\omega,z}\end{pmatrix}=E_0\begin{pmatrix}a_x\cos\theta_0+\gamma_{\omega,in}b_x\sin\theta_0\\a_y\cos\theta_0+\gamma_{\omega,in}b_y\sin\theta_0\\a_z\cos\theta_0+\gamma_{\omega,in}b_z\sin\theta_0\end{pmatrix}, \tag{S2}$$

where $\gamma_{\omega,in}=2/(1+\varepsilon_\omega)$, standing for the in-coupling coefficient of the electric field which is polarized perpendicularly to the nanowire. ε_ω indicates the dielectric constant of the nanowire (CdTe) at the frequency of ω. Therefore, the electric field of second harmonic generation (SHG) from zincblende CdTe (point group $4\bar{3}m$), $\vec{E}_{2\omega}=(E_{2\omega,x},E_{2\omega,y},E_{2\omega,z})$, can be described by the matrix[1],

$$\begin{pmatrix}E_{2\omega,x}\\E_{2\omega,y}\\E_{2\omega,z}\end{pmatrix}=\begin{pmatrix}0&0&0&d_{14}&0&0\\0&0&0&0&d_{14}&0\\0&0&0&0&0&d_{14}\end{pmatrix}\begin{pmatrix}E_{\omega,x}^2\\E_{\omega,y}^2\\E_{\omega,z}^2\\2E_{\omega,y}E_{\omega,z}\\2E_{\omega,z}E_{\omega,x}\\2E_{\omega,x}E_{\omega,y}\end{pmatrix}, \tag{S3}$$

Then we obtain the components of SHG which is parallel ($\vec{E}_{2\omega,p}$) or perpendicular ($\vec{E}_{2\omega,s}$) to the nanowire (or $\vec{e}_2$) is written as,

$$\vec{E}_{2\omega,p}=(\vec{E}_{2\omega}\cdot\vec{e}_2)\vec{e}_2=2d_{14}E_0^2[u_p\cos^2\theta_0+v_p\sin 2\theta_0+w_p\sin^2\theta_0]\vec{e}_2, \tag{S4}$$

$$\vec{E}_{2\omega,s}=(\vec{E}_{2\omega}\cdot\vec{e}_3)\vec{e}_3=\gamma_{2\omega,out}2d_{14}E_0^2[u_s\cos^2\theta_0+v_s\sin 2\theta_0+w_s\sin^2\theta_0]\vec{e}_3, \tag{S5}$$

where

$$\begin{pmatrix} u_p \\ v_p \\ w_p \end{pmatrix} = \begin{pmatrix} 3a_x a_y a_z \\ \gamma_{\omega,in}(a_z a_y b_x + a_x a_z b_y + a_y a_x b_z) \\ \gamma^2_{\omega,in}(a_x b_y b_z + a_y b_z b_x + a_z b_x b_y) \end{pmatrix}, \tag{S6}$$

$$\begin{pmatrix} u_s \\ v_s \\ w_s \end{pmatrix} = \begin{pmatrix} (a_z a_y b_x + a_x a_z b_y + a_y a_x b_z) \\ \gamma_{\omega,in}(a_x b_y b_z + a_y b_z b_x + a_z b_x b_y) \\ 3\gamma^2_{\omega,in} b_x b_y b_z \end{pmatrix} = \begin{pmatrix} v_p / \gamma_{\omega,in} \\ w_p / \gamma_{\omega,in} \\ 3\gamma^2_{\omega,in} b_x b_y b_z \end{pmatrix}. \tag{S7}$$

where $\gamma_{2\omega,out}$ depicts the out-coupling coefficient of the electric field which is polarized perpendicular to the nanowire. In nanobelts, the size is much larger than the excitation wavelength and then $\gamma_{2\omega,out} = \gamma_{2\omega,in} = \gamma_{\omega,in} = 1$. The intensity, having an angle of θ with respect to $\vec{e}_2$ in the $\vec{e}_2\vec{e}_3$ plane, is detected by

$$I_{2\omega}(\theta, \theta_0) = \left| \vec{E}_{2\omega,p} \cos\theta + \vec{E}_{2\omega,s} \sin\theta \right|^2. \tag{S8}$$

If considering $\vec{k} = (1, -1, 0)/\sqrt{2}$,

$$\begin{pmatrix} u_p \\ v_p \\ w_p \end{pmatrix} = \begin{pmatrix} 3a_x a_y a_z \\ \dfrac{\gamma_{\omega,in}}{\sqrt{2}}\{(a_x + a_y)(a_y a_x - a_z^2)\} \\ \dfrac{\gamma^2_{\omega,in}}{2} a_z [a_z + (a_x + a_y)][a_z - (a_x + a_y)] \end{pmatrix}, \tag{S9}$$

$$\begin{pmatrix} u_s \\ v_s \\ w_s \end{pmatrix} = \begin{pmatrix} v_p/\gamma_{\omega,in} \\ w_p/\gamma_{\omega,in} \\ \frac{3\gamma_{\omega,in}^2}{2\sqrt{2}} a_z^2 (a_x + a_y) \end{pmatrix}. \quad \text{(S10)}$$

Similar to the CdS case, we assume the long-axis ($\vec{e}_2$) has an angle of α_0 with respect to [001], therefore, $a_x = a_y = -\sin\alpha_0/\sqrt{2}$, $a_z = \cos\alpha_0$.

If $\alpha_0 = -54.74^\circ$, $\vec{e}_2 = (1,1,1)/\sqrt{3}$ and the long-axis is [111]. Then $a_x = a_y = a_z = 1/\sqrt{3}$, $\vec{e}_3 = (-1,-1,2)/\sqrt{6}$,

$$\begin{pmatrix} u_p \\ v_p \\ w_p \end{pmatrix} = \begin{pmatrix} \frac{1}{\sqrt{3}} \\ 0 \\ -\frac{1}{2\sqrt{3}}\gamma_{\omega,in}^2 \end{pmatrix} \text{ and } \begin{pmatrix} u_s \\ v_s \\ w_s \end{pmatrix} = \begin{pmatrix} 0 \\ -\frac{1}{2\sqrt{3}}\gamma_{\omega,in} \\ \frac{\gamma_{\omega,in}^2}{\sqrt{6}} \end{pmatrix}.$$

$$\vec{E}_{2\omega,p} = 2d_{14}E_0^2[\frac{1}{\sqrt{3}}\cos^2\theta_0 - \gamma_{\omega,in}^2\frac{1}{2\sqrt{3}}\sin^2\theta_0]\vec{e}_2, \quad \text{(S11)}$$

$$\begin{aligned} \vec{E}_{2\omega,s} &= \gamma_{2\omega,out}2d_{14}E_0^2[-\gamma_{\omega,in}\frac{1}{2\sqrt{3}}\sin 2\theta_0 + \gamma_{\omega,in}^2\frac{1}{\sqrt{6}}\sin^2\theta_0]\vec{e}_3 \\ &= \gamma_{2\omega,out}\gamma_{\omega,in}2d_{14}E_0^2\frac{1}{\sqrt{3}}\sqrt{\frac{2+\gamma_{\omega,in}^2}{2}}\sin\theta_0\sin(\theta_0-\beta)\vec{e}_3, \end{aligned} \quad \text{(S12)}$$

where $\cos\beta = \gamma_{\omega,in}/\sqrt{2+\gamma_{\omega,in}^2}$ and $\sin\beta = \sqrt{2/(2+\gamma_{\omega,in}^2)}$. If $\gamma_{2\omega,out} = 1$ in the large nanobelts, $\beta = \cos^{-1}\sqrt{1/3} = 54.74^\circ$, then $\vec{E}_{2\omega,s} = 0$ when $\theta_0 = \beta$, corresponding to [001]. If $\gamma_{2\omega,out} \to 0$ in the small nanowires, $\beta = 0^\circ$. If $\theta_0 = 0$, $\vec{E}_{2\omega,p} = \frac{2}{\sqrt{3}}d_{14}E_0^2\vec{e}_2$ and $\vec{E}_{2\omega,s} = 0$, while if $\theta_0 = 90^\circ$, $\vec{E}_{2\omega,p} = -\gamma_{\omega,in}^2\frac{1}{\sqrt{3}}d_{14}E_0^2\vec{e}_2$ and $\vec{E}_{2\omega,s} = \gamma_{2\omega,out}\gamma_{\omega,in}^2\frac{2}{\sqrt{6}}d_{14}E_0^2\vec{e}_3$, then

$$I_{2\omega}(\theta,\theta_0=0^\circ)=\left|\vec{E}_{2\omega,p}\cos\theta+\vec{E}_{2\omega,s}\sin\theta\right|^2\propto\cos^2\theta, \tag{S13}$$

$$I_{2\omega}(\theta,\theta_0=90^\circ)=\left|\vec{E}_{2\omega,p}\cos\theta+\vec{E}_{2\omega,s}\sin\theta\right|^2\propto\left|\cos\theta+x\sin\theta\right|^2\propto\cos^2(\theta-\delta), \tag{S14}$$

where $x=-\sqrt{2}\gamma_{2\omega,out}$, $\cos\delta=1/\sqrt{1+x^2}$ and $\sin\delta=x/\sqrt{1+x^2}$. It is seen that the output SHG signal reaches the maximum when $\theta_0=m\pi-\delta$ $(m=0,\pm1,\pm2,\cdots)$. If $\gamma_{2\omega,out}=1$ in the large nanobelts, $\delta=\cos^{-1}\sqrt{-2/3}=-54.74^\circ$. If $\gamma_{2\omega,out}\to0$ in the small nanowires, $\delta=0^\circ$.

If $\alpha_0=-125.26^\circ$, $\cos\alpha_0=-1/\sqrt{3}$, $\sin\alpha_0=-\sqrt{2}/\sqrt{3}$, $\vec{e}_2=(1,1,-1)/\sqrt{3}$ and the long-axis is $[11\bar{1}]$). Then $a_x=a_y=1/\sqrt{3}$, $a_z=-1/\sqrt{3}$, $\vec{e}_3=(1,1,2)/\sqrt{6}$,

$$\begin{pmatrix}u_p\\v_p\\w_p\end{pmatrix}=\begin{pmatrix}-\frac{1}{\sqrt{3}}\\0\\\frac{1}{2\sqrt{3}}\gamma_{\omega,in}^2\end{pmatrix}\text{ and }\begin{pmatrix}u_s\\v_s\\w_s\end{pmatrix}=\begin{pmatrix}0\\\frac{1}{2\sqrt{3}}\gamma_{\omega,in}\\\frac{\gamma_{\omega,in}^2}{\sqrt{6}}\end{pmatrix}.$$

$$\vec{E}_{2\omega,p}=2d_{14}E_0^2[-\frac{1}{\sqrt{3}}\cos^2\theta_0+\gamma_{\omega,in}^2\frac{1}{2\sqrt{3}}\sin^2\theta_0]\vec{e}_2, \tag{S15}$$

$$\begin{aligned}\vec{E}_{2\omega,s}&=\gamma_{2\omega,out}2d_{14}E_0^2[\gamma_{\omega,in}\frac{1}{2\sqrt{3}}\sin2\theta_0+\gamma_{\omega,in}^2\frac{1}{\sqrt{6}}\sin^2\theta_0]\vec{e}_3\\&=\gamma_{2\omega,out}\gamma_{\omega,in}2d_{14}E_0^2\frac{1}{\sqrt{3}}\sqrt{\frac{2+\gamma_{\omega,in}^2}{2}}\sin\theta_0\sin(\theta_0+\beta)\vec{e}_3,\end{aligned} \tag{S16}$$

where $\cos\beta=\gamma_{\omega,in}/\sqrt{2+\gamma_{\omega,in}^2}$ and $\sin\beta=\sqrt{2/(2+\gamma_{\omega,in}^2)}$. If $\gamma_{2\omega,out}=1$ in the large nanobelts, $\beta=\cos^{-1}\sqrt{1/3}=54.74^\circ$, then $\vec{E}_{2\omega,s}=0$ when $\theta_0=-\beta$, corresponding to $[00\bar{1}]$.

If $\gamma_{2\omega,out} \to 0$ in the small nanowires, $\beta = 0^\circ$. If $\theta_0 = 0$, $\vec{E}_{2\omega,p} = -\frac{2}{\sqrt{3}} d_{14} E_0^2 \vec{e}_2$ and $\vec{E}_{2\omega,s} = 0$, while if $\theta_0 = 90^\circ$, $\vec{E}_{2\omega,p} = \gamma_{\omega,in}^2 \frac{1}{\sqrt{3}} d_{14} E_0^2 \vec{e}_2$ and $\vec{E}_{2\omega,s} = \gamma_{2\omega,out} \gamma_{\omega,in}^2 \frac{2}{\sqrt{6}} d_{14} E_0^2 \vec{e}_3$, then

$$I_{2\omega}(\theta, \theta_0 = 0^\circ) = \left| \vec{E}_{2\omega,p} \cos\theta \right|^2 \propto \cos^2\theta, \tag{S17}$$

$$I_{2\omega}(\theta, \theta_0 = 90^\circ) = \left| \vec{E}_{2\omega,p} \cos\theta + \vec{E}_{2\omega,s} \sin\theta \right|^2 \propto \left| \cos\theta + x \sin\theta \right|^2 \propto \cos^2(\theta - \delta), \tag{S18}$$

where $x = \sqrt{2}\gamma_{2\omega,out}$, $\cos\delta = 1/\sqrt{1+x^2}$ and $\sin\delta = x/\sqrt{1+x^2}$. It is seen that the output SHG signal reaches the maximum when $\theta_0 = m\pi - \delta$ $(m = 0, \pm 1, \pm 2, \cdots)$. If $\gamma_{2\omega,out} = 1$ in the large nanobelts, $\delta = \cos^{-1}\sqrt{1/3} = 54.74^\circ$. If $\gamma_{2\omega,out} \to 0$ in the small nanowires, $\delta = 0^\circ$.

B.3 Nonlinear coefficient from different domains of CdTe

In the first section, SHG from CdTe is analyzed in the crystal axes ($\vec{e}_x \vec{e}_y \vec{e}_z$). We can also transfer the nonlinear tensor $\{\chi^{(2)}_{lmn}\}$ from the crystal axes to the lab axes ($\vec{e}_1 \vec{e}_2 \vec{e}_3$) by the rotation matrix, $R=\{R_{il}\}=\{\vec{e}_i \cdot \vec{e}_l\}$ (i=1, 2, 3; l=x, y, z), namely[6]

$$\chi^{(2)\dagger}_{ijk} = R_{il} R_{jm} R_{kn} \chi^{(2)}_{lmn}. \tag{S19}$$

Here $\{\chi^{(2)}_{lmn}\}$ corresponds to $\{d_{lm}\}$ of Eq.(S3) in Voigt notation. As defined above, $\vec{e}_1 = (1, -1, 0)$ is always the zone-axis ($[1\bar{1}0]$). In domain A$^+$, $\vec{e}_2 = (1,1,1)$ and $\vec{e}_3 = (-1, -1, 2)$, therefore the rotation matrix,

$$R=\begin{pmatrix} 1/\sqrt{2} & -1/\sqrt{2} & 0 \\ 1/\sqrt{3} & 1/\sqrt{3} & 1/\sqrt{3} \\ -1/\sqrt{6} & -1/\sqrt{6} & 2/\sqrt{6} \end{pmatrix}, \tag{S20}$$

then, $\{\chi_{ijk}^{(2)\dagger}\}$ can be obtained and expressed in Voigt notation $\chi_{lab}^{(2)}(+A)=\{d_{ij}^{\dagger}\}$,

$$\chi_{lab}^{(2)}(+A)=d_{14}\begin{pmatrix} 0 & 0 & 0 & 0 & -2/\sqrt{6} & -1/\sqrt{3} \\ -1/\sqrt{3} & 2/\sqrt{3} & -1/\sqrt{3} & 0 & 0 & 0 \\ -2/\sqrt{6} & 0 & 2/\sqrt{6} & -1/\sqrt{3} & 0 & 0 \end{pmatrix}. \tag{S21}$$

If rotating domain A^+ over 180° along $\vec{e}_1$, we will have domain A^- and therefore derive $\chi_{lab}^{(2)}(A^-)$ from $\chi_{lab}^{(2)}(A^+)$ by the rotation matrix,

$$R=\begin{pmatrix} 1 & 0 & 0 \\ 0 & -1 & 0 \\ 0 & 0 & -1 \end{pmatrix}, \tag{S22}$$

Then,

$$\chi_{lab}^{(2)}(A^-)=-\chi_{lab}^{(2)}(A^+). \tag{S23}$$

As defined above, domain B^+ has the lab axes of $\vec{e}_1=(1,-1,0)$ $\vec{e}_2=(-1,-1,1)$ and $\vec{e}_3=(-1,-1,-2)$, and exhibits the nonlinear tensor from that in the crystal axes ($\vec{e}_x\vec{e}_y\vec{e}_z$),

$$\chi_{lab}^{(2)}(+B)=d_{14}\begin{pmatrix} 0 & 0 & 0 & 0 & 2/\sqrt{6} & -1/\sqrt{3} \\ -1/\sqrt{3} & 2/\sqrt{3} & -1/\sqrt{3} & 0 & 0 & 0 \\ 2/\sqrt{6} & 0 & -2/\sqrt{6} & -1/\sqrt{3} & 0 & 0 \end{pmatrix}. \tag{S24}$$

In terms of rotation, domain B^+ can be obtained by rotating domain A^+ over -109° (anticlockwise) along $\vec{e}_1$ or over 180° relative to the $\vec{e}_2\vec{e}_3$ plane, which will give the same relation as Eq. (S24). Similarly domain B^- is the 71° rotation (clockwise) of domain A^+ or 180° rotation of domain B^+ along $\vec{e}_1$, then

$$\chi^{(2)}_{lab}(B^-) = -\chi^{(2)}_{lab}(B^+). \quad \text{(S25)}$$

Therefore in the lab axes ($\vec{e}_1\vec{e}_2\vec{e}_3$), under TE excitation, $\overrightarrow{E_\omega} = E_0\vec{e}_3$

$$\overrightarrow{E_{2\omega}}(A^+) = d_{14}E^2_\omega(-\frac{1}{\sqrt{3}}\vec{e}_2 + \frac{2}{\sqrt{6}}\vec{e}_3) = d_{14}E^2_\omega\chi^{(2)}_A$$

$$\overrightarrow{E_{2\omega}}(B^+) = d_{14}E^2_\omega(-\frac{1}{\sqrt{3}}\vec{e}_2 - \frac{2}{\sqrt{6}}\vec{e}_3) = d_{14}E^2_\omega\chi^{(2)}_B$$

$$\overrightarrow{E_{2\omega}}(B^-) = d_{14}E^2_\omega(\frac{1}{\sqrt{3}}\vec{e}_2 + \frac{2}{\sqrt{6}}\vec{e}_3) = d_{14}E^2_\omega(-\chi^{(2)}_B)$$

In this situation (TE excitation), domains A and B exhibit polar properties or polarities, which relate to the effective nonlinear coefficients $\chi^{(2)}_A$, $\chi^{(2)}_B$ and $-\chi^{(2)}_B$.

$$\chi^{(2)}_A = -\frac{1}{\sqrt{3}}\vec{e}_2 + \frac{2}{\sqrt{6}}\vec{e}_3, \text{ and } \chi^{(2)}_B = -\frac{1}{\sqrt{3}}\vec{e}_2 - \frac{2}{\sqrt{6}}\vec{e}_3 \quad \text{(S26)}$$

B.4 Description of Domains and Twin Boundaries

To understand the nature of upright and inverted TBs, we need to consider four different domains of ZB CdTe and their interface with each other. First domain or domain A^+ can be arbitrarily selected. Second domain, domain B^+ can be obtained by rotating domain A^+ by 109.35° along <110>. The intersection of domains A^+ and B^+ along the {111} is called an upright TB[12]. The two other two domains, A^- (or B^-) are the inversion of A^+ (or B^+) or a 180° rotation of A^+ (or B^+) along <110> (Figure B.1 A). Intersection of domains $A^+(A^-)$ and $B^-(B^+)$ along the {111} is called an inverted TB. Please note that an inverted TB is also an anti-phase boundary (APB) since the atoms across {111} are similar and are in principle forming "wrong-bonds"[12] (Figure B.1 A). Similarly, domains $A^+(B^+)$ and $A^-(B^-)$ can intersect along {111} to form an APB but not a

TB (Figure B.1 A). In order to interpret our SHG polarimetry data, consider the following coordinate system: assume domain A^+ with the lab axes of $\vec{e}_1 = (1,-1,0)$, $\vec{e}_2 = (1,1,1)$ and $\vec{e}_3 = (-1,-1,2)$, and domain B^+ with $\vec{e}_1 = (1,-1,0)$ $\vec{e}_2 = (-1,-1,1)$ and $\vec{e}_3 = (-1,-1,-2)$ (Figure B.1A. $\vec{e}_1$ is parallel to incident laser beam propagation direction. In a twinned nanostructure $\{AB\}_n$ (Figure B.1 B), parallel ($\vec{E}_{2\omega,p}$, θ=0°) or transverse magnetic (TM) components of SHG is expressed as (Eqs. S11 and S15),

$$\vec{E}_{2\omega,p} = 2E_0^2[(R_A + R_B)\frac{1}{\sqrt{3}}\cos^2\theta_0 - (R_A + R_B)\gamma_{\omega,in}^2\frac{1}{2\sqrt{3}}\sin^2\theta_0]\vec{e}_2, \quad (1)$$

and the perpendicular ($\vec{E}_{2\omega,s}$, θ=90°) or transverse electric (TE) components of SHG is (Eqs. S12 and S16),

$$\vec{E}_{2\omega,s} = \gamma_{2\omega,out}2E_0^2[-(R_A + R_B)\gamma_{\omega,in}\frac{1}{2\sqrt{3}}\sin 2\theta_0 + (R_A - R_B)\gamma_{\omega,in}^2\frac{1}{\sqrt{6}}\sin^2\theta_0]\vec{e}_3, \quad (2)$$

where $R_A = d_A V_A$ and $R_B = d_B V_B$, V_A (or V_B) is the interaction volume of single domain $A^{\pm}$ (or $B^{\pm}$) and $|d_{A,B}| = d_{14}$ is the second-order nonlinear coefficient of ZB CdTe, the polarization angle of fundamental wave (FW) (or SHG signal) is θ_0 (or θ) set with respect to $\vec{e}_2$, $\gamma_{\omega,in}$ stands for the in-coupling coefficient of FW at frequency ω, while $\gamma_{2\omega,out}$ stands for the out-coupling coefficient of SHG at frequency 2ω. Then the parallel and perpendicular intensity of SHG is, $I_{2\omega,p} = \left|\vec{E}_{2\omega,p}\right|^2$ and $I_{2\omega,s} = \left|\vec{E}_{2\omega,s}\right|^2$, and polarimetric SHG is described as,

$$I_{2\omega}(\theta,\theta_0) = \left|\vec{E}_{2\omega,p}\cos\theta + \vec{E}_{2\omega,s}\sin\theta\right|^2 \propto \left|\cos\theta + x\sin\theta\right|^2, \quad (3)$$

where x is the fitting parameter. $\vec{E}_{2\omega,p} = 2/\sqrt{3}(R_A + R_B)E_0^2\vec{e}_2$ and $\vec{E}_{2\omega,s} = 0$ under TM excitation ($\theta_0 = 0^\circ$), while $\vec{E}_{2\omega,p} = -1/\sqrt{3}(R_A + R_B)\gamma_{\omega,in}^2 E_0^2\vec{e}_2$ and $\vec{E}_{2\omega,s} = 2/\sqrt{6}\,\gamma_{2\omega,out}(R_A - R_B)\gamma_{\omega,in}^2 E_0^2\vec{e}_3$ under TE excitation ($\theta_0 = 90^\circ$). In the case of TE excitation ($\theta_0 = 90^\circ$), the fitting parameter is $x = \sqrt{2}\gamma_{2\omega,out}(R_B - R_A)/(R_B + R_A)$, therefore

$$R_A/R_B = (\sqrt{2}\gamma_{2\omega,out} - x)/(\sqrt{2}\gamma_{2\omega,out} + x), \tag{4}$$

which reveals domain information, such as polarity and volume fraction. If $R_A \approx R_B$, $|R_A - R_B| << |R_A + R_B|$ and then $x \to 0$, the TE-excited SHG will be TM-polarized ($I_{2\omega,s} << I_{2\omega,p}$). Also, this means that the material contains two domains of like sign, either A^+ and B^+ or A^- and B^- with comparable volume fractions. Therefore, there is only a possibility of upright TBs in such a material. However, if $R_A \approx -R_B$, $|R_A - R_B| >> |R_A + R_A|$ and $x \to \infty$, the TE-excited SHG will be TE-polarized ($I_{2\omega,s} >> I_{2\omega,p}$). This means that the material contains two domains of opposite signs, either A^+ and B^- or A^- and B^+ with comparable volume fractions and hence only inverted TBs can be present in the material. As discussed further in this work, most materials often consist of a mixture of all four domains and contain both upright and inverted TBs and therefore the observed SHG signal is in between the two cases described above.

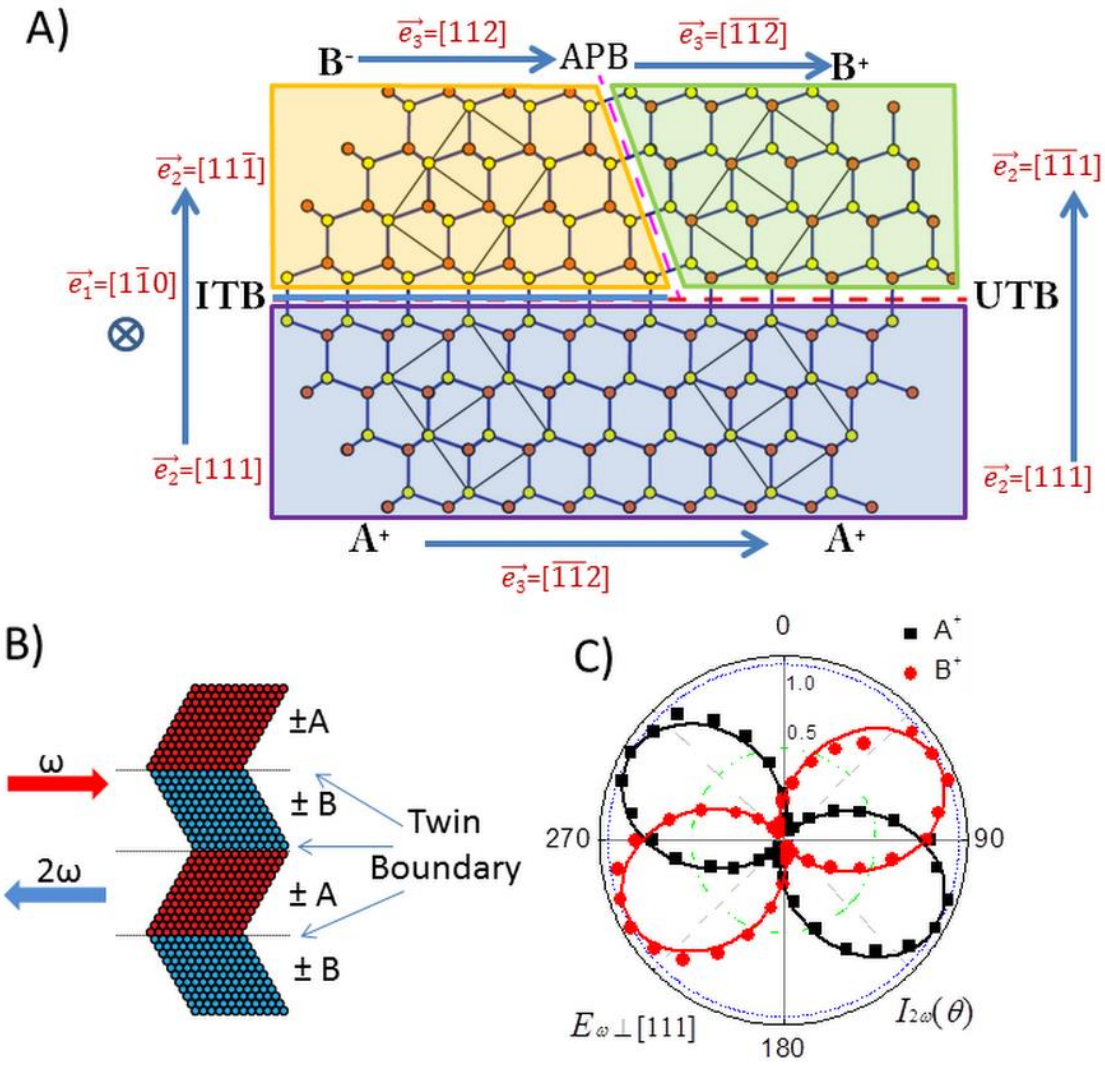

Figure B.1 A) Atomic model of twin boundaries (TB), upright TB (red dotted line) formed at the interface between A^+ (blue shaded region) and B^+ (green shaded region) and inverted twin boundary (ITB) (blue solid line) formed at the interface between A^+ and B^- (orange shaded region). B) Schematic of SHG polarimetry performed on a twinned CdTe nanostructure which is composed of domains A (or $A^{\pm}$) and B (or $B^{\pm}$). C) TE-excited SHG signal from domains A^+ and B^+ of a CdTe nanobelt (d~1500 nm).

B.5 Detection of Different Domains using SHG

In order to validate the efficacy of SHG polarimetry technique in detecting different type of domains, we started with the simple case of ZB CdTe nanostructures with single domain A ($A^{\pm}$) or B ($B^{\pm}$) without any TBs. The untwinned CdTe nanobelt

(NB) was first analyzed via TEM to ensure the absence of TBs and later through optical SHG polarimetry technique which has been well-established in our previous work (Appendix A). Under TE excitation, the SHG polarimetry measurements carried out on an untwinned CdTe NB (d~1500 nm) shows that TM- and TE-polarized SHG signals are comparable if the out-coupling efficiency is not considered ($\gamma_{2\omega,out}$ ~1) (Eqs. S11 and S12). The SHG signal is polarized in the second and fourth quadrants if the NB is illuminated from the top side ($\vec{k} = [1\bar{1}0]$), which corresponds to single domain defined as domain A^+ (Figure B.1 C). As previously mentioned, domain B^+ can be obtained by rotating domain A^+ by 109.5° counterclockwise along the $[1\bar{1}0]$ axis or by 180° along the [111] axis. Therefore, if the same NB was to be illuminated from the opposite direction ($\vec{k} = [\bar{1}10]$), then the NB should exhibit SHG polarimetry characteristics corresponding to domain B^+. When illuminated from the bottom (owing to the transparent SiN_x membrane on which the sample rests), the SHG signal is ploarized in the first and third quadrants, which is indeed a signature of domain B^+ (Figure B.1 C). Therefore, SHG polarimetry technique is capable of distinguishing between different domains (A and B) of CdTe, thus enabling the detection of planar defects such as TBs in nanostructures.

B.6 Detection and Analysis of Twin Boundaries in CdTe Nanobelt using SHG

Formation of TBs in ZB CdTe nanostructures, grown by Vapor-Liquid-Solid (VLS) mechanism, is attributed to low stacking fault energy (SFE) of this material and is believed to happen during the growth process itself[12]. Figure B.2 A is a bright field TEM micrograph (inset: dark field TEM micrograph) of one such twinned CdTe NB displaying distinct twin domains with varying contrast[10] in dissimilar volume fractions spread across

the entire NB. Twinning is also confirmed by the SAED pattern with superimposed diffraction spots from the two crystallographically distinct twin domains (A and B) (Fig. 2B). The domains A and B are stacked alternatively along <111>, forming the domain boundaries (or twin planes) along {111}. It is important to note that our TEM results reveal the presence of TBs but is unable to distinguish between upright and inverted TBs owing to inversion symmetry of the SAED pattern (Friedel's law). TM-excited SHG signal is TM-polarized (along $\vec{e}_2$), which is analogous to the untwinned CdTe NB (CdS reference). However, under TE excitation, the SHG signal generated from different regions of the NB is distinct. At an arbitrary point Q_1, the TE-excited SHG signal reaches the maximum at θ=160° (Figure B.2 C), similar to domain A^+, while it exhibits similar behavior as domain B^+ at another arbitrary point Q_2 and reaches the maximum at θ=41.82° (Figure B.2 D). More interestingly, The TE-excited SHG signal is almost polarized along $\vec{e}_2$ (θ=3.64°) at arbitrary point Q_3 (Figure B.2 E) while perpendicular to $\vec{e}_2$ (θ=74.55°) at arbitrary point Q_4 (Figure B.2 F).

In order to understand the observed phenomena, we assume domain A (or B) includes $A^{\pm}$ (or $B^{\pm}$) with second-order nonlinear coefficient of $\pm\chi_A^{(2)}$ (or $\pm\chi_B^{(2)}$), and any twinned CdTe NB is composed of all four domain types, $A^{\pm}$ and $B^{\pm}$. Therefore, ZB CdTe NBs can contain both upright and inverted TBs. According to our theoretical model, domain fractions and their relative polarity can be obtained by the formula $R_A/R_B = (\sqrt{2}-x)/(\sqrt{2}+x)$. We find $R_A/R_B = 1.68$ at Q_1 with x = – 0.36 and therefore A^+ (or A^-) seems to dominate over B^+ (or B^-). Similarly, $R_A/R_B = 0.21$ at Q_2 with x =

0.92, showing that B^+ (or B^-) dominates over A^+ (or A^-) . At Q_3, $x \approx 0$ and $R_A/R_B \approx 1$, leading to the equivalent fraction of B^+ (or B^-) and A^+ (or A^-). In contrast, $x = 3.57$ and $R_A/R_B = -0.43$ at Q_4, which indicates that domain B^+ (or B^-) dominates over domain A^- (or A^+). From this analysis of the SHG polarimetry data in different regions of CdTe NB, we can conclude that all four type of domains exist in twinned CdTe NBs simultaneously but in random volume fractions, as commonly observed in other materials[2,3]. Also, this indicates the presence of both upright as well as inverted TBs. In a NB, besides the VLS growth that occurs only in one dimension, vapor solid (VS) growth takes place at the lateral edges of the material during the entire duration. This is an epitaxial growth process where CdTe vapor condenses on spatially different locations along the belt as islands, grows along the lateral surface and eventually coalesce with each other. The growth rate of the above process is much faster and therefore there is a high probability of randomization in TB formation, i.e. both upright and inverted TBs can be formed simultaneously. In other words, the regions with distinct contrast in the TEM micrograph do not have to be uniform or periodic domains (Figure B.2 A) but can be a mixture of $A^{\pm}$ and $B^{\pm}$ domains. Therefore, these experiments have demonstrated the utility of SHG technique as a reliable source to detect and distinguish complex defects such as upright and inverted TBs irrespective of the nanotwin domain size, a task extremely difficult to achieve via conventional TEM techniques[5] and impossible via PFM owing to its low spatial resolution and need for low electrical conductivity samples[18].

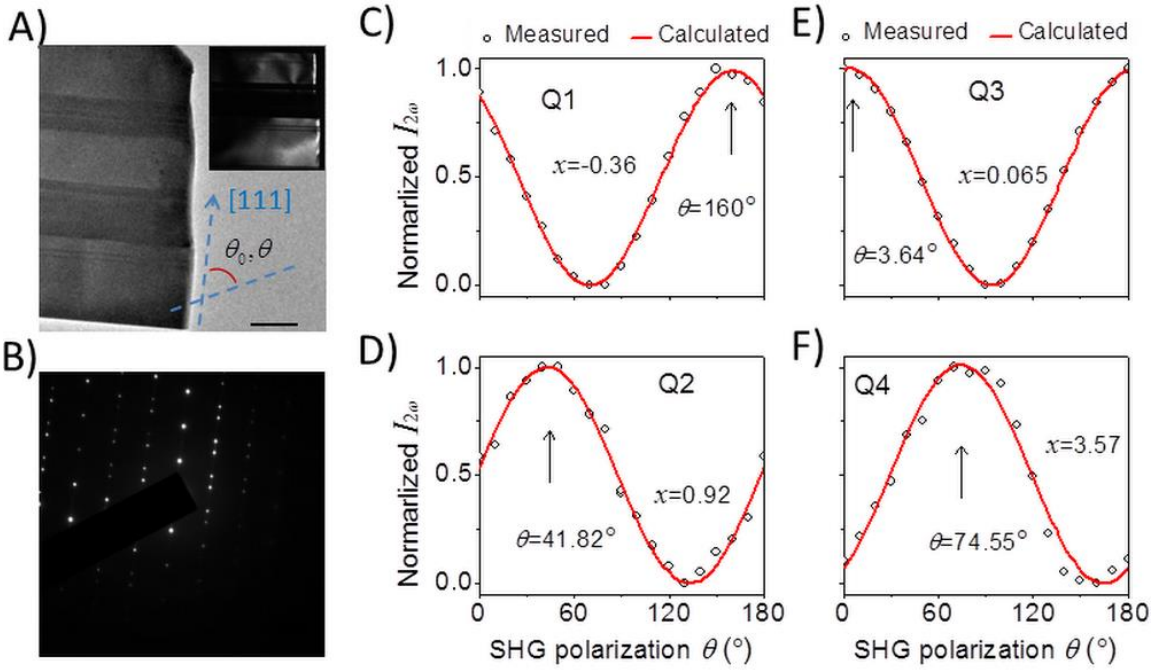

Figure B.2 Different response of TE-excited second harmonic generation (SHG) from different region of a twinned CdTe nanobelt. A) Bright field TEM micrograph of a twinned CdTe NB. Dark field TEM micrograph (inset) exhibits a non-uniform sized domain pattern. Scalar bar: 200 nm. B) SAED pattern confirming the twinned structure of the nanobelt. C)-F) SHG polarization plots of TE-excited SHG signal ($I_{2\omega}$) from different excitation regions of the CdTe NB.

B.7 Detection and Analysis of Twin Boundaries in CdTe Nanowire using SHG

In order to study the size effect of twinned nanostructures in resulting SHG signal, we performed measurements on CdTe nanowires (NWs) where the geometrical in-/out-coupling efficiency needs to be considered. A twinned NW (d~170 nm) possessing multiple periodic domains (A and B) was selected (Figure B.3 A) for comparison. In this NW, the SHG signal is TM-polarized under TM-excitation, similar to the ordinary CdTe NW which shows that TBs have little impact on the results under TM-excitation. However, under TE excitation (laser excitation polarized along the TB plane), the SHG signal is TE-polarized (Figure B.3 B). These results, considering our theoretical model,

indicate that the fitting parameter $x \to \infty$ or $R_A/R_B \approx -1$ (similar size but opposite polarity) in the twinned NW, which alludes towards the presence of only inverted rather than upright TBs. In fact, the twin domains in CdTe NWs are of uniform size (Figure B.3A). Therefore the TE-polarized components of SHG from adjacent domains are excited simultaneously and interfere constructively, while the TM-polarized components are opposite and cancel each other out, leading to dominant SHG polarized perpendicular to $\vec{e}_2$ (TE). In contrast to NBs, the NW formation is solely via VLS process and since there is only one nucleation event and subsequent steady state growth process via super saturated Au catalyst, one would expect uniform TBs of only one type across the entire length of the NW[6,7]. Formation of higher energy inverted TBs as opposed to lower energy upright TBs can be explained by periodic fluctuation of precursor concentration in the Au catalyst droplet thereby leading to formation of an APB, also a SF and hence an inverted TB, during growth.

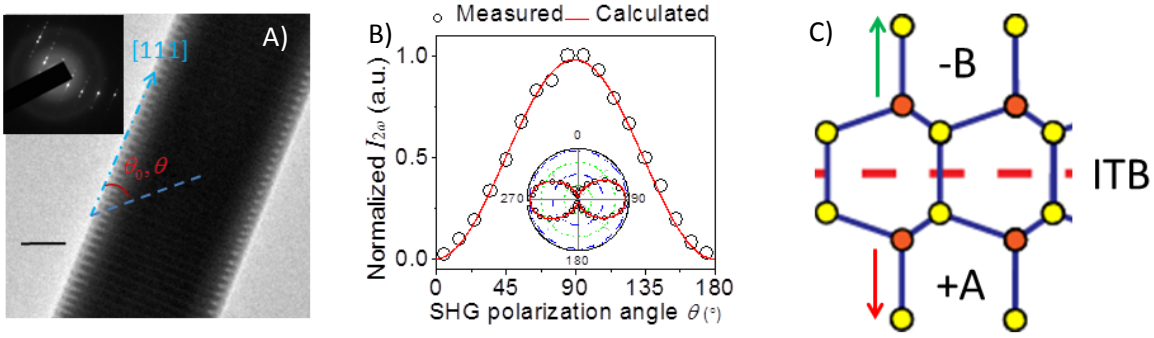

Figure B.3 Properties of second harmonic generation (SHG) from a twinned CdTe nanowire under TE excitation. A) Bright field TEM micrograph of a twinned NW (inset: SAWD). Scale bar: 50 nm. B) TE-excited SHG signal polarized perpendicular to the NW. C) Atomic model of polarization in domains across an inverted twin boundary (ITB). The parallel component (along [111]) is vanishing owning to the cancelation of domains A^+ and B^- along [111]. However in the perpendicular direction, they are constructively interfered and leading to the enhancement of perpendicular component.

B.8 Analysis of Twin Boundaries in CdTe Nanowire after Heat Treatment

To further explore the efficacy of SHG technique in detecting and differentiating between different type of TBs in smaller nanostructures, CdTe NW (same as Figure B.3) was analyzed after heat treatment which involved rapidly increasing the temperature up to 500°C in high vacuum (10^{-7} Torr), maintaining it at 500°C for ~ 10 minutes, followed by immediately cooling it down to room temperature. The purpose of this heat treatment process was to disturb the uniform nature of inverted TBs in the NW and to transform a fraction of TBs to upright TBs. As shown in Figure B.4 A, the image contrast owing to TBs is still very clear, however their nature is under question. Under TE excitation, this heat treated NW emits SHG signal which is observed to differ in different regions, very similar to the twinned NBs with random mutli-domains (Figure B.2). For example, TE-excited SHG exhibits a maximum at θ=5.45° (close to $\vec{e}_2$) at an arbitrary point P_1 (Figure B.4 B), at θ=68.69° at an arbitrary point P_2 (Figure B.4 D and at θ=127.27° at an arbitrary point P_3 (Figure B.4 D). This observed change in resulting SHG can be explained as follows. The twinned NW exhibits uniform domain pattern with only inverted TBs and becomes non-uniform (or random) after heat treatment owing to partial change in the nature of TBs from inverted to upright because of various factors such as vacancy condensation and dislocation motion. Sublimation of CdTe is also possible in the annealing process as evident from Figure B.4 A, which may also affect the SHG pattern. However, TE-excited SHG should still be TE-polarized like before (Figure B.3 B) after sublimation, assuming that domains A ($A^{\pm}$) and B ($B^{\pm}$) are sublimated equally. Therefore the significant changes of TE-excited SHG observed only after heat treatment could be

ascribed to the change in the nature of TBs and domain inversion in response to heat treatment[19].

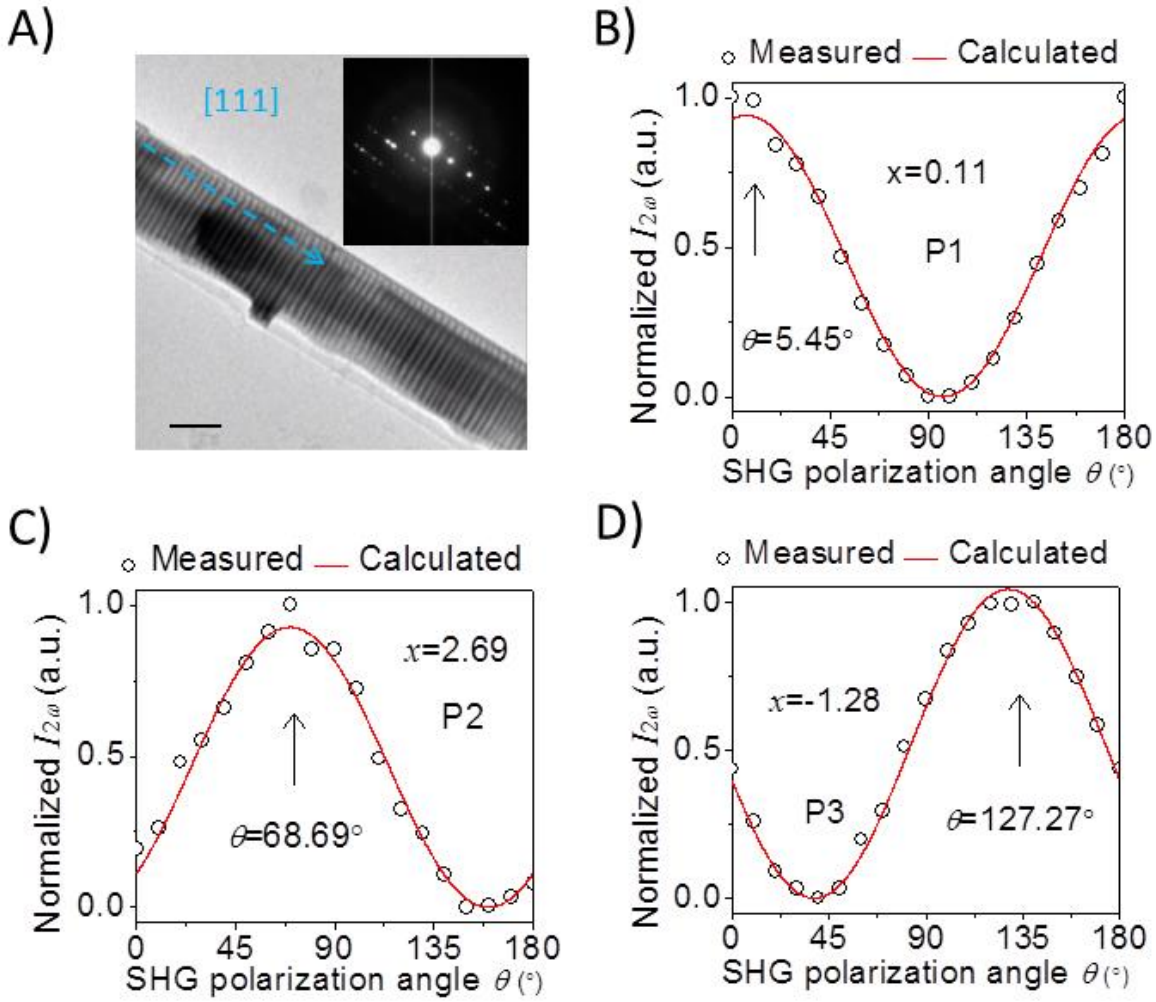

Figure B.4 Polarized SHG signal ($I_{2\omega}$) from the annealed nanowire (e.g. points P_1, P_2 and P_3) under TE excitation. A) Bright field TEM micrograph of twinned NW (same as Figure 3) after heat treatment (inset: SAED). Scale bar: 100 nm. B)-D) Three distinct TE-excited SHG polar plots in three different excitation regions (P_1, P_2 and P_3).

B.9 Conclusion

To summarize, optical SHG polarimetry technique has been demonstrated as a powerful and novel technique to detect and study the nature of planar defects such as upright and inverted TBs in ZB CdTe nanostructures, verified by TEM analysis of the

same samples. The technique can be extended to any non-centrosymmetric single crystalline material not only at the nanoscale but also for bulk materials which are impossible to characterize via TEM and to study the nature of defects in devices in-operando. The versatility and flexibility of this technique promises to improve our understanding in areas such as charge separation and carrier collection in semiconductors for efficient solar energy harvesting. For example, the present case study revealed that twinned CdTe NBs are made from randomly arranged multi-domains, containing both upright and inverted TBs, while a twinned CdTe NW exhibits uniform presence of periodic inverted TBs which may be transformed into a random multi-domain structure upon application of the necessary stimulus.

B.10 References

1. Li, C.; Wu, Y. L.; Pennycook, T. J.; Lupini, A. R.; Leonard, D. N.; Yin, W. J.; Paudel, N.; Al-Jassim, M.; Yan, Y. F.; Pennycook, S. J. Phys. Rev. Lett. 2013, 111, (9), 096403.

2. Li, Q.; Gong, X. G.; Wang, C. R.; Wang, J.; Ip, K.; Hark, S. Adv. Mater. 2004, 16, (16), 1436.

3. Hao, Y. F.; Meng, G. W.; Wang, Z. L.; Ye, C. H.; Zhang, L. D. Nano Lett. 2006, 6, (8), 1650.

4. Xiong, Q. H.; Wang, J.; Eklund, P. C. Nano Lett. 2006, 6, (12), 2736.

5. Johansson, J.; Karlsson, L. S.; Svensson, C. P. T.; Martensson, T.; Wacaser, B. A.; Deppert, K.; Samuelson, L.; Seifert, W. Nat. Mater. 2006, 5, (7), 574.

6. Algra, R. E.; Verheijen, M. A.; Borgstrom, M. T.; Feiner, L. F.; Immink, G.; van Enckevort, W. J. P.; Vlieg, E.; Bakkers, E. P. A. M. Nature 2008, 456, (7220), 369.

7. Caroff, P.; Dick, K. A.; Johansson, J.; Messing, M. E.; Deppert, K.; Samuelson, L. Nature Nano. 2009, 4, (1), 50.

8. Ohno, Y.; Yamamoto, N.; Shoda, K.; Takeda, S. Jpn J Appl Phys 2 2007, 46, (33-35), L830.

9. Liu, M. C.; Jing, D. W.; Zhou, Z. H.; Guo, L. J. Nat Commun 2013, 4, 2278.

10. Fultz, B.; Howe, J. M.; Louis A. Duhring Fund., Transmission electron microscopy and diffractometry of materials. 3rd ed.; Springer: Berlin ; New York, 2008; p xix.

11. Shiojiri, M.; Kaito, C.; Sekimoto, S.; Nakamura, N. Philos Mag A 1982, 46, (3), 495.

12. Holt, D. B. J. Phys. Chem. Solids 1969, 30, (6), 1297.

13. Sheng, Y.; Best, A.; Butt, H. J.; Krolikowski, W.; Arie, A.; Koynov, K. Opt. Express 2010, 18, (16), 16539.

14. Malard, L. M.; Alencar, T. V.; Barboza, A. P. M.; Mak, K. F.; de Paula, A. M. Phys Rev B 2013, 87, (20), 201401.

15. Kumar, N.; Najmaei, S.; Cui, Q. N.; Ceballos, F.; Ajayan, P. M.; Lou, J.; Zhao, H. Phys Rev B 2013, 87, (16), 161403.

16. Yin, X. B.; Ye, Z. L.; Chenet, D. A.; Ye, Y.; O'Brien, K.; Hone, J. C.; Zhang, X. Science 2014, 344, (6183), 488.

17. Hu, H.; Wang, K.; Long, H.; Liu, W.; Wang, B.; Lu, P. Nano Lett 2015, 15, (5), 3351.

18. Kalinin, S. V.; Jesse, S.; Rodriguez, B. J.; Shin, J.; Baddorf, A. P.; Lee, H. N.; Borisevich, A.; Pennycook, S. J. Nanotechnology 2006, 17, (14), 3400.

19. Nakamura, K.; Ando, H.; Shimizu, H. Appl. Phys. Lett. 1987, 50, (20), 1413.

APPENDIX C: Observing Oxygen Vacancy Dynamics Indirectly during Electroforming via Platinum Migration

Adapted and reprinted in parts from:

M.H. Jang*, R. Agarwal*, P. Nukala, D. Choi, A.T.C. Johnson, I-W. Chen and R. Agarwal, "Observing Oxygen Vacancy Dynamics Indirectly during Electroforming via Platinum Migration", Under review at ACS Nano Letters. *Equal Authorship

C.1 Introduction

Resistive memory devices that can be switched between low and high resistance states (LRS and HRS) by the application of electrical pulses are being extensively investigated as promising candidates for next-generation non-volatile memory systems and also as an artificial synapse material for applications in neuromorphic computing[1-15]. A typical resistive memory device consists of an active material sandwiched between two metal electrodes, which can be configured in crossbar architecture for random access memory. A variety of active materials such as transition metal oxides (TMOs), solid-state electrolytes, perovskites and organic materials that can be reversibly switched between different resistance states have been studied[1-6]. Among these candidates, TMOs (e.g., TiO_2, Ta_2O_5, NiO) have distinct advantages owing to their high temperature stability, ease of film deposition and compatibility with conventional semiconductor fabrication processes with sub 10-nanometer scale feature size[5-12]. For any resistive memory device, the preliminary step before practical operation is the process of electroforming which enables the as-deposited HRS to switch into a LRS upon the application of an electrical

bias. Electroforming process is believed to be due to the formation of a low resistance filament in a high resistance active material matrix[15], which can then be reversibly disrupted or reformed with *d.c.* or pulsed electrical bias to access different resistance states. Therefore, given the significance of the electroforming process in device operation, it is critical that the underlying physical mechanism is properly understood. One broadly accepted hypothesis explaining the electroforming process in TMOs is the migration and accumulation of oxygen vacancies under electric field leading to formation of localized regions with an off-stoichiometric, oxygen-deficient conductive phase, such as the *Magnéli* phase (Ti_nO_{2n-1})[6-10]. Kwon et al.[10] observed the *Magnéli* phase (Ti_4O_7) in electroformed Pt/TiO_2/Pt stacked structure via ex situ TEM experiments, where the samples were prepared by cross-sectioning the device post-electroforming via focused ion-beam (FIB), which may alter the state of the device. Even though extensively studied, a direct observation of the electroforming process in TMO based memory devices is lacking thus far owing to challenges in device fabrication and observing the phenomenon in situ while in operation. It must be realized that directly tracking the dynamics of point defects such as oxygen vacancies in real-time during the electroforming process is extremely challenging using electron microscopy techniques, further complicated due to the polycrystalline or even amorphous nature of the films typical of TMO-based devices. Given these challenges, it would be helpful if the unique properties of the oxygen deficient phase can itself be utilized to observe oxygen vacancy motion under an electrical bias in a direct manner to verify oxygen vacancy's role in resistive switching.

C.2 Strong Metal Support Interaction

It is well known in catalysis that certain noble metals (e.g., Pt, Pd or Au) display enhanced surface interaction with partially reduced TMOs owing to charge transfer from the d-orbital of the reduced cation of the TMO to the metal atom leading to an ionic interaction, which alters the catalytic properties of the noble metal[16-20]. This interaction, known as strong metal-support interaction (SMSI), is only applicable to TMOs where the transition metal cation can exhibit multiple oxidation states. The cation in the vicinity of oxygen vacancies in TMO is reduced (e.g. Ti^{4+} in TiO_2 becomes Ti^{3+}), thus triggering SMSI between the reduced cation and the noble metal atom. Therefore, the SMSI character of a TMO can be strongly enhanced by increasing the oxygen vacancy concentration and has been extensively studied in the Pt-TiO_2 system[18-20]. In this work, we have enabled the detection of oxygen-vacancy-rich TMO regions via their increased Pt concentration established by Pt migration driven by enhanced Pt-TiO_2 SMSI. By designing thin Pt contacts (10-15 nm), we show that Pt can act as a tracer for the oxygen deficient phase and hence can be easily detected via microscopy, thereby providing evidence of the role of oxygen vacancy dynamics during the electroforming process in TMO-based resistive memory devices. The purpose of Pt migration and filament formation in this work is to directly probe the oxygen vacancy migration and accumulation driven electroforming mechanism and not to create metal filament based resistive memory devices[4,13] which can be reversibly switched between LRS and HRS.

C.3 Device Fabrication and Characterization

In order to optimize SMSI in our system and to observe the formation of conductive filament by high-resolution transmission electron microscopy (TEM), nanoscale lateral Pt/TiO_2/Pt devices were fabricated on thin (<50 nm) electron beam transparent SiN_x membranes such that Pt electrodes are stacked between SiN_x and TiO_2 film (Fig. C.2 A). Double side polished SiN(300 nm)/Si(525 μm)/SiN(300 nm) wafers were etched to form SiN membrane window by KOH. After opening the SiN membrane windows, substrates were spin-coated with a 100 nm thick PMMA (A2 950 single layer) to lithographically define Pt electrode nanogap patterns via electron beam lithography (Elionix ELS-7500). After developing, 10-20 nm thick Pt layer was deposited by sputtering. TiO_2 thin films (~10-15 nm) were then deposited by atomic layer deposition (ALD) using Tetrakis(dimethylamido)titanium (TDMAT) and H_2O precursors at 250^oC. The samples were then annealed at 300^oC without breaking the vacuum to crystallize TiO_2 films in an inert atmosphere. For fabrication of Pt/SiO_2/Pt device, we deposited SiO_2 by plasma enhanced chemical vapor deposition (PECVD). The chemical composition of TiO_2 thin film before and after annealing was measured by X-ray photoelectron spectroscopy (XPS). In Fig. C.1 (a) and (b), XPS O 1*s* raw and fitted spectra before and after the annealing treatment are shown with deconvoluted sub-peaks. O signals from -OH bonds and H_2O are almost gone after annealing. This indicates that TiO_2 film is reduced and has more hydrophobicity on account of losing the hydroxyl group attached to the Ti atoms. This hydrophobicity of TiO_2 films after annealing is also confirmed by the contact angle measurements of the as-grown TiO_2 film with 16.7º (Fig.

C.1 c) and of the annealed TiO_2 with 54.3° (Fig. C.1 d). Selective area electron diffraction (SAED) performed on TiO_2 film after an annealing treatment (Fig. C.1 e) confirms the presence of only anatase crystalline phase.

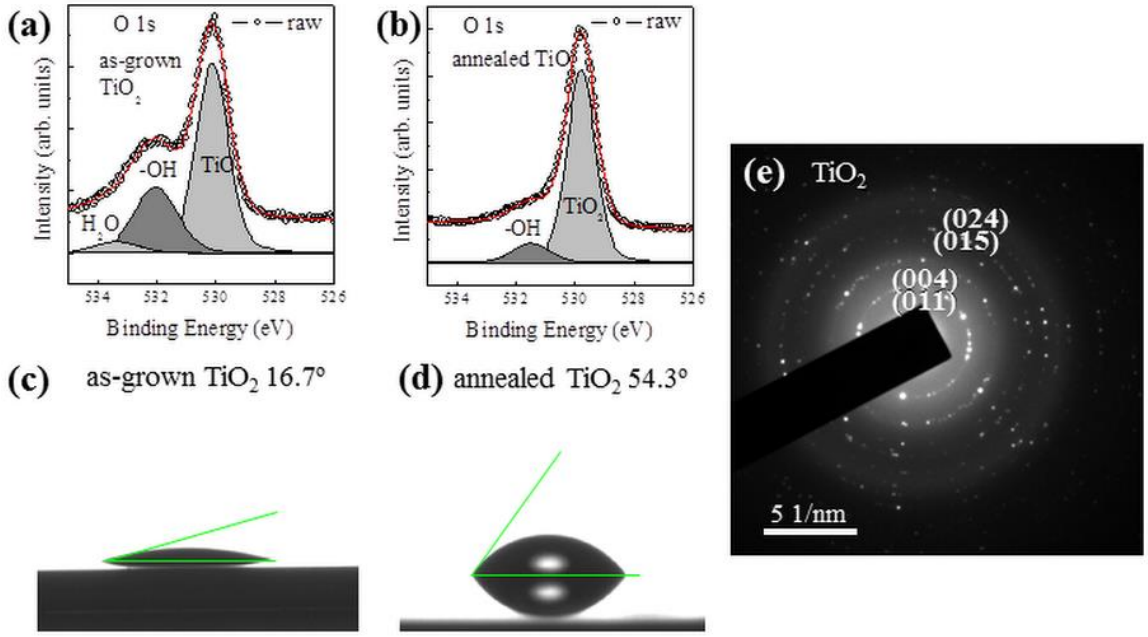

Figure C.1 Characterization of ALD deposited TiO_2 film before and after annealing (a) XPS O 1s spectra of the as-grown TiO_2 film. Open circles and the red line indicate the raw data and the fitted data, respectively. Deconvoluted sub peaks which are assigned as TiO_2, OH and H_2O are shown underneath the spectra. (b) XPS O 1s spectra of annealed TiO_2 film. Open circles and the red line indicate the raw data and the fitted data, respectively. TiO_2 and OH peaks are assigned. (c) Contact angle measurement of as-grown TiO_2 film showing a contact angle of 16.7° (d) Contact angle measurement of annealed TiO_2 film showing a contact angle of 54.3°. TiO_2 becomes more hydrophobic after annealing treatment in inert atmosphere. (e) SAED pattern of TiO_2 film after annealing treatment in an inert atmosphere confirming the presence of TiO_2 in anatase crystal structure (Space group: $I4_1/amd$).

This TEM compatible lateral device platform eliminates the need of disruptive FIB based techniques for cross-sectioning the sample, which is known to cause device degradation through Ga^+ implantation and carbon deposition. A lateral device configuration also ensures uniform exposure of all device components to its environment, which eliminates stacking sequence dependent electroforming properties[8]. In our study,

Pt was chosen as the electrode material for a variety of reasons: it is known to exhibit strong SMSI behavior with TiO_2, is considered an "inert" electrode material with a high melting point (2040 K). Furthermore, ultra-thin (10-20 nm) Pt electrodes and TiO_2 layer ensures maximum surface interaction between the two materials, thereby enhancing SMSI and easing the detachment process of Pt from the parent electrode to track the oxygen deficient phase during electroforming.

C.4 Electroforming in Pt/TiO_2/Pt Device

The electroforming process of one such lateral Pt/TiO2/Pt device (~40 nm gap between the metal electrodes, Fig. C.2 b) performed under ambient conditions (outside the microscope) during the I-V sweep with a low compliance current of 30 µA occurs at a voltage (Vf) <10 V (Fig. C.2 d, red circles). Post electroforming, the current flowing through the device in LRS increased by ~500 times (Fig. C.2 (d), black circles) in comparison to the virgin device in HRS at 1 V. Interestingly, the scanning electron microscopy (SEM) image of the electroformed device (Fig. C.2 c) shows a continuous filament between Pt electrodes along with some shrinkage at the anode, which suggests that the metal from the anode possibly participated in the conductive filament formation. To further understand the chemical composition and structure of the conductive filament, the device was characterized via TEM [21,22] further confirming (Fig. C.2 e, f) a continuous Pt filament from the anode to the cathode. Energy filtered TEM (EFTEM) mapping of the nanogap region using Pt O-edge confirms the presence of Pt atoms in the filament.

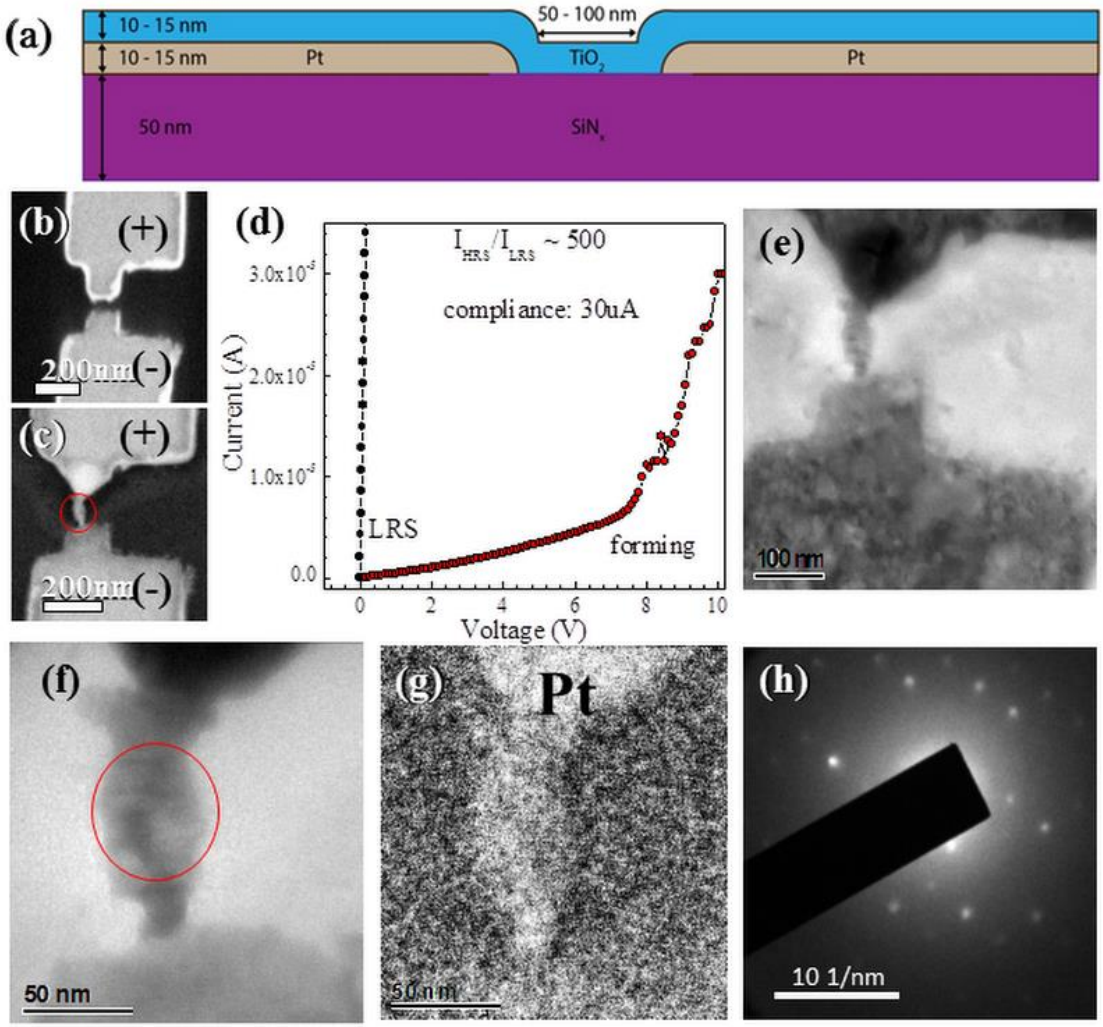

Figure C.2 Characterization of a lateral Pt/TiO2/Pt device before and after the electroforming process in ambient conditions (a) Schematic of a lateral nanogap Pt/TiO2/Pt device with Pt electrodes stacked between SiNx membrane and TiO2 film. (b) SEM image of a nanogap Pt/TiO2/Pt device prior to TiO2 deposition. (c) SEM image of the Pt/TiO2/Pt device after electroforming. The electrode polarity is indicated by '+' (anode) and '-' (cathode). Brighter region corresponds to higher atomic number material. (d) I-V characteristic curves during electroforming (red filled circles) and after electroforming (black filled circles) in Pt/TiO2/Pt device at the compliance current of 30 μA. (e) TEM image of Pt/TiO2/Pt device after forming. (f) Magnified TEM micrograph of the conductive filament. (g) Pt O-edge EFTEM map of the nanogap region showing a continuous Pt filament across the electrodes. (h) Nano-beam diffraction (NBD) pattern of conductive filament (region inside the circle in Fig. 1 (f)) shows pure-Pt face-centered cubic phase.

Nanobeam electron diffraction (NBD) obtained from the central part of the filament (Fig C.2 e, red circle) also corresponds to Pt metal in face centered cubic structure (Fig. 1h) (space group: $Fm\bar{3}m$ and a = 3.92 Å). These observations demonstrate that in our device design, the conductive filament, whose formation is responsible for the electroforming event, is made of metallic Pt, the source of which appears to be the Pt from the anode.

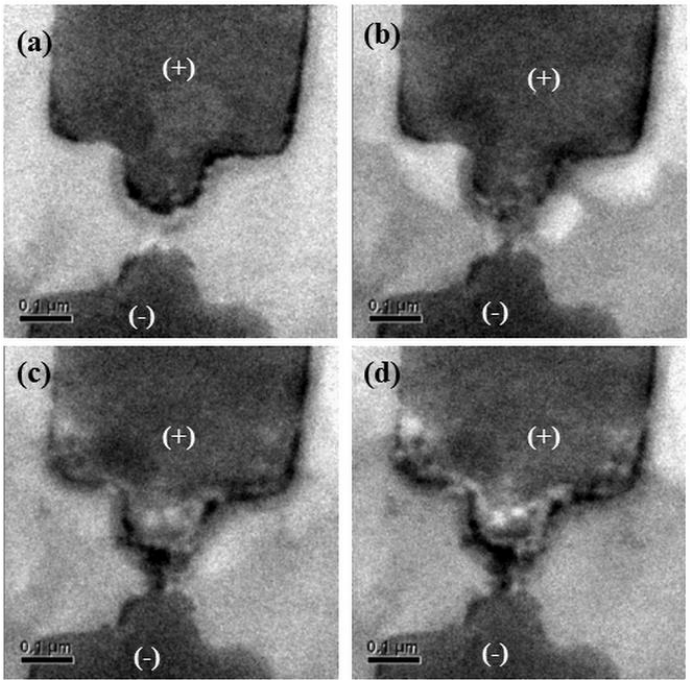

Figure C.3 Snapshots from the movie S1 showing in situ BF-TEM observation of electroforming process in a lateral Pt/TiO2/Pt device. (a) The virgin device before applying bias, (b) Initiation of the conductive filament formation along with O2 bubble formation near the anode (lighter contrast). (c) Complete filament formation (d) The electroformed device after the electrical bias was removed.

C.5 In-situ TEM Electroforming in Pt/TiO_2/Pt Device

It is surprising that a noble metal such as Pt can participate in the filament formation during the electroforming process since it is believed to be chemically inert[14]. To further validate these results and observe the electroforming behavior in real-time, another lateral Pt/TiO_2/Pt device was electrically biased on our in situ TEM compatible

platform under high vacuum (~10^{-7} Torr) while simultaneously recording a movie (Fig. C.3). During the experiment, we clearly observed a gradual migration of Pt from the anode towards the cathode leading to the formation of a continuously connected path along with development of lighter contrast near the anode suggestive of O_2 gas bubble formation and eventual dissipation[9] (Fig. C.3 a-d). The directionality of Pt motion from the anode to the cathode shows that metal migration is polarity dependent and not due to heat related effects. These in situ observations are similar to the ex situ results described earlier, which also suggests that effects due to electron beam exposure are not significant.

C.6 Electroforming in Pt/SiO_2/Pt Device

Recently Yang and coworkers[23] observed the motion of nanoscale metal inclusions, including Pt, embedded in an insulating SiO_2 matrix under large electrical bias towards the cathode, which they explained through polarization of metallic nanoparticles and their subsequent motion under sufficiently large electric field. However, for the case of Pt nanoparticles, the motion was much more difficult requiring very high fields (>5 MV/cm) to move them over very small distances (~5 nm), which they attributed to poor polarizability of Pt. In comparison, in our system, the Pt electrode can release Pt at lower electric field intensities (<3 MV/cm) to migrate over much larger distances (50-100 nm) in sufficient quantity so as to form a continuous bridge across the metal electrodes[23], suggesting a completely different mechanism. To compare with Pt/TiO_2/Pt system, we also fabricated Pt/SiO_2/Pt lateral devices. The non-TMO (SiO_2), incapable of displaying SMSI with Pt, switched to LRS accompanied by severe electrode disfigurement at an extremely high electric field strength of ~28 MV/cm (Fig. C.4 a-c), possibly due to

dielectric breakdown of SiO_2[24]. Another experiment performed with a device architecture of the type Pt/SiN_x/Pt (Fig. C.5) with a nitride matrix between the Pt electrodes did not show any Pt migration or electroforming at ~5 MV/cm. These results confirm that transition metal cations and oxygen anions are necessary for observing the enhanced migration of Pt in response to an applied electric field, which is consistent with the SMSI mechanism.

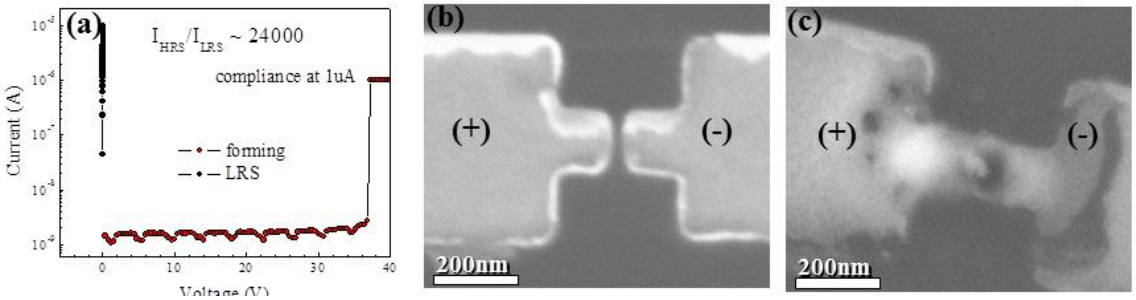

Figure C.4 Electroforming process in a lateral Pt/SiO2/Pt device (a) I-V characteristic curves of Pt/SiO2/Pt device during electroforming (red circles) and after electroforming (black circles). The forming voltage is ~ 37 V with the compliance current set at 1 μA. (b) SEM image of the Pt gap before SiO2 deposition. (c) SEM image after the electroforming process showing severely disfigured electrodes due to high fields.

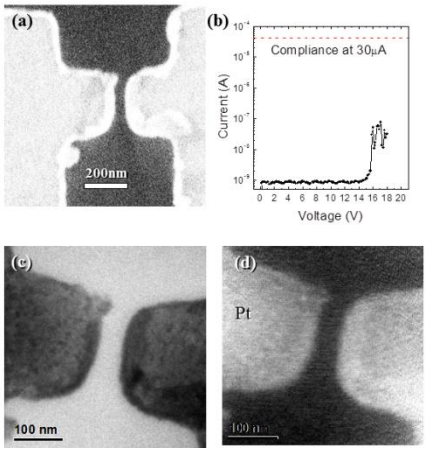

Figure C.5 Characterization of Pt/SiN_x/Pt nanogap device (a) SEM image of a 30 nm Pt nanogap region on SiN_x membrane with no TiO_2 film deposited on top of the electrodes. (b) I-V characteristic curve of the device for an applied bias up to 18 V (~5 MV/cm) showing no electroforming event. The current value is two orders of magnitude below the set compliance level. (c) TEM image of the nanogap region after applying electrical bias shows no Pt motion from either electrode (d) Pt-O edge EFTEM image of the nanogap region confirming no Pt motion or filament formation in the device.

C.7 Atmosphere Dependent Electroforming in $Pt/TiO_2/Pt$ Devices

Since the SMSI character of a TMO is strongly dependent on the oxygen vacancy concentration, one is able to tune SMSI by way of environmental conditions[16-20]. For example, reducing atmosphere enhances the SMSI character of a TMO with Pt by increasing the oxygen vacancy concentration, whereas oxidizing atmosphere suppresses the effect[16-20]. To study how varying the extent of SMSI influences electroforming, we first performed the experiment on a $Pt/TiO_2/Pt$ lateral device (Fig. C.6 a) in a reducing atmosphere (H_2 gas, at 300 Torr). In a reducing H_2 atmosphere, in conjunction with a higher concentration of oxygen vacancies, Ti reduction also occurs providing more n-type polarons thus enhancing the electrical conductivity of the virgin device by ~50 times in comparison to air (Fig. C.6 a, inset)[8]. As a result, upon application of electrical bias, electroforming was achieved at a lower electric field of ~2 MV/cm (Fig C.6 a) as compared to an ambient atmosphere. Post-electroforming, the device was characterized via TEM (Fig. C.6 b) and EFTEM (Fig C.6 c), which confirmed the formation of Pt filaments constituting a large number of uniformly distributed Pt particles between the two metal electrodes in contrast to a dense single filament obtained under ambient conditions (Fig. C.2). However, experiments performed on another device (Fig. C.6 d) under an oxidizing atmosphere (300 Torr O_2) did not result in electroforming even upon application of 40 V (~6 MV/cm) (Fig. C.6 e). Yet, the same device, when exposed to ambient conditions, underwent electroforming at ~2.5 MV/cm (Fig. C.6 e). These results underline the importance of the environment in the electroforming process where the conductive metallic filament is readily formed in ambient and reducing atmospheres but

not under oxidizing conditions. In fact, it is easier to electroform a device under a reducing atmosphere as compared to ambient conditions.

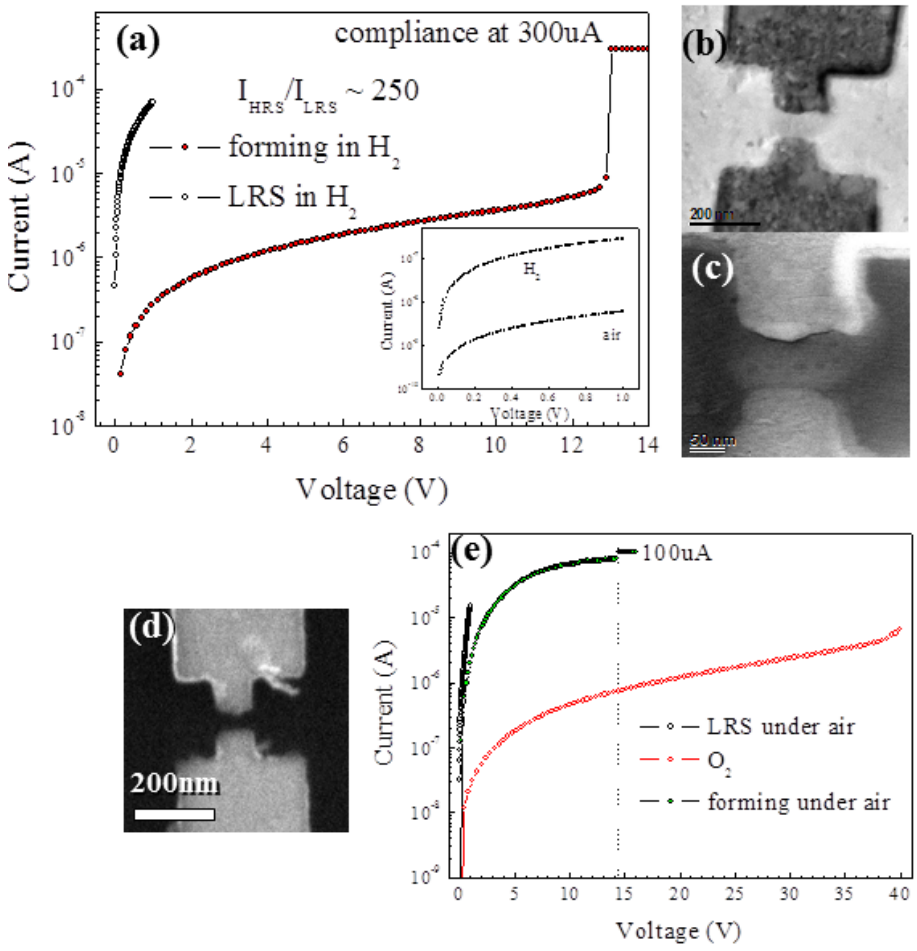

Figure C.6 Atmosphere dependent electroforming process in a lateral Pt/TiO_2/Pt devices (a) I-V characteristic curves of the device during (red circles) and post (black circles) electroforming process in H_2 atmosphere. Forming voltage is ~ 13 V with the compliance level set at 300 µA. Inset shows the current level of the same device before the electroforming process in ambient conditions and 300 torr of H_2. (b) TEM image of the device after the electroforming process in H_2. (c) Pt O-edge mapped EFTEM image of the nanogap region shows continuous Pt filament formation. (d) SEM image of a Pt/TiO_2/Pt device prior to TiO_2 deposition. (e) I-V characteristic curves of the device under O_2 at 300 torr during the failed electroforming attempt (red filled circles), successful electroforming under air (green filled circles) and subsequent LRS under air (black circles). The device did not switch under 100 % O_2.

C.8 Oxygen Vacancy Mediated Electroforming Mechansim in Pt/TiO_2/Pt Devices

Based on these observations, the following mechanism for electroforming in our lateral Pt/TiO_2/Pt devices via conductive metallic filament formation is proposed. During device fabrication, upon annealing of the TiO_2 film deposited above the Pt electrodes in an inert atmosphere, polycrystalline anatase TiO_2 is formed, which is known to have structural oxygen vacancies[25-29]. Characterization of the annealed device via X-ray photoelectron spectroscopy and contact angle measurements shows that after annealing in an inert atmosphere, TiO_2 film becomes more hydrophobic as a result of losing the hydroxide ions[31-33] leading to a reduced, off-stoichiometric anatase phase with structural oxygen vacancies (Fig. C.1). This is the first instance at which SMSI between Pt from the electrodes and adjacent TiO_2 is initiated, thereby facilitating the detachment of Pt from the electrode through enhanced attraction between reduced TiO_2 and atomic Pt (Fig C.7 a). Under applied electric field, it is known that in TMOs such as TiO_2, oxygen vacancies are created near the anode by discharging O_2 gas, subsequently migrating towards the cathode since they have a net positive charge, and are finally quenched near the cathode by consuming O_2 gas from the atmosphere[8,9] (Fig C.7 b). Therefore, as oxygen deficient and partially reduced TiO_{2-x} region is created near the anode and progresses towards the cathode under an applied electrical bias, Pt atoms are dragged along owing to enhanced SMSI character of this region, which has a higher concentration of oxygen vacancies as compared to its surroundings (Fig C.7 c). As more Pt atom dissociation from the anode follows, this fragmentation process is further catalyzed by Joule heating and especially by the enhanced SMSI character of reduced TiO_{2-x} continuously created near the anode as described earlier. This sequence of events finally leads to sufficient Pt injection into the

TiO_2 matrix such that Pt atoms can migrate along with oxygen vacancies towards the cathode to form a continuous metallic bridge across the electrodes following the oxygen deficient phase (Fig C.7 d). The role of TiO_2 and accompanied SMSI-assisted Pt migration is further supported in another experiment (Fig. C.8) where the TiO_2 film near the Pt anode was partly delaminated but still allowed to contact the Pt cathode in some part; and the electroforming process in this device occurred by Pt migration via a circuitous path tracking the TiO_2 film, forming a dendrite like filament following the fringe electric field.

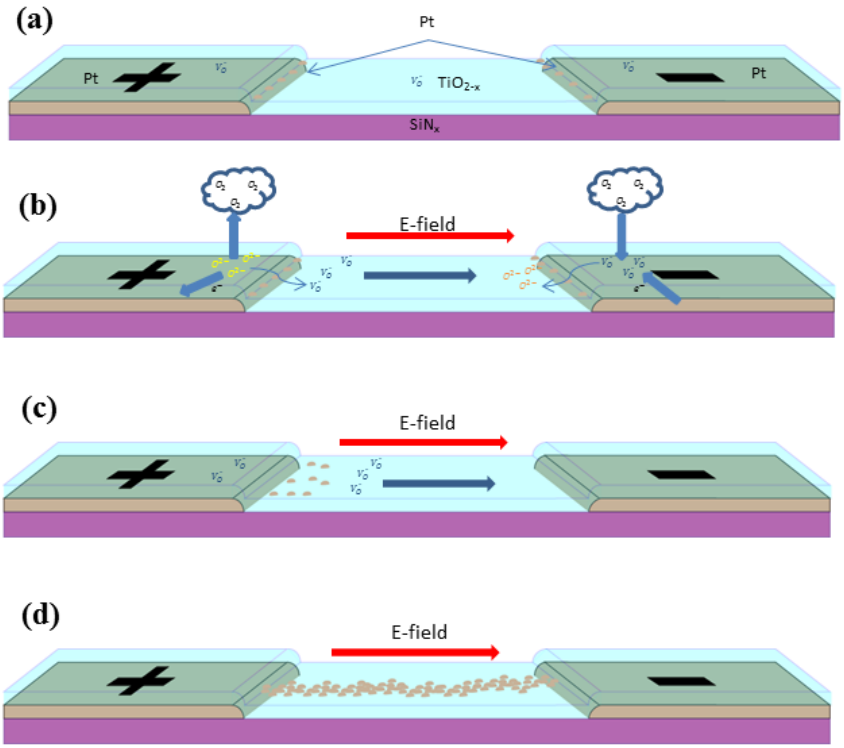

Figure C.7 Schematic of the electroforming process. (a) $Pt/TiO_2/Pt$ device after annealing and before application of electrical bias showing partially reduced TiO_{2-x} film with Pt atoms from both electrodes detaching into the film. (b) Creation and annihilation of oxygen vacancies near the anode (+) and the cathode (-) respectively under an applied bias and their subsequent motion by drift and diffusion towards the cathode. (c) Migration of atomic Pt along with oxygen vacancies from the anode towards the cathode under an applied bias by enhanced SMSI between Pt and partially reduced TiO_{2-x} film. (d) Formation of a continuous Pt conductive filament once sufficient metal has detached from the anode and migrated towards the cathode.

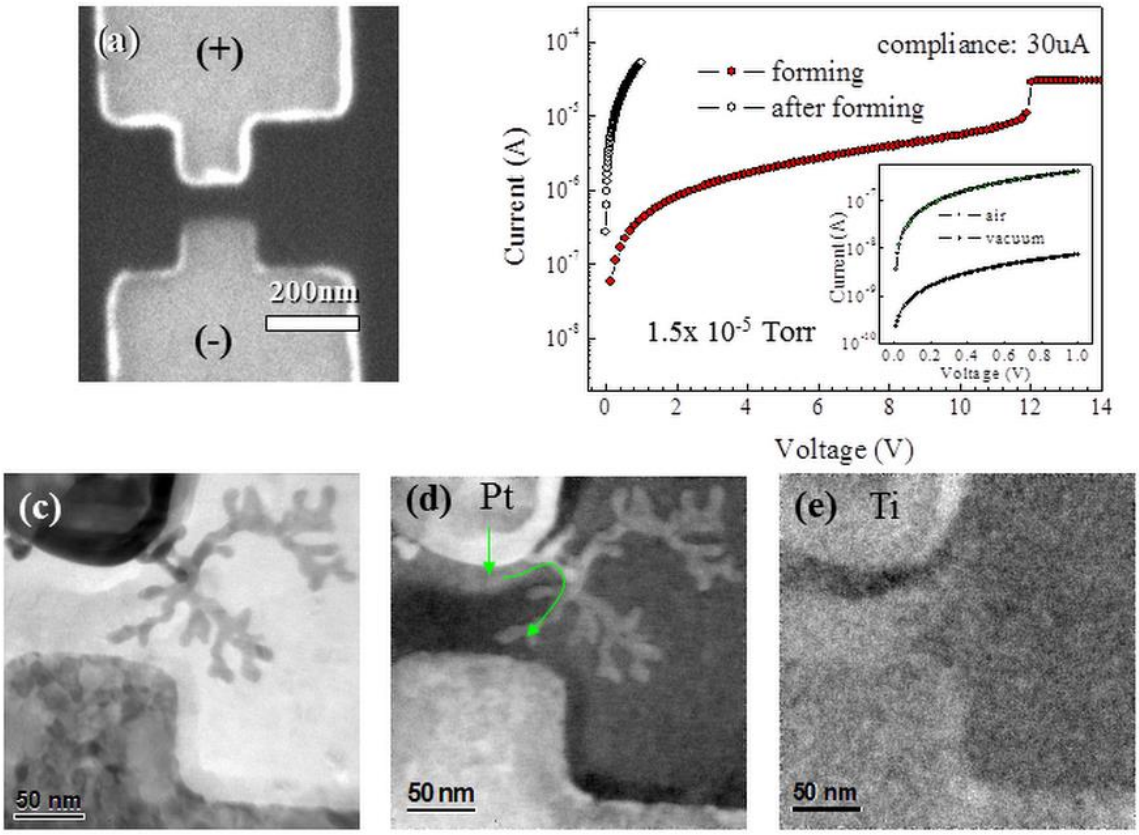

Figure C.8 Characterization of a Pt/TiO_2/Pt device before and after electroforming under high vacuum. (a) SEM image of the device prior to TiO_2 deposition. (b) I-V characteristic curves during (red circles) and after (black circles) the electroforming event in the Pt/TiO_2/Pt resistive memory device. The compliance level is set at 30 μA and the forming voltage was 12 V. The I_{HRS}/I_{LRS} ratio is ~130. (c) TEM image of the device after the electroforming process showing a dendrite shaped Pt filament formed between the two electrodes circumventing the delaminated TiO_2 film (red dotted circle). (d) Pt O-edge EFTEM map of the device with the same region as (c) confirming the dendrite shaped filament is made of Pt. (e) Ti L-edge EFTEM map of the device with the same region of (c) showing the delaminated TiO_2 film between the two electrodes (darker region inside red dotted circle).

Atmosphere dependent electroforming experiments further highlight the role of SMSI in Pt migration in Pt/TiO_2/Pt system under the applied electric field. (i) In reducing atmosphere, oxygen vacancy formation is enhanced[8]. Generally, an overall increase in the oxygen vacancy concentration significantly increases Pt-TiO_2 interaction via SMSI, thereby opening multiple pathways through which Pt metal can migrate from the anode

towards the cathode resulting in a more spread-out and much thinner metallic filaments. (ii) Under high vacuum, oxygen vacancy concentration increases as compared to ambient conditions, due to which electroforming occurs at lower voltages, similar to the case of a reducing atmosphere (Fig. C.8). (iii) Under ambient conditions, equilibrium vacancy concentration of TiO_2 is sufficient to drive forward the electroforming process, even though oxygen vacancies are constantly being created at the anode and annihilated at the cathode. (iv) In an oxidizing atmosphere, where the equilibrium oxygen vacancy concentration of TiO_2 is greatly suppressed, Pt motion is sluggish owing to reduced interaction between Pt and TiO_2, explaining the lack of electroforming.

C.9 Conclusions

In conclusion, by combining electron microscopy with novel device designs, we have shown the role of oxygen vacancy dynamics during electroforming by utilizing a noble metal such as Pt as a tracer element for oxygen vacancies in TiO_2 via strong metal-support interaction. By performing experiments in different atmospheres and with different material systems, the role of oxygen vacancies during the electroforming process in Pt-TiO_2, a prototypical resistive memory device system, is further highlighted. The clear role of oxygen vacancies during switching and the realization that passive electrode may not be as inert as generally assumed, will further help our understanding of the complex processes that can occur in typical resistive memory devices, thus aiding developing the next generation of nanoscale memory systems.

C.10 References

1. Janousch, M.; Meijer, G. I.; Staub, U.; Delley, B.; Karg, S. F.; Andreasson, B. P. Adv. Mater. 2007, 19, (17), 2232.

2. Jiang, A. Q.; Wang, C.; Jin, K. J.; Liu, X. B.; Scott, J. F.; Hwang, C. S.; Tang, T. A.; Lu, H. B.; Yang, G. Z. Adv. Mater. 2011, 23, (10), 1277.

3. Song, S.; Cho, B.; Kim, T.-W.; Ji, Y.; Jo, M.; Wang, G.; Choe, M.; Kahng, Y. H.; Hwang, H.; Lee, T. Adv. Mater. 2010, 22, (44), 5048.

4. Waser, R.; Dittmann, R.; Staikov, G.; Szot, K. Adv. Mater. 2009, 21, (25-26), 2632.

5. Kim, D. C.; Seo, S.; Ahn, S. E.; Suh, D.-S.; Lee, M. J.; Park, B.-H.; Yoo, I. K.; Baek, I. G.; Kim, H.-J.; Yim, E. K.; Lee, J. E.; Park, S. O.; Kim, H. S.; Chung, U.-I.; Moon, J. T.; Ryu, B. I. Appl. Phys. Lett. 2006, 88, (20), 202102.

6. Yoshida, C.; Tsunoda, K.; Noshiro, H.; Sugiyama, Y. Appl. Phys. Lett. 2007, 91, (22).

7. Jeong, D. S.; Schroeder, H.; Waser, R. Electrochem Solid St 2007, 10, (8), G51.

8. Jeong, D. S.; Schroeder, H.; Breuer, U.; Waser, R. J. Appl. Phys. 2008, 104, (12).

9. Yang, J. J.; Miao, F.; Pickett, M. D.; Ohlberg, D. A. A.; Stewart, D. R.; Lau, C. N.; Williams, R. S. Nanotechnology 2009, 20, (21).

10. Kwon, D. H.; Kim, K. M.; Jang, J. H.; Jeon, J. M.; Lee, M. H.; Kim, G. H.; Li, X. S.; Park, G. S.; Lee, B.; Han, S.; Kim, M.; Hwang, C. S. Nature Nanotechnol. 2010, 5, (2), 148.

11. Hu, C. Q.; McDaniel, M. D.; Posadas, A.; Demkov, A. A.; Ekerdt, J. G.; Yu, E. T. Nano Lett. 2014, 14, (8), 4360.

12. Hu, Y. S.; Perello, D.; Yun, M.; Kwon, D. H.; Kim, M. Microelectron. Eng. 2013, 104, 42.

13. Waser, R.; Aono, M. Nat. Mater. 2007, 6, (11), 833.

14. Yang, Y. C.; Gao, P.; Gaba, S.; Chang, T.; Pan, X. Q.; Lu, W. Nat. Commun. 2012, 3.

15. Yang, J. J. S.; Strukov, D. B.; Stewart, D. R. Nature Nanotechnol. 2013, 8, (1), 13.

16. Zhang, J. W.; Zhang, M.; Jin, Z. S.; Wang, J. J.; Zhang, Z. J. Appl. Surf. Sci. 2012, 258, (8), 3991.

17. Bamwenda, G. R.; Tsubota, S.; Nakamura, T.; Haruta, M. Catal. Lett. 1997, 44, (1-2), 83.

18. Tauster, S. J.; Fung, S. C.; Garten, R. L. J. Am. Chem. Soc. 1978, 100, (1), 170.

19. Li, Q. Y.; Wang, K.; Zhang, S. L.; Zhang, M.; Yang, H. J.; Jin, Z. S. J. Mol. Catal a-Chem. 2006, 258, (1-2), 83.

20. Tauster, S. J.; Fung, S. C.; Baker, R. T. K.; Horsley, J. A. Science 1981, 211, (4487), 1121.

21. Nukala, P.; Agarwal, R.; Qian, X. F.; Jang, M. H.; Dhara, S.; Kumar, K.; Johnson, A. T. C.; Li, J.; Agarwal, R. Nano Lett. 2014, 14, (4), 2201.

22. Nam, S. W.; Chung, H. S.; Lo, Y. C.; Qi, L.; Li, J.; Lu, Y.; Johnson, A. T. C.; Jung, Y. W.; Nukala, P.; Agarwal, R. Science 2012, 336, (6088), 1561.

23. Yang, Y. C.; Gao, P.; Li, L. Z.; Pan, X. Q.; Tappertzhofen, S.; Choi, S.; Waser, R.; Valov, I.; Lu, W. D. Nat. Commun. 2014, 5.

24. Klein, N.; Gafni, H. Ieee T. Electron. Dev. 1966, Ed13, (2), 281.

25. Minato, T.; Kawai, M.; Kim, Y. J. Mater. Res. 2012, 27, (17), 2237.

26. Cheng, H. Z.; Selloni, A. Phys Rev B 2009, 79, (9).

27. Su, J.; Zou, X. X.; Chen, J. S. RSC Adv. 2014, 4, (27), 13979.

28. Diebold, U. Surf. Sci. Rep. 2003, 48, (5-8), 53.

29. Ganduglia-Pirovano, M. V.; Hofmann, A.; Sauer, J. Surf. Sci. Rep. 2007, 62, (6), 219.

APPENDIX D: LIST OF PUBLICATIONS

A. Accepted Publications

1) **R. Agarwal**, D. N. Zakharov, N. M. Krook, W. Liu, J. Berger, E. A. Stach and R. Agarwal, "Real-time Observation of Morphological Transformations in II-VI Semiconducting Nanobelts via Environmental Transmission Electron Microscopy" Nano Letters 5, (2015), p.3303.

2) F. Streller‡, **R. Agarwal**‡, F. Mangolini and R.W. Carpick, "Novel Metal Silicide Thin Films by Design via Controlled Solid-State Diffusion", Chem. Mater. 27, (2015), p.4247 ‡ *Equal Authorship*.

3) M. Cargnello‡, **R. Agarwal**‡, D. Klein, B. Diroll, R. Agarwal and C.B. Murray, "Uniform Bimetallic Nanocrystals by High-Temperature Seed-Mediated Colloidal Synthesis and Their Catalytic Properties for Semiconducting Nanowire Growth", Chem. Mater. 27, (2015), p.5833 ‡ *Equal Authorship*.

4) P. Nukala, **R. Agarwal**, X. Qian, M.H. Jang, S. Dhara, K. Kumar, A. T. C. Johnson, J. Li and R. Agarwal, "Direct Observation of Metal-Insulator Transition in Single-Crystalline Germanium Telluride Nanowire Memory Devices Prior to Amorphization", Nano Lett. 14, (2014), p.2201.

5) C.O. Aspetti, C.H. Cho, **R. Agarwal** and R. Agarwal, "Studies of hot photoluminescence in plasmonically coupled silicon via variable energy excitation and temperature dependent spectroscopy", Nano Lett. 14, (2014), p.5413.

6) B.Piccione, **R. Agarwal**, Y. Jung and R. Agarwal, "Size-dependent chemical transformation, structural phase change, and optical properties of nanowires", Philosophical Magazine 93, (2013), p.2089.

7) Y. Jung, **R. Agarwal**, C.Y. Yang and R. Agarwal, "Chalcogenide Phase-change Memory Nanotubes for Lower Writing Current Operation", Nanotechnology 22, (2011), p.4012. (invited paper for the nanoscale memory issue).

8) Vicky V.T. D-Nguyen, S. Zhang, E.B. Trigg, **R. Agarwal,** J. Li, D. Su, K.I. Winey and C.B. Murray, "Synthesis and X-ray Characterization of Cobalt Phosphide Nanorods for Oxygen Reduction Reaction", ACS Nano 9, (2015), p.8108.

B. Publications Under Review

9) M. Ren‡, **R. Agarwal**‡, W. Liu and R. Agarwal, "Crystallographic Characterization of II-VI Semiconducting Nanostructures via Optical Second Harmonic Generation", (Under Review at ACS Nano. Lett.) ‡ *Equal Authorship*

10) M.H. Jang‡, **R. Agarwal**‡, P. Nukala, D. Choi, A.T.C. Johnson, I-W. Chen and R. Agarwal, "Observing Oxygen Vacancy Driven Electroforming in Pt-TiO_2-Pt Device via Strong Metal Support Interaction", (Under review at ACS Nano Lett.) ‡*Equal Authorship*

C. Publications Under Preparation

11) **R. Agarwal**, N. M. Krook, M.-L. Ren, L.Z. Tan, W. Liu, A. M. Rappe and R. Agarwal, "Atomic Templating via Anion Exchange in II-VI Semiconducting Nanostructures"

12) M. Ren‡, **R. Agarwal‡**, P. Nukala, W. Liu and R. Agarwal, "Nanotwin Detection and Domain Polarity Determination via Optical Second Harmonic Generation" ‡*Equal Authorship*

13) **R. Agarwal**, Y. Kim, S. Liu, L.Z. Tan, W. Liu, A. M. Rappe and R. Agarwal, "Atomic Templating Based Chemical Transformation in II-VI Semiconducting Nanostructures"

14) P. Nukala, M. Ren, **R. Agarwal** and R. Agarwal, "Manipulating Domains in Germanium Telluride, a Ferroelctric Metal"

15) **R. Agarwal** and R. Agarwal, "Chemical Transformation in Covalent Compounds".